Universitetet i Stavanger

FACULTY OF SCIENCE AND TECHNOLOGY

MASTER'S THESIS

Study programme/specialisation: Offshore Technology – Marine- and Subsea Technology	Spring semester, 2017 Open / ~~Confidential~~
Author: Andreas Vangdal Høiland	…… (signature of author)
Programme coordinator: Supervisor(s): Prof. Muk Chen Ong, Dr. Lin Li, Dr. Zhiyu Jiang	
Title of master's thesis: Dynamic Analysis of a Vessel-shaped Fish Farm for Open Sea	
Credits: 30	
Keywords: Aquaculture, Concept, Dynamic, Finite Element Method, Frequency domain, Hydrodynamics, RAO, SIMO, SIMO-Riflex, Time domain, Vessel-shaped, Fish farm, Wadam	Number of pages: 100 + supplemental material/other: 18 Stavanger, June 15 /2017 Date/year

Abstract

In recent years, aquaculture has been the fastest-growing animal food producing industry in the world. However, the absence of suitable production areas might potentially become the most limiting factor for future production growth. This motivates and necessitates the development of open sea fish farming. Design of offshore aquaculture systems is a novel and unique engineering challenge, which will depend on numerical tools that can simulate and predict the structural response in open sea conditions. In this master thesis, a vessel-shaped fish farm concept for offshore fish farming is studied. The vessel uses a turret mooring system for station keeping and is designed to break incoming waves and reduce environmental loads on the system. Dynamic analyses have been carried out using numerical simulation programs, with the aim to analyse vessel motions, mooring lines, fish nets, and coupled motions of the system.

For studies of the hydrodynamic properties of the vessel, different panel models were created using the design analysis tool GeniE. The RAOs in heave, roll, and pitch were obtained from frequency domain analyses of the vessel hull, using the potential flow solver Wadam. Hydrodynamic data acquired from frequency domain analyses were exported from Wadam to SIMO, the program used for quasi-static time domain analysis of the vessel and simplified mooring system. Based on the mooring lines performance in SIMO, new mooring line parameters were established for the fully coupled time domain simulations in SIMO-Riflex, where fully coupled time domain analyses of the vessel-shaped fish farm was carried out.

A sensitivity study was carried out from the fully coupled time domain simulations by comparing three different fish net models; rigid model, flexible model, and flexible model with no reduction factor. It was found that the simplified models overestimate the drag forces on the system, and it is recommended that neither of the simplified models should be used for future dynamic analyses of aquaculture systems. Development of tension in the foremost and rearmost fish nets was studied in steady current conditions, and with a conjunction of regular waves and steady currents. A mutual dependency between the forces on the net and its deformations was found. Motions of the coupled fish farm system and the efficiency of mooring lines were studied in time domain simulations with regular waves and steady currents.

Acknowledgement

I would like to thank my supervisor Prof. Muk Chen Ong for his continuous guidance and consultation throughout this semester. His outstanding motivation and support has granted me focus and guided me in the right direction during the whole of this semester.

I would like to express my sincere gratitude to my Co-supervisor Dr. Lin Li for her help and patience in solving problems for this thesis. All the time she has set available to consult on the thesis and her help regarding Wadam and SIMA related challenges are greatly appreciated.

I would also like to thank my Co-supervisor Dr. Zhiyu Jiang for taking his time to attend scheduled meetings and provide constructive comments on the thesis. I would like to extend my sincerest thanks for his recommendations and consultation on HydroD and SIMA related topics.

Finally, I want to give special gratitude to my family and girlfriend, for their love and unlimited support has kept me going through challenging times.

Table of Contents

1 Introduction 1

1.1 Overview of Existing Technologies 2

1.1.1 Plastic Fish Cage 2

1.1.2 Hinged Steel Fish Cage 3

1.1.3 Submersible Fish Cage 4

1.2 Literature Review 5

1.3 Objective 6

2 Theoretical Background 8

2.1 Potential Flow Theory 8

2.1.1 Basic Assumptions 8

2.1.2 Laplace Differential Equation 9

2.1.3 Boundary Conditions 10

2.1.4 Excitation Forces 11

2.1.4.1 Froude-Krylov Force 11

2.1.4.2 Diffraction Force 12

2.1.5 Radiation Forces 12

2.1.6 Equations of Motion and RAO 13

2.2 Hydrodynamic Loads in Frequency Domain 14

2.2.1 Morison’s Formula for Slender Structures 14

2.2.2 Stochastic Drag Linearization 15

2.3 Hydrodynamics of Fish Nets 17

2.3.1 Drag and Lift Forces on Fish Nets 19

2.3.2 Velocity Reduction Factor 21

2.4 Mooring System 22
2.5 Waves and Currents 26
2.5.1 Regular Waves 26
2.5.2 Linear Wave Theory 27
2.5.3 Irregular Waves 28
2.5.4 Wave Spectra 29
2.5.5 Currents 31
2.6 Time Domain Finite Element Method 32
2.6.1 Nonlinear Finite Element Analysis 33
2.6.2 Coupled Analysis 33
3 Hydrodynamic Analysis – Vessel in Frequency Domain 35
3.1 Numerical Analysis Program and Input 35
3.1.1 Frequency Set 37
3.1.2 Panel Model 37
3.1.3 Composite Model 39
3.1.3.1 Added Mass Coefficient 40
3.1.3.2 Drag Coefficient 40
3.1.3.3 JONSWAP Wave Spectrum 43
3.2 Hydrodynamic Results 44
3.2.1 Sensitivity Study from Different Frequency Sets 44
3.2.2 Convergence Study Using Different Panel Models 50
3.2.3 Comparison of Panel Model and Composite Model 54
4 Response Analysis – Coupled Vessel and Mooring System 57
4.1 Simulation program SIMO 57
4.2 Static Calculation of Mooring Lines 58

4.3 Numerical Modelling in SIMO 61
4.4 Time Domain Simulation Results 64
4.4.1 Vessel Motions 65
4.4.1.1 Translational Motion in X-direction 65
4.4.1.2 Translational Motion in Y-direction 66
4.4.1.3 Rotational Motion About X-axis 68
5 Response Analysis – Coupled Vessel, Fish Nets, and Mooring Lines 70
5.1 Simulation Program SIMO-Riflex 70
5.2 Numerical Modelling in SIMO-Riflex 73
5.2.1 Modelling of Mooring Lines 73
5.2.2 Modelling of Flexible Fish Nets 75
5.2.3 Modelling of Rigid Fish Nets 78
5.2.4 Modelling of Waves and Currents 81
5.3 Time Domain Simulation Results 82
5.3.1 Comparison of Rigid and Flexible Fish Net Models 82
5.3.2 Mooring Line Tension and Drift-Off 85
5.3.3 Fish Net Tension in Current 88
5.3.4 Fish Net Tension in Waves and Current 89
5.3.5 Sensitivity Study on Solidity Ratio 93
6 Conclusions and Further Work 94
6.1 Conclusions 94
6.2 Further Work 95
7 References 97

List of Figures

Figure 1.1: Square- and circular-shaped fish farm (AKVAgroup, 2016) 2

Figure 1.2: Plastic Fish Cage (AKVAgroup, 2016) 3

Figure 1.3: Hinged Steel Fish Cage (AKVAgroup, 2016). 4

Figure 1.4: Submersible Fish Cages, where left is active(Plastforum, 2016) and right is passive (Refamed, 2015) 5

Figure 1.5: Vessel-shaped fish farm concept (Bennett, 2016) 7

Figure 2.1: Principal illustration of flow through system of net cages (Løland, 1993) 18

Figure 2.2: Conical-shaped fish farm (Egersund Net, 2016) 19

Figure 2.3: Basic definition of a net with parameters. 20

Figure 2.4: Drag coefficient and velocity reduction factor, as function of solidity ratio (Løland, 1993) 21

Figure 2.5: Wake velocity behind a screen, width of 10 m and initial velocity u=0.8·U (Løland, 1993) 22

Figure 2.6: Internal and external turret (Chakrabarti, 2005) 24

Figure 3.1: Water depth and wave directions for frequency domain analyses 36

Figure 3.2: Dimensions of vessels submerged section 38

Figure 3.3: Illustration of Morison elements 40

Figure 3.4: Drag coefficient for rectangle 42

Figure 3.5: JONSWAP wave spectrum from Wadam 44

Figure 3.6: Heave low frequency 45

Figure 3.7: Roll low frequency 45

Figure 3.8: Pitch low frequency 46

Figure 3.9: Heave modified frequency 46
Figure 3.10: Roll modified frequency 47
Figure 3.11: Pitch modified frequency 47
Figure 3.12: Heave final frequency 48
Figure 3.13: Roll final frequency 48
Figure 3.14: Pitch final frequency 49
Figure 3.15: Comparison of frequency sets, heave motion for wave direction 0 50
Figure 3.16: Panel model 1 (top) and Panel model 2 (bottom) 51
Figure 3.17: Panel model comparison, heave motion for wave direction 90 52
Figure 3.18: Panel model comparison, pitch motion for wave direction 90 52
Figure 3.19: Panel model comparison, roll motion for wave direction 90 53
Figure 3.20: Heave, comparison of composite model and panel model 55
Figure 3.21: Roll, comparison of composite model and panel model 55
Figure 3.22: Pitch, comparison of composite model and panel model 56
Figure 4.1: SIMO program modules (MARINTEK, 2015) 58
Figure 4.2: Simplified illustration of mooring line configuration 59
Figure 4.3: Wave directions for time domain simulations SIMO 62
Figure 4.4: Location of reference point for vessel motions in time domain 64
Figure 4.5: Mooring line lifted from the seabed for EC7 65
Figure 4.6: Translation motion in X-direction, EC1 66
Figure 4.7: Translational motion in X-direction, EC2 66
Figure 4.8: Translational motion in Y-direction, EC1 67

Figure 4.9: Translation motion in Y-direction, EC2 68

Figure 4.10: Rotational motion about X-axis, EC1 69

Figure 4.11: Rotational motion about X-axis, EC2 69

Figure 5.1: Components modelled in SIMO and Riflex for SIMO-Riflex simulations 72

Figure 5.2: Structure of Riflex system (MARINTEK, 2016a) 72

Figure 5.3: SIMO-Riflex mooring lines with numbering 75

Figure 5.4: Fish net with supernodes and slender lines 76

Figure 5.5: Rigid nets and supernodes 80

Figure 5.6: Vessel position in EC12 81

Figure 5.7: Tension in mooring line 1 for different current velocities and fish net models 84

Figure 5.8: Mooring line tensions in 0.1 m/s current 84

Figure 5.9: Mooring line tensions in 0.5 m/s current 84

Figure 5.10: Mooring line tensions in 1.0 m/s current 85

Figure 5.11: Maximum mooring line tension EC9, EC10, EC11, and EC12 87

Figure 5.12: Displacement in X-dir for EC9, EC10, EC11, and EC12 88

Figure 5.13: Net deformation from simulations with current velocity of 0.4 m/s (left) and 0.8 m/s (right) 89

Figure 5.14: Fish net tension for different current velocities 89

Figure 5.15: Axial tension in fish net, EC9 92

Figure 5.16: Axial tension in fish net, EC10 92

Figure 5.17: Axial tension in fish net, EC11 92

Figure 5.18: Upstream fish net tension for varying solidity ratios 93

List of Tables

Table 3.1: Parameters for calculation of Reynolds number 41

Table 3.2: Input for JONSWAP wave spectrum 43

Table 3.3: Comparison of frequency sets 49

Table 3.4: Maximum RAO amplitudes for different panel models 54

Table 4.1: Chosen characteristic values for mooring lines 60

Table 4.2: Calculated values for mooring lines 60

Table 4.3: SIMA input for JONSWAP wind wave environment 62

Table 4.4: SIMO input parameters imported from Wadam 63

Table 4.5: SIMO input parameters for mooring line 63

Table 5.1: Chain mooring parameters 73

Table 5.2: SIMO-Riflex input parameters for mooring lines 74

Table 5.3: Constants used for fish cage calculations 77

Table 5.4: Riflex input parameters for flexible fish nets 78

Table 5.5: Riflex input parameters for rigid fish nets 80

Table 5.6: Environmental conditions for SIMO-Riflex 82

Table 5.7: Percentage increase in maximum mooring line tension for different fish cage models 85

Table 5.8: Mooring tension data for EC9, EC10, EC11, and EC12 86

Table 5.9: Displacement in x-dir for EC9, EC10, EC11, and EC12 87

Table 5.10: Axial tension in the steady phase, fish net upstream 91

Table 5.11: Axial tension in the steady phase, fish net downstream 91

1 Introduction

Producing sufficient amounts of food for a continuously growing population is a global challenge. Aquaculture can play a major part in meeting these future food needs. The World Bank projects that 62 % of all seafood consumed worldwide will come from fish farming by the year 2030. The Norwegian fish farming industry has developed from humble beginnings in the 1970s, to produce 1.3 million metric tonnes of fish in 2013 with an export value of 39.8 billion NOK (Bjelland et al., 2015).

During the last decades, aquaculture has been the fastest-growing animal food producing industry in the world, where an increase in demand for fish has been the primary incentive for production growth. Furthermore, the productivity advancement has decreased over the years, and production growth will be achieved by increasing the production area (Asche et al., 2013). Fish farming originally started in more sheltered coastal environments. However, due to the industry growth and competition with other coast-based industries, fewer such areas are today available for fish farming. The absence of suitable production areas might potentially become the most limiting factor for future production growth in the aquaculture industry.

The development of the aquaculture industry is aiming to move fish farms from the fjords to the open sea. Utilising these exposed fish farming locations at open sea will increase the suitable production areas tremendously and simultaneously reduce important environmental effects. Open sea fish farming features more stable water flow conditions than sheltered sites in the fjords. This will generate better circulation within the fish farms and lead to greater dispersal of wastes, improved fish welfare, and improved production environment (Bjelland et al., 2015). The severe wave, wind, and current conditions are very challenging for fish farming operations at open sea. It is therefore essential that the aquaculture installation can withstand the environmental loads at these exposed areas.

1.1 Overview of Existing Technologies

There exists much satisfactory technology in today's aquaculture industry, but changing external conditions, human limitations, and increasingly complex solutions result in an increased demand for new technology. A large part of the technology that is available is not very well documented and is largely based on practical experience. For the increased dimensions of structures, combined with more extreme weather conditions it is necessary to base the future technical solutions on scientific research (Sunde et al., 2003).

The most typical systems used in marine aquaculture are sea cages connected to a floater that is moored to the seabed or the shore. The floaters used for aquaculture in the fjords are not built to withstand offshore environmental conditions and are not capable of conducting offshore fish farming. There exist several different systems today with different material and geometry, e.g. plastic fish cages, steel constructions, and submersible cages. The most commonly used fish cages are the plastic fish cages and the hinged steel cages (Sunde et al., 2003). Figure 1 below illustrates one circular and one square shaped modern Norwegian fish farm.

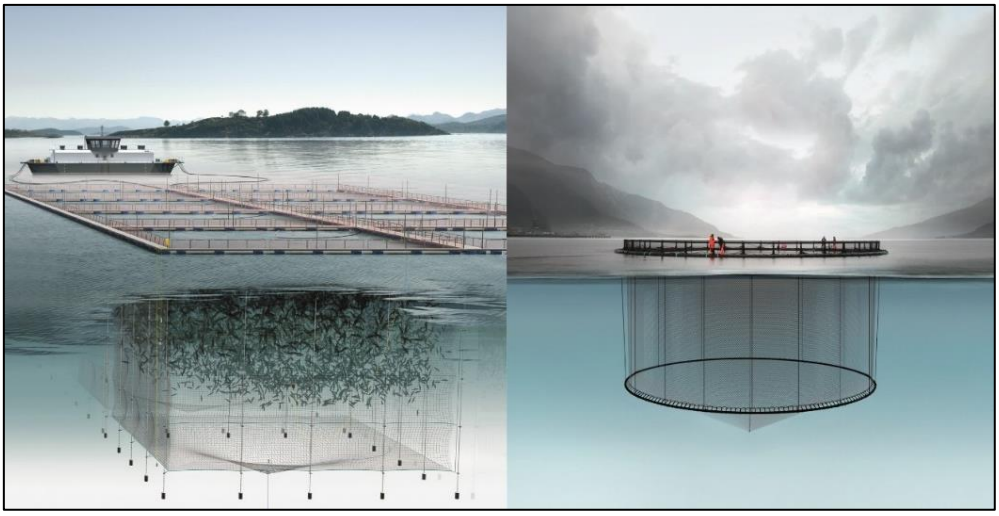

Figure 1.1: Square- and circular-shaped fish farm (AKVAgroup, 2016)

1.1.1 Plastic Fish Cage

The plastic fish farms have been utilized since the mid-1980s, and there have been limited innovative updates to the system in recent years. The most regular cages have a circular shape with two or three floating collars made of extruded high-density polyethylene (HDPE) plastic

pipes, but it is also available as square shaped. The main advantage of these fish cages is that they are produced in a flexible material with no hinge or metal parts, which can suffer fatigue and be damaged by strong current and high seas. Plastic fish cages are also cheaper to produce and install than steel constructions and submersible fish cages. Compared to steel constructions however, the plastic cages absence of wide and stable walkways leads to the unavoidable use of workboats for certain manual work. In addition, the flexible plastic floaters will have large deformations in high sea states. The plastic fish cages are therefore less suitable for manual work and maintenance and can withstand much smaller sea states than steel constructions (Sunde et al., 2003). Figure 1.2 below illustrates a plastic fish cage with two floating collars.

Figure 1.2: Plastic Fish Cage (AKVAgroup, 2016)

1.1.2 Hinged Steel Fish Cage

Flexible steel construction is composed of rigid steel elements which are attached to each other with flexible hinges. This is the best-selling and most common form of steel construction in Norway. The construction type has been common since the mid-80s and is still preferred by farmers along the Norwegian coast. The main advantage with these fish cages is the ability to endure harsh weather, while the wide walkways combined with increased stability allows for manual work and maintenance. Hinged steel cages are however more expensive than the flexible plastic fish cages and face challenges with fatigue damage in hinges/joints and therefore has higher maintenance requirements. Figure 1.3 shows several connected hinged steel cages.

Figure 1.3: Hinged Steel Fish Cage (AKVAgroup, 2016).

1.1.3 Submersible Fish Cage

Submersible fish cages are mainly sold to foreign countries, and only a few submersible facilities exist in Norway, primarily used for testing and research. There are many advantages with submersible fish farms, the most significant advantage being the ability to withstand harsh weather by reducing the environmental loads on the system. There are however many challenges related to the submersible fish cages and their operation, e.g. the fact that salmon requires available air for their swim bladder. There has previously been insufficient research and little technology suitable for operation of the submersible system, but in recent years there has been an increase in interest and research on the system for use both in- and offshore. Certain submersible concepts are "passive" i.e. the current forces induce the immersion, while other systems are technically regulated by the filling floater tubes with water or air. Figure 1.4 below illustrates one "passive" tension leg cage and one technically regulated "active" submersible fish cage.

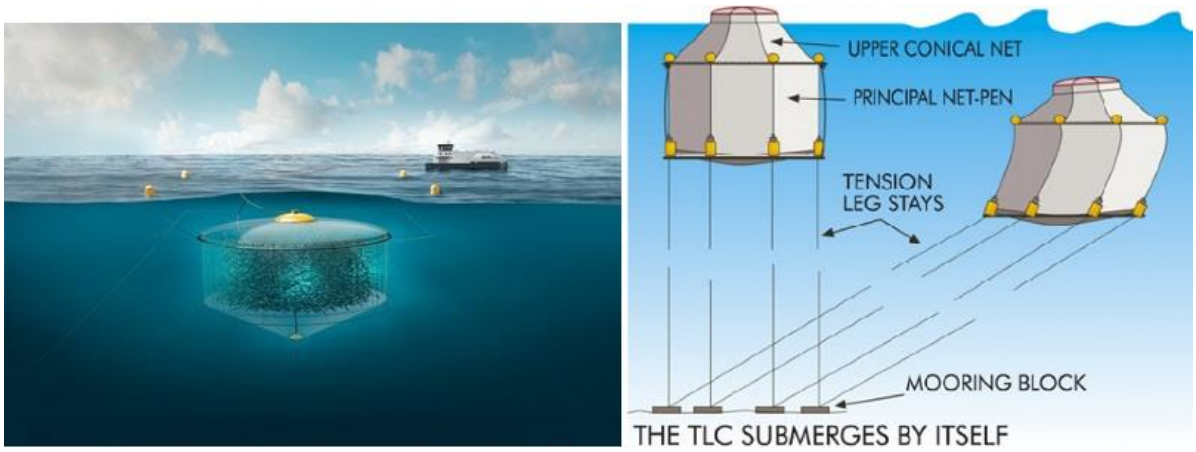

Figure 1.4: Submersible Fish Cages, where left is active(Plastforum, 2016) and right is passive (Refamed, 2015)

1.2 Literature Review

Research on hydrodynamic effects on fish cage systems have been conducted by aquaculture researchers for over 40 years, and the research interest has increased in recent years. Kawakami (1964) proposed semi-empirical formulas based on the fundamental concept of drag force, enabling the estimation of environmental loads on nets. In more recent years, Løland (1991) studied the drag and lift forces on a net panel in conjunction with current directions and shielding effects. The relationship between deformation of flexible nets and hydrodynamic forces was studied by Lader et al. (2003), and an approach to predict global forces on flexible net sheets was developed from scale model testing by Lader and Enerhaug (2005).

A consistent finite element method to model hydrodynamic response of net panels in wave and current loads was proposed by Tsukrov et al. (2003), and accuracy of numerical predictions was evaluated by comparison with experimental observations. Fredriksson et al. (2003) adopted a stochastic approach to analyse motion response characteristics and tension response in an anchor line to wave loads. The work was validated by comparing simulations of physical and numerical models with field observations, and have resulted in important information on the fish cage and mooring performance in the energetic open ocean.

Most recently, Zhao et al. (2007) developed a numerical model based on the lumped-mass method and simulated the dynamic response of a gravity cage in regular waves combined with

currents. The gravity cage motions and mooring line forces from numerical simulations were all in close agreement with experiment data from physical model tests. Kristiansen and Faltinsen (2012) proposed a screen force model for viscous hydrodynamic load on nets, where the screen model divides the net into a number of flat net panels. The screen model is a generalisation of the screen model by Løland (1991), and satisfactory agreement of experimental and numerical predictions of drag and lift as a function of solidity ratio was documented.

There has been an increased attention on extending aquaculture operations to the open sea (Lader et al. (2007); Huang et al. (2008); Tsukrov et al. (2003)). This is mainly due to lack of available sheltered locations, and the tremendous growth of the aquaculture industry necessitates and motivates the use of offshore locations for future fish farming (Lader et al., 2007). The extensive studies presented in this chapter, have resulted in improved understanding of external forces affecting fish cages and provided necessary information for designing structures that can withstand the environmental forces of the open sea.

In open sea environments, the design of reliable systems to withstand waves and currents require stricter design criteria and novel engineering methods. These methods include mathematical modelling of the dynamic responses of structures in high-energy sea areas and simulations of the open sea environmental loads acting on aquaculture systems (Kristiansen et al., 2015).

1.3 Objective

In recent years, many fish farm systems for open sea development have been proposed. These new concepts focus on reducing risk and increasing profit for production offshore. The company Nordlaks have proposed a vessel-shaped fish farm with single-point mooring system called Havfarm. The floater of the fish farm is vessel-shaped and designed to break waves and reduce the environmental loads on the system. Several fish cages are connected within the vessel hull, and along the vessel sides, there are steel louse skirts that prevent sea lice from entering the fish cages. This thesis will be a study of a similar vessel-shaped fish farm with a

turret mooring system for station keeping. Figure 1.5 illustrates the vessel-shaped fish farm concept.

The objective of this thesis is to perform dynamic analyses of the vessel-shaped fish farm concept, using numerical simulation programs. The aim is to analyse vessel motions, mooring lines, and coupled vessel motions with installed mooring lines and fish nets. Detailed dynamic analyses will be conducted using Wadam, SIMO, and SIMO-Riflex.

Figure 1.5: Vessel-shaped fish farm concept (Bennett, 2016)

2 Theoretical Background

This chapter includes the essential theory of which this thesis work is based on. The derived theory is based on linear wave theory and used for simulations and analysis in this thesis. A linear analysis will usually be sufficiently accurate for prediction of global wave frequency loads. Hence, this thesis will focus on first order waves, in addition to steady currents, and the vessel motions that occur from them. The term linear means that the fluid dynamic pressure and the resulting loads are proportional to the wave amplitude. This means that the loads from individual waves in an arbitrary sea state can be simply superimposed (DNV GL, 2014).

2.1 Potential Flow Theory

2.1.1 Basic Assumptions

To obtain the potential function, some important assumptions are used. The fluid is assumed to be irrotational, and the vorticity is then equal to zero, i.e. the fluid deforms but do not rotate. For this assumption, it follows that the flow is assumed to be frictionless with no shear forces. This is deemed a good approximation for flow (Gudmestad, 2015). For non-rotational flow, we have the following:

$$\omega = \nabla \times U = 0 \tag{2.1}$$

Where ω is the vorticity of the flow and U is the velocity of the flow. The fluid is also assumed to be incompressible, meaning the fluid volume will remain constant, resulting in the following equation:

$$\nabla * U = \frac{\partial u}{\partial x} + \frac{\partial v}{\partial y} + \frac{\partial w}{\partial z} = 0 \tag{2.2}$$

Where u, v, w is the particle velocity in x, y, and z-direction, respectively. The vessel-shaped fish farm will conduct its operations not far from shore, and it is assumed that these areas are suitable for sustainable aquaculture production, with a sufficient and reliable supply of oxygen.

Production in locations closer to shore will also reduce the environmental loads on the vessel and decrease transportation time. With this is mind, the water depth is set to 120 meters for the case studied in this thesis. The water depth can be related to the wavelength and thus determining if we have deep, shallow or intermediate water depths. The following properties for waves are used to determine the range for deep water conditions (Gudmestad, 2015):

- Deep water: $d > \frac{L}{2}$
- Intermediate water depth: $\frac{1}{20} < \frac{d}{L} < \frac{1}{2}$
- Shallow water depth: $\frac{d}{L} < \frac{1}{20}$

Where d is water depth and L is wavelength. For the chosen water depth of 120 meters, all wavelengths of less than 240 meters will result in deep water for this location, corresponding to a wave period of approximately 12.4 second. Thus, the water depth chosen for this thesis is determined to result in deep water conditions, and formulas used is simplified accordingly.

2.1.2 Laplace Differential Equation

From the assumptions mentioned above, we find the Laplace differential equation of second order and the equation for potential flow. The partial derivative of the velocities gives the following equation:

$$V = \nabla\varphi = \frac{\partial\varphi}{\partial x}i + \frac{\partial\varphi}{\partial y}j + \frac{\partial\varphi}{\partial z}k \tag{2.3}$$

Where φ is the velocity potential. By deriving Equation 2.3 above, and exploiting the assumption that the fluid is incompressible and non-rotational, we get the Laplace differential equation of second order and the equation for potential flow:

$$\nabla^2\varphi = 0 \tag{2.4}$$

$$\varphi(x, y, z, t) = \frac{\partial\varphi^2}{\partial x^2} + \frac{\partial\varphi^2}{\partial y^2} + \frac{\partial\varphi^2}{\partial z^2} = 0 \tag{2.5}$$

2.1.3 Boundary Conditions

The boundary conditions are all found from physical considerations using linear wave theory. Partial differential equations have several solutions, and to obtain a solution with sinusoidal waves at the surface, boundary conditions must be applied. Three boundary conditions will be used to solve the Laplace equation; the bottom boundary condition, wall boundary condition, and surface boundary condition.

The bottom boundary condition is based on the fact that it is not possible for water to flow through the seabed. Considering a flat seabed, the bottom boundary condition can be written as:

$$w|_{z=-d} = 0 \quad \Rightarrow \quad \left.\frac{\partial \varphi}{\partial z}\right|_{z=-d} = 0 \tag{2.6}$$

The vessel does not remain in a stationary position in the water but moves with a different velocity than the waves. A kinematic boundary condition is used to describe the relation between the wave and the velocity of the vessel. The kinematic boundary condition states that no water can flow through the surface of the body. For flow in contact with the vessel, this implies that there should be zero difference in the fluid velocity and body surface velocity in the direction normal to the body surface. The kinematic boundary condition is expressed by Equation 2.7.

$$\left(\vec{v} - \vec{U}\right) \cdot \vec{n} = 0 \;\Rightarrow\; \frac{\partial \varphi}{\partial \vec{n}} = U_n, \qquad \text{on the body surface} \tag{2.7}$$

The boundary condition for the infinite/unbounded fluid domain locations is also utilized for simulations conducted in this thesis. The boundary condition states that far from the body, the fluid is not affected by the vessel motions. Thus, the velocity field in an infinite distance from the vessel should be zero. This far field condition can be expresses as in Equation 2.8.

$$\vec{v} \to 0 \;\Rightarrow\; \nabla\varphi \to 0, \qquad \text{as } \sqrt{x^2 + y^2 + z^2} \to \infty \tag{2.8}$$

The surface boundary condition is based on the fact that no water can flow through the surface. To obtain the equation for surface boundary condition, we first look at two separate surface boundary conditions:

- **The kinematic free surface boundary condition:** takes under consideration the fact that water particles at the free surface will always remain at the free surface.
- **The dynamic free surface boundary condition:** pressure at the free surface is constant and equal to the atmospheric pressure. The boundary condition is found by utilizing the Bernoulli equation for pressure field at the surface.

The two different conditions are linearized to remove the nonlinear terms and then combined to obtain the combined free surface boundary condition for $z = 0$, giving the equation:

$$\frac{\partial^2 \varphi}{\partial t^2} + g\frac{\partial \varphi}{\partial z} = 0 \tag{2.9}$$

We can now find a solution for potential flow φ by solving the Laplace equation $\nabla^2 \varphi = 0$, with the boundary conditions. The boundary conditions are linearized and the waves found from the potential function will therefore be sinusoidal waves.

2.1.4 Excitation Forces

The forces on a submerged structure due to waves are determined by different methods depending on the flow regime in close proximity of the structure. As previously mentioned, the Morison's formula is not applicable for the large structure vessel considered in this thesis. The excitation forces acting on the floating body in regular waves can therefore be calculated from either the Froude-Krylov (FK) theory or the diffraction theory.

2.1.4.1 Froude-Krylov Force

According to the FK theory, forces on the structure are calculated by a pressure-area method where an expression of the pressure due to the incident waves is used on the surface of the structure. Based on this theory, the FK force is found from the undisturbed pressure-area in the incoming wave and calculation of the force on the structure is performed assuming the structure has no interference with the waves. It is recognized that the forces derived from the FK theory

are not directly applicable without making a correction due to the oscillation fluid around the structure and this correction is applied in the form of a force coefficient (Chakrabarti, 1987).

2.1.4.2 Diffraction Force

The diffraction loads appear as a result of a change in the wave field by the presence of the vessel. If the incident wave experiences scattering from the surface of the structure, in the form of reflected waves of the same order of magnitude as the incident waves, then the diffraction theory is applied in computing the wave force (Chakrabarti, 1987). Incident waves undergo significant diffraction for offshore structures of large horizontal dimensions, and diffraction theory must then be applied to calculate the wave forces. The diffraction force is found from the vessels interference with the waves.

2.1.5 Radiation Forces

According to linear potential theory, the potential of a floating body is a superposition of the potentials due to the undisturbed incoming wave Φ_w, the potential due to the diffraction of the undisturbed incoming wave on the fixed body Φ_d, and the radiation potentials due to the six body motions Φ_j (Journée and Massie, 2001):

$$\Phi = \sum_{j=1}^{6} \Phi_j + \Phi_w + \Phi_d \tag{2.10}$$

Radiation forces appear due to the vessel motions, i.e. the hydrodynamic loads are the dynamic forces and moments which occurs for an oscillating vessel in still water; waves are radiated from the vessel. The fluids momentum is changed due to the vessel motions, and the pressure change induce the radiation forces. To obtain the forces and moments which occur due to vessel motions, the pressure is integrated over the average wetted surface S_w (Journée and Massie, 2001).

$$\tau_{rad,i} = \begin{cases} -\iint_{S_w} \left(\frac{\partial \Phi_{\text{rad}}}{\partial t}\right)(n)_i ds \quad i = 1,2,3. \\ -\iint_{S_w} \left(\frac{\partial \Phi_{\text{rad}}}{\partial t}\right)(r * n)_{i-3} ds \quad i = 4,5,6 \end{cases} \tag{2.11}$$

Where $i = 1,2,3,4,5,6$ are the six degrees of freedom; surge, sway, heave, roll, pitch, and yaw respectively.

2.1.6 Equations of Motion and RAO

For the submerged rigid body in frequency domain, the linearized equation of motion and the external forces on the system is expressed in Equation 2.12 (Naess and Moan, 2013):

$$\big(M + A(\omega)\big)\ddot{x}(\omega) + B(\omega)\dot{x} + Cx(\omega) = F(\omega) \tag{2.12}$$

The hydrodynamic analysis program Wadam (Wave Analysis by Diffraction and Morison Theory) uses a complex 6 by 1 motion vector $X(\omega, \beta)$ for frequency domain analyses, which can be found from deriving the equation of motion. By applying Newtons law and including the added mass, damping, and exciting force contributions acting on the panel and Morison sections of a hydro model, the equation of motion is altered to (DNV, 2010):

$$\big[-\omega^2\big(M + A(\omega)\big) + i\omega\big(B(\omega)_p + B_v\big) + C + C_e\big]X(\omega, \beta) = F(\omega, \beta) \tag{2.13}$$

Where:

M : represents the 6 by 6 body inertia matrix

$A(\omega)$: represents the 6 by 6 frequency dependent added mass matrix

$B(\omega)_p$: represents the 6 by 6 frequency dependent potential damping matrix

B_v : represents the 6 by 6 linearized viscous damping matrix

C : represents the 6 by 6 hydrostatic restoring matrix

C_e : represents the 6 by 6 external restoring matrix

$F(\omega, \beta)$: is the 6 by 1 complex exciting force vector for frequency ω and incident wave heading angle β

For nonlinear systems, the solution of Equation 2.13 must be solved by iteration for every time step in time domain. The equation of motion can therefore be transformed to fit a nonlinear model, and is then known as the Duhamel's integral. In time domain, the Duhamel's integral accounts for the frequency dependent added mass and linear radiation damping. Duhamel's integral is expressed in Equation 2.14 (Naess and Moan, 2013):

$$(M + A^{\infty})\,\ddot{x}(t) + \int_0^t \kappa\,(t-\tau)\dot{x}(\tau)d\tau + Cx(t) = F(t) \tag{2.14}$$

Vessel response often governs marine operations, especially from an engineering point of view. The equations of rigid body motion are six coupled equations, for three translations (surge, sway and heave) and three rotations (roll, pitch and yaw). From a frequency domain analysis, the RAO gives the response per unit amplitude of excitation, as a function of the wave frequency (DNV GL, 2014).

Each RAO contains a pair of values that define the vessel response for one degree of freedom to one wave direction and period. One of these values relate the amplitude of the vessel motion to the amplitude of the wave, and the other value is a phase that defines the timing of the vessel motion relative to the wave. E.g., will a roll RAO of 0.5 degrees per meter in a wave amplitude of 2 meter, roll between $-1°$ and $1°$ from its static position (Orcina, 2016).

2.2 Hydrodynamic Loads in Frequency Domain

2.2.1 Morison's Formula for Slender Structures

The Morison's formula is based on the assumption that D/L is small, where D is the characteristic horizontal dimensions of the structure and L is the wavelength. From this assumption, it follows that the kinematics of the undisturbed flow near the structure do not change in the incident-wave direction. This assumption is not fulfilled for the vessel-shaped fish farm, and the Morison's formula can therefore not directly be applied to calculate the total force acting on the vessel. However, the Morison's formula can be used to calculate the drag

forces for the slender elements along the ship. This is done for frequency domain analysis with the composite model in Chapter 3.1.3. For wave loads on structures so large that the acceleration is not constant over the body, reflection and other effects must be considered. The Morison's formula is based on experiments and is the sum of the mass force and the drag force (Gudmestad, 2015). The equation for fixed cylinder in still water is given by:

$$f_{z,t} = f_M + f_D = \rho \frac{\pi D^2}{4} C_M \dot{u} + \frac{\rho}{2} C_D D u|u| \tag{2.15}$$

Where C_M is the mass coefficient, C_D is the drag coefficient, u is the horizontal particle velocity, $\dot{u}$ is the horizontal particle acceleration, and ρ is the water density.

The total force is thus given by integrating over the mass force and drag force:

$$F_{(t)} = \int_{-d}^{Surface} f(z,t)dz = \int_{-d}^{\xi} f_M(z,t)dz + f_D(z,t)dz \tag{2.16}$$

For a floating structure, the body itself is moving with a velocity and the Morison's formula is altered to:

$$F_t = \rho \frac{\pi D^2}{4} \dot{u} + \rho C_M \frac{\pi D^2}{4} (\dot{u} - \dot{v}) + \rho \frac{\pi D^2}{4} C_D (u - v)|u - v| \tag{2.17}$$

Where v is the velocity of the body and $\dot{v}$ is the acceleration of the body.

2.2.2 Stochastic Drag Linearization

In frequency domain analysis, the drag term is linearized based on stochastic drag linearization to combine panel method with the drag term in Morison's formula. The composite model analysed in this thesis includes viscous drag forces and therefore require linearization of the drag term. Linearization of the drag forces can be done by either regular-wave linearization or stochastic linearization.

In the regular-wave linearization method, the linear damping coefficient is found from assuming the equivalent damping dissipates an equal amount of energy as the quadratic

damping (Shao et al., 2016). In this method, a wave amplitude is required as input to the linearization scheme. However, it is not clear which wave amplitude should be chosen, as the vessel will encounter waves with different wave amplitudes in a sea state. This is however not a problem when using the method of stochastic drag linearization, since it directly takes into account the characteristics of the wave spectrum.

By assuming the excitation is a Gaussian stochastic process, the equivalent linear damping is found after minimizing the errors in the least square sense. The stochastic linearization is considered to be more rational than the regular wave linearization, since it is dependent on the sea state and there is no uncertainty in the choice of wave amplitude used in the linearization. In this thesis, stochastic drag linearization is therefore used for all Wadam simulations with implemented drag forces. From irregular-wave stochastic linearization, it follows that the drag force on a strip of length dl of a Morison element is expressed as in Equation 2.18 (Shao et al., 2016).

$$dF_D \approx \frac{1}{2}\rho C_D D\sqrt{\frac{8}{\pi}}\sigma_{|v-\dot{x}|}(v-\dot{x})dl = b_v(v-\dot{x}) \tag{2.18}$$

$$b_v = \frac{1}{2}\rho C_D D\sqrt{\frac{8}{\pi}}\sigma_{|v-\dot{x}|}dl \tag{2.19}$$

Here v is the ambient flow velocity, $\dot{x}$ is the motion velocity of the strip, and $\sigma_{|v-\dot{x}|}$ is the standard deviation of the amplitude of relative velocity between ambient flow and the rigid body motions at the Morison elements location. b_v represents the linearized damping coefficient contributed by one strip of length dl. The complete equivalent coefficients are found from integrating Equation 2.18 for each element and sum up the contribution from all included Morison elements.

Integrating all the inertia loads and equivalently linearized drag forces on all Morison elements and summing up the Morison loads, the equation of motion can be rewritten as in Equation 2.20

(Shao et al., 2016). The integration is not included in the present thesis. More details on stochastic linearization can be found in Borgman (1967) and Wolfram (1999).

$$\left(-\omega^2(M + A(\omega) + A_{mor}) - i\omega(B(\omega) + B_{mor}) + (C + C_e)\right)X = F_{exc}(\omega, \beta) + F_{exc,mor} \quad (2.20)$$

Where:

ω : wave frequency

β : wave heading

M : mass matrix of the floating structure

$A(\omega)$: added mass matrix

A_{mor} : added mass damping matrix contributed by the Morison elements

$B(\omega)$: Potential flow damping matrix

B_{mor} : equivalent linearized damping matrix contributed by the Morison elements

C : Hydrostatic restoring matrix

C_e : External restoring matrix due to, e. g. mooring

X : Rigid body motion vector

$F_{exc}(\omega, \beta)$: Wave excitation due to potential flow

$F_{exc,mor}$: excitation force due to Morison loads

2.3 Hydrodynamics of Fish Nets

Fish cages with highly flexible and non-solid fish nets are the common enclosure system used in open sea fish farming today. Their properties, which are rarely encountered in traditional marine engineering, govern the flow pattern within and around the fish farming structure, as shown in Figure 2.1. The permeability allows the flow to go around and partly through the net, and the flexibility allows the net to change shape when affected by current and wave forces. Even though the flexibility and permeability increase the complexity of the task at hand, it is important to keep in mind that increasing flexibility reduces the internal loading. In order to design each net pen and the geometry of the whole system in an optimum manner, one must be

able to evaluate the flow field in close proximity of the fish cages, and their shape when exposed to environmental loads (Reinertsen et al., 1993).

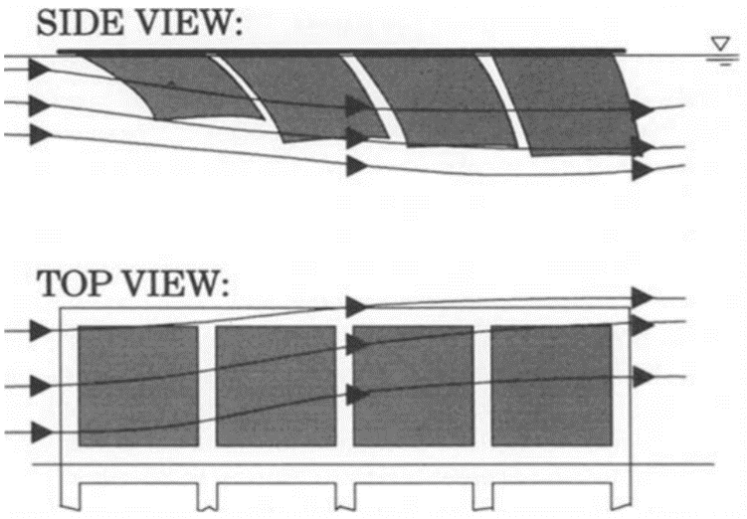

Figure 2.1: Principal illustration of flow through system of net cages (Løland, 1993)

The fish cages used in Norway today mostly use flexible knotless nets made of nylon. In order to cope with predator related challenges, other countries have developed fish cages based on metal. Aquaculture in Norway do not face these challenges and can utilize the less costly nylon nets. Fish cages with flexible fish nets might often limit the possibility of farming in locations with strong current, since the main challenge related to the flexible fish nets is the ability to maintain sufficient volume and fish welfare in strong currents (Sunde et al., 2003)

The development in fish net technology are mainly based on scaling up and increasing the fish net size. On the material side, there has only been minimal development when considering new types of nylon and the development is mainly based on upscaling the previous models. The fish nets are manufactured based on the farming location and the sea-states they must endure, e.g. with extra thickness and strength for locations with strong current (Sunde et al., 2003). To keep the fish net extended and maintain sufficient volume in strong currents, a heavy weight is connected to the bottom as illustrated in Figure 2.2 .

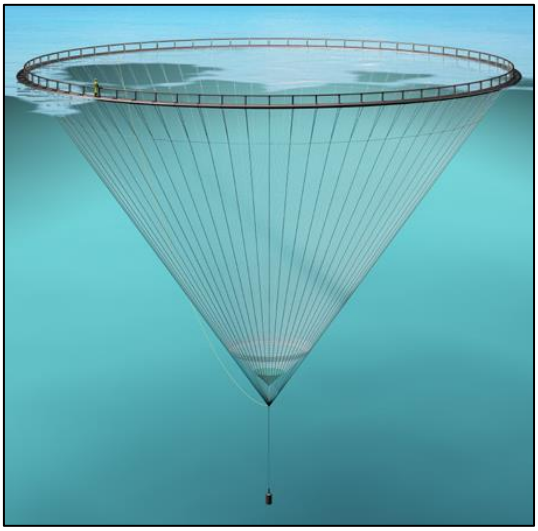

Figure 2.2: Conical-shaped fish farm (Egersund Net, 2016)

For the time domain simulations carried out in this thesis, the nets are modelled by dividing the cage into super elements, which contain properties that simulate the nettings knot and twine structure. The fish nets are modelled using slender elements in SIMO-Riflex, and the hydrodynamic drag and lift components on the net element is calculated by means of coefficients that are dependent on the nets solidity ratio. Further details on the modelling of fish nets are presented in Chapter 5.2.2.

2.3.1 Drag and Lift Forces on Fish Nets

Drag and lift forces on the fish nets in this thesis are calculated using the drag and lift term in Morisons formula. Furthermore, the drag and lift coefficients are found from the nets solidity ratio. For time domain simulations, SIMO-Riflex requires the input of solidity ratio to compute the drag and lift forces on the fish nets. The mean drag (F_d) and lift (F_l) force on a net panel are (Aksnes, 2016):

$$F_d = \frac{1}{2}\rho C_d(\theta) A U^2 \tag{2.21}$$

$$F_l = \frac{1}{2}\rho C_l(\theta) A U^2 \tag{2.22}$$

Where ρ is the water density, A is the area of the net panel, U is resultant velocity vector, θ is the angle between the normal of the panel and the current direction, Cd is the drag coefficient, and Cl is the lift coefficient. The empirical drag and lift coefficients are based on model test data and given as (Aksnes, 2016):

$$C_d = 0.04 + (-0.04 + 0.33S_n + 6.54S_n^2 - 4.88S_n^3)\cos\theta \tag{2.23}$$

$$C_l = (-0.05S_n + 2.3S_n - 1.76S_n^3)\sin 2\theta \tag{2.24}$$

Where θ is the angle of the net and Sn is the solidity ratio, i.e. the ratio between the area projected by the net panel and the total area contained within the frame of the panel. For a knotless net with square shaped screen, Sn is expressed:

$$S_n = \frac{2d}{\lambda} - \left(\frac{d}{\lambda}\right)^2 \tag{2.25}$$

Where λ is the mesh size and d is the twine diameter. Note that the mathematical formulation and results found in Figure 2.4 is not valid for very large solidity ratios, i.e., when the net approaches a solid sheet, since other effects govern the wake behaviour in those cases. Figure 2.3 illustrate a square shaped screen and the parameters used to find the solidity ratio.

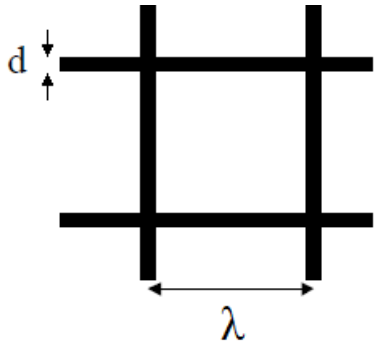

Figure 2.3: Basic definition of a net with parameters.

When the fish net is submerged in the sea over a long period of time it tends to get overgrown with different marine organisms. Marine growth or fouling can change the behaviour of the net, and must be considered when the installation is intended to stay submerged for a long period of

time. As an approximation, fouling can be modelled as an increase in the nets solidity, and the effect of fouling can be estimated by comparing nets with different solidity (Lader and Fredheim, 2006). This is the applied procedure in this thesis, considering the vessel is planned to operate in open sea for long periods of time.

2.3.2 Velocity Reduction Factor

The current force on a net cage is a function of the square of the velocity. In order to obtain correct force calculations, it is therefore of major importance that the velocity description is accurate. This is especially important when several net cages are situated in a row each behind the other, such as the case studied in this thesis. Since the velocity reduction factor alters the velocity, it is an important factor to include in numerical studies of fish farms. The velocity reduction factor is a function of the nets drag coefficient and by that also a function of the solidity ratio. Figure 2.4 below shows the drag coefficient C_D and the velocity reduction factor r, as functions of the solidity.

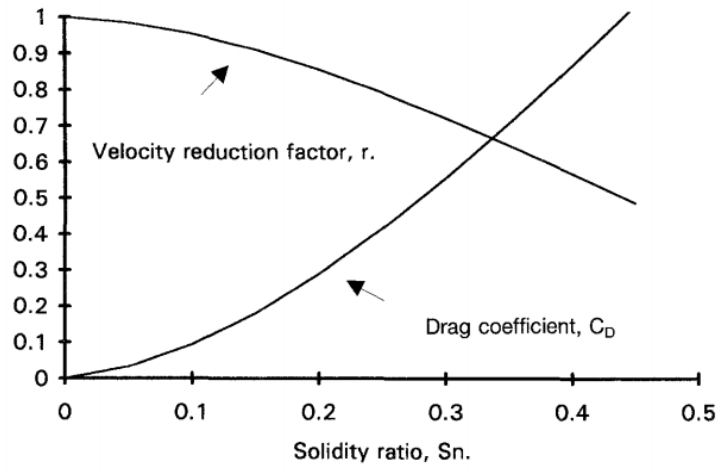

Figure 2.4: Drag coefficient and velocity reduction factor, as function of solidity ratio (Løland, 1993)

A simple expression for the velocity reduction behind a panel $u = rU$ was given by Løland (1991), where u is the velocity in the wake behind the panel and $r = 1 - 0.46CD$ is an empirical reduction factor. In the simulation program SIMO-Riflex utilized in this thesis, the velocity reduction factor is implemented as an explicit input parameter (Aksnes, 2016). Figure 2.5 illustrates the velocity profile behind a 2D screen with a width of 10 m for different distances downstream. The initial velocity is $u = 0.8 * U$, which is approximately the velocity behind a

net cage with solidity of $S_n = 0.17$. From the figure, it is clear that the wake exists very far downstream, in the order of several hundred times the screens dimension. However, the results are based on the assumption of completely uniform free flow, with no disturbances in the fluid besides the wake generated by the net. Even though the wake will vanish more rapidly downstream in reality, it is clear that a wake will exist very far downstream, further uttering the importance of implementing the velocity reduction factor.

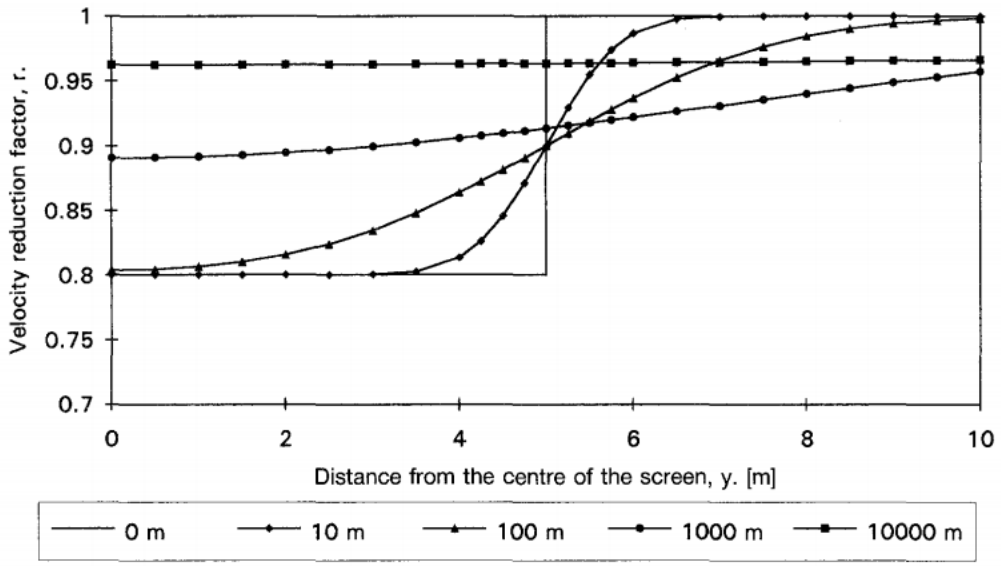

Figure 2.5: Wake velocity behind a screen, width of 10 m and initial velocity u=0.8·U (Løland, 1993)

2.4 Mooring System

Steel linked chain and wire rope are the most commonly used types of mooring lines for floating vessels and platforms. These lines form a catenary mooring configuration, which can be described as the resulting shape of a free hanging line affected by gravity (Gudmestad, 2015). To produce restoring forces as the surface vessel is displaced by environmental loads, the lines rely on an increase or decrease in line tension, from lifting or settling on the seabed (Chakrabarti, 2005). The line tension increases with the horizontal offset of the vessel, as more of the mooring line is lifted from the seabed. Thus, the spread mooring line system used in this thesis generates a nonlinear restoring force to provide station keeping for the vessel.

Following the requirement to operate in increasingly deep-water locations, the weight of mooring lines have come to be a prohibitive factor. Consequently, advances in fibre rope technology have been developed in recent years to enable deep water mooring. Fibre ropes have been installed as mooring systems to reduce line length, mean and low frequency platform offsets, fairlead tension, and the total mooring cost for vessels operating at particularly deep water locations (Chakrabarti, 2005). For the case studied in this thesis however, the vessel-shaped fish farm will operate close to shore and deep-water mooring is not deemed necessary. The water depth is limited to an adequately low value, where there exists a more extensive experience from use of chain mooring lines, making chain mooring lines more applicable and cost-effective. Furthermore, the use of connectors require special attention to fatigue, and their use is not recommended for permanent moorings (Chakrabarti, 2005).

Primarily, there are two chain constructions used for station keeping today; the stud-link chain and the studless chain. The stud-link chains have traditionally been used for mooring of FPSOs (Floating Production, Storage and Offloading) in relatively shallow water since the studs provide stability that facilitate the installation and removal of mooring lines. For permanent moorings however, the studless chain has been the preferred choice. The studless chain have a higher strength per unit weight and increased fatigue life, at the expense of making the installation and removal less convenient. The vessel-shaped fish farm will conduct its operations in the same location for long periods of time, and studless chain is therefore chosen for station keeping.

Monohulls, semi-submersibles, and FPSOs have traditionally been moored with spread catenary systems, with the mooring connections being at various locations on the hull. For a vessel with fixed heading, the environmental loads can be immense due to of excessive offsets. The single point mooring (SPM) system have been developed to overcome this disadvantage, and the vessel is then free to weather vane. However, the SPM system involves many complex components and is subjected to several limitations. Turret mooring systems developed in recent years are therefore considered to be more profitable and reliable than SPMs (Chakrabarti, 2005).

The turret can be either internal or external, and both systems are widely used today. Internal turrets are generally located near the vessels bow, but have been located amidships for a

considerable number of vessels. In order to avoid environmental loading from extreme conditions, disconnectable turret mooring systems have also been developed. The mooring system is then designed to withstand harsh ocean environments, and to be disconnected from the turret whenever encountering a too severe sea state (Chakrabarti, 2005). The internal disconnectable turret system is utilized for the vessel-shaped fish farm studied in this thesis. The turret is located at the bow of the vessel, so that the risk of physical contact of fish nets and mooring lines is reduced. Figure 2.6 illustrates one internal disconnectable turret and one permanent internal turret.

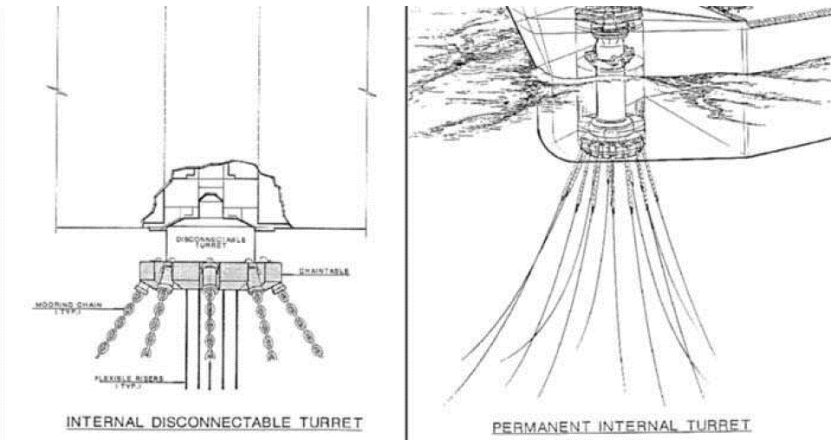

Figure 2.6: Internal and external turret (Chakrabarti, 2005)

Former mooring systems for FPSOs have primarily been passive systems. In recent times however, some mooring systems are used in conjunction with dynamic positioning systems using thrusters. The dynamic positioning systems decrease the loads on the mooring system either by assisting in turning the vessel or by reducing the vessels horizontal offsets when necessary. Summarized, the conjunction of mooring lines and a dynamic positioning system would benefit the vessel-shaped fish farm with:

- a reduction in hydrodynamic loads on due to faster and more proficient weathervaning,
- reduced offset and mooring tension when thrusters move against heading sea,
- possibility to disconnect in storms/harsh weather and move inshore to wait for weather.

The vessel-shaped fish farm should therefore exploit both mooring lines and a dynamic positioning system for station keeping. For simplification purposes, the thruster forces from a

dynamic positioning system will not be included in simulations carried out in this thesis. It is however assumed that the vessel can disconnect and move to a safe location for more severe weather conditions than those studied in this thesis.

The vessel-shaped fish farm will be anchored to the seabed with six catenary chain mooring lines. All the mooring lines are attached to the vessel in a turret located near the vessels bow. This enables the vessel to rotate around the turret and weathervane, thus always facing the main wave and current directions. Weathervaning will result in lower tension in mooring lines by reducing the environmental loads on the vessel and the vessel motions.

The equations used for calculation of the catenary mooring line configuration can be found below. Static mooring line calculations are carried out in MATLAB and results are presented in Chapter 4.2.

$$H = T_{pre} * \cosh(\phi) \tag{2.26}$$

$$y = \frac{H}{W}(\cosh\frac{W}{H}x - 1) \tag{2.27}$$

$$L = \frac{H}{W}\cosh^{-1}\left[\frac{W}{H}h + 1\right] \tag{2.28}$$

$$s = \frac{H}{W}(\cosh\frac{W}{H}L - 1) \tag{2.29}$$

$$T = \sqrt{H^2 + (Ws)^2} \tag{2.30}$$

Where T_{pre} is the pretension, ϕ is the preangle, y is the geometry of the mooring line, L is the horizontal distance to touchdown point, s is the length of catenary, T is the total mooring line tension, H is the horizontal force, W is the weight per length unit in water, and h is the water depth.

2.5 Waves and Currents

The standard DNV-RP-C205 by DNV GL is used as a theoretical background for this chapter. Waves is a result of wind activity over an area of water and actions of higher wind velocities over a larger area of sea, for a longer period of time, will generate higher waves. The wave height also depends on the wave to wave interaction, hence smaller waves can grow into higher waves by energy exchange through interaction with themselves and wind actions (Gudmestad, 2015).

Sea states are stochastic by nature and it is a challenging task to model the sea surface elevation. Thus, several simplifications and methodologies have been developed to depict the sea state conditions. One of the simplified ways to describe the sea state, is the regular wave concept. Waves are in general characterized as either regular waves or irregular waves.

2.5.1 Regular Waves

A regular wave propagates with a permanent form and has a distinct wave height, wave period, and wavelength. Furthermore, the waves propagate with a propagation velocity known as the phase velocity. The phase velocity c of a wave is related to the specific wavelength L and wave period T, as presented in Equation 2.31 below.

$$c = \frac{L}{T} \tag{2.31}$$

The wave frequency (f) denotes the number of completed wave cycles per second, i.e. the inverse of the wave period, and is expressed as:

$$f = \frac{1}{T} \tag{2.32}$$

The wave number k and angular frequency Ω are essential parameters used to depict regular waves, and are both related to the wavelength and wave period, as can be seen in Equation 2.33 and Equation 2.34.

$$k = \frac{2\pi}{T} \tag{2.33}$$

$$\Omega = \frac{2\pi}{T} \tag{2.34}$$

The wave height H is the vertical distance from trough to crest. Wave height can therefore be expressed by the sum of the wave crest height A_C and the wave trough depth A_T. Where A_C is the distance from still water level to crest and A_T is the distance from still water level to trough.

$$H = A_C + A_T \tag{2.35}$$

Regular waves can be categorized as either linear or nonlinear. For linear regular waves, the waves are symmetric about the still water level and the crest height is therefore equal to the trough depth, $A_C = A_T$. For nonlinear waves however, the waves are asymmetric and the phase velocity depends on the dispersion relation, i.e. a relation between H, T, and L.

Multitudinous wave theories have been developed for cases with constant water depth (d). These theories determine the relationship between the water particle motion, the wave period, and the wavelength. The Airy wave theory, which is often referred to as linear wave theory, is applied in the present work. From this wave theory, it follows that all waves applied throughout this study are linear waves.

2.5.2 Linear Wave Theory

The ocean waves in a true sea are built up of several nonlinear components from different directions, generated by wind over variable distances. There are many factors that influence the ocean waves, e.g. viscosity, current interaction, tides, coast lines, natural and man-made obstacles. In order to simplify the complexity of ocean waves, reasonable approximations have been developed by assuming incompressible, irrotational, inviscid fluid flow, and utilizing linear wave theory (Faltinsen, 1990).

Linear theory can be used to simulate irregular seas as a sum of a large number of wave components with different frequencies. According to linear wave theory, the free surface elevation for long-crested waves travelling in the positive x-direction is given by Eq. 3.73

The linear wave theory is considered the core theory of ocean surface waves used in ocean engineering and naval architecture. Linear wave theory is also referred to as small amplitude wave theory, Airy theory, or sinusoidal wave theory. This theory is obtained by assuming the wave height is much smaller than both the wavelength and water depth.

The theory derived in this thesis is from linear wave theory. Hence, the surface conditions are linearized. From linearization, we obtain sinusoidal waves which are applicable for many applications. Linear wave theory is based on these assumptions:

- Wave amplitude is small compared to the wavelength
- Body stays at its mean position
- Body motion is of the same order as the wave amplitude

From linear wave theory in combination with the boundary conditions and assumption of incompressible and non-rotational flow, we obtain the velocity potential function:

$$\varphi(x,z,t) = \frac{\xi_0 g}{\omega}\frac{\cosh(k(z+d))}{\cosh(kd)}\cos(\omega t - kx) \tag{2.36}$$

Where ξ_0 is the wave amplitude, ω is the wave angular frequency, t is the time, k is the wave number, and g is the gravitational acceleration.

2.5.3 Irregular Waves

The free surface elevation of the sea is irregular with stochastic random waves. The irregular random waves represent a real sea state, and can be modelled as a summation of sinusoidal wave components (DNV GL, 2014). Wavelength of irregular waves is defined as the distance between two consecutive zero up-crossings. In addition, the wave crest in a random irregular sea is defined as the global maxima between one up-crossing and the consecutive down-crossing.

In a sea state, the wave condition is categorized as wind seas and swells. The local wind gives rise to wind seas, but has no effect on the swells. Swells are generated by wind affecting a distant area, where wind blows over a fetch of water, and are therefore superimposed into the incoming sea wave. Since the swells have travelled out of the areas where they were generated, multiple swell components may simultaneously be present at a location. As a result of this, the wind sea will follow the local wind direction, while the swell is omnidirectional. Analysis of offshore structures that are sensitive to different propagation directions should therefore identify, and include, the most unfavourable sea states (Ishie et al., 2016).

As previously mentioned, irregular random waves can be modelled as a summation of sinusoidal wave components and will then represent a real sea state. The simplest random wave model is the linear long crested wave model given by:

$$\eta_1(t) = \sum_{k=1}^{N} A_k \cos(\omega_k t + \varepsilon_k) \tag{2.37}$$

Where ε_k are random phases uniformly distributed between 0 and 2π, mutually independent of each other and of the amplitudes A_k, which are random and Rayleigh distributed with mean square value given by:

$$E[A_k^2] = 2S(\omega_k)\Delta\omega_k \tag{2.38}$$

Where $S(\omega)$ is the wave spectrum and $\Delta\omega_k = \omega_k - \omega_{k-1}$ is the difference between successive frequencies.

2.5.4 Wave Spectra

The power spectral density function of the vertical sea surface displacement is called a wave spectrum, and is used to describe the short-term stationary irregular sea in this thesis. Several numerical approximations of wave spectra have been developed over the years, including the Pierson-Moskowitz (PM) spectrum, developed by Pierson and Moskowitz (1964) from measurements in the North Atlantic. The PM wave spectrum is regarded as one of the simplest ways of describing a fully developed sea, and assumes that the wind blows steadily for a long

time over a large area so that the waves reach equilibrium with the wind. The PM spectrum was extended by a group of researchers in the Joint North Sea Wave Project, forming the JONSWAP spectrum (1973). The JONSWAP spectrum is regarded as the most relevant spectrum for numerical approximations of North Sea conditions, and has therefore been used to model irregular wave conditions in this thesis.

The sea states used to model irregular seas can be either short-term or long-term sea conditions. Long term sea state is characterised by probability of exceeding an environmental parameter or a return period. For short-term sea states on the other hand, the sea surface is assumed stationary for 3-6 hours. The stationary sea is described by two environmental variables, namely the significant wave height H_s and the wave peak period Tp. The significant wave height is either defined as the mean wave height of the highest one-third of the waves measured within a time period, or as four times the standard deviation of a surface elevation. The peak period can be defined as the inverse of the frequency at which the value of the frequency spectra has its maximum value. For certain cases, the wave direction, θ, and wave peakedness, γ, are input parameters which are necessary to obtain the random sea state. This is the case for the JONSWAP wave spectrum used in this thesis, which also requires the input of spectral width parameters, σ_a and σ_b. The JONSWAP wave spectrum can be expressed as (DNV GL, 2014):

$$S_J(\omega) = S_{PM}(\omega)(1 - 0.287ln\gamma)\gamma^{\exp\left(-0.5\left(\frac{\omega-\omega_P}{\sigma\omega_p}\right)^2\right)} \tag{2.39}$$

Where $S_{PM}(\omega)$ is the PM spectrum, γ is the non-dimensional peak shape parameter, and σ is the spectral width parameter. From average values for JONSWAP experiment data, the spectral width diameter is (DNV GL, 2014):

$$\begin{aligned} \sigma = \sigma_a = 0.07\ for\ \omega \leq \omega_P \\ \sigma = \sigma_b = 0.09\ for\ \omega \leq \omega_P \end{aligned} \tag{2.40}$$

Further, the non-dimensional peak shape parameter γ is found from the following three equations:

$$\gamma = 5 \quad \text{for} \quad \frac{T_P}{\sqrt{H_S}} \leq 3.6 \tag{2.41}$$

$$\gamma = \exp\left(5.75 - 1.15\frac{T_P}{\sqrt{H_S}}\right) \quad \text{for} \quad 3.6 < \frac{T_P}{\sqrt{H_S}} < 5 \tag{2.42}$$

$$\gamma = 1 \quad \text{for} \quad 5 \leq \frac{T_P}{\sqrt{H_S}} \tag{2.43}$$

2.5.5 Currents

Large net deformations occur from strong currents and current forces depend highly on the magnitude of net deformation. It is also acknowledged that certain volume within the fish cage must exist in order to maintain fish welfare. Furthermore, the design of mooring lines also relies on an accurate assessment of current and wave forces on the total system (Kristiansen and Faltinsen, 2012). Qualitatively, it is therefore obvious that the design and analysis of offshore aquaculture systems should include the effects of combined wave and current forces (Fredriksson et al., 2005).

The current velocity varies with water depth, and the current velocity profile is either stretched or compressed by cause of surface waves. In general, the current velocity varies in space and time, where the time-dependency is a result of flow fluctuations caused by turbulence (DNV GL, 2014).

$$V_c = V_c(x, y, z; t) \tag{2.44}$$

Total current velocity should be taken as the vector sum of all present current components at the location, e.g. wind generated, tidal and circulational currents. For most applications however, the current velocity can be considered as a steady flow field with a velocity vector as a function only of water depth.

Variation of current velocity over water depth depends on the oceanographic climate of the location, the vertical density distribution, and the flow of water in or out of the area. These factors may vary from season to season and the water profiles may be complex, with current directions altering by up to 180 degrees. However, if detailed field measurements are not available, the variation in current velocity with water depth can be modelled as a simple power law, assuming unidirectional current (DNV GL, 2014).

In this thesis, the current is assumed unidirectional for a uniformly distributed current with constant velocity over varying water depth. This assumption is made to simplify the modelling and to simulate worst case scenario for the vessel-shaped fish farm. The assumption will result in higher current velocities at lower water depths and eliminate the risk of underestimation of the hydrodynamic forces on the nets and mooring lines for a given current velocity.

2.6 Time Domain Finite Element Method

For the time domain analysis, waves with specified wave heights and periods are time-stepped through the structure. The response of the structure is then computed for each time step with a chosen duration length. Time domain analysis demands more computer resources than the frequency domain approach, but is more flexible when including multiple bodies and combination of waves and current conditions Bachynski (2014).

Design of offshore aquaculture systems is a novel and unique engineering challenge, where the system components alone might be technically simple, but to dynamically represent the system as a whole is a complex and demanding task. For these systems, an analytical approach would require an excessive amount of assumptions and would doubtfully result in sufficiently accurate solutions (Fredriksson et al., 2003). Methods that utilize numerical and physical models are therefore used in the dynamic structural analysis of such systems.

In this thesis, frequency domain analysis is used to find the vessel motion in heave, pitch, and roll. Furthermore, the frequency domain analysis provides essential input values for time domain analysis. The time domain analysis is first performed using the numerical simulation program SIMO and then using SIMO-Riflex. SIMO is used to conduct a simplified (quasi-

static) coupled dynamic analysis of the vessel with mooring system, and SIMO-Riflex is used to conduct a fully coupled dynamic analysis of the vessel with mooring system and fish nets.

2.6.1 Nonlinear Finite Element Analysis

Analyses from Finite Element Method (FEM) uses a numerical integration method that approximates the solution of differential equations of motion and divides the structural component into small elements with a decreased number of displacement patterns. Nonlinear FEM accounts for secondary effects, e.g. large displacements, nonlinear material behaviour and changing boundary conditions. The secondary effects introduce a memory effect and traditional mechanic principles, such as superposition of loads and responses, are then considered insufficient. The simulation program SIMO-Riflex addresses the geometric nonlinearities in the nonlinear FEM analysis.

The nonlinear equation of motion can be expressed by global matrices containing mass, damping, and stiffness properties of the finite elements as in Equation 2.45 (MARINTEK, 2016b) The external forces arise from buoyancy, weight, viscous drag and wave acceleration forces, and forced displacements from attached bodies.

$$(M^S + M^H)\ddot{r}(t) + C^S\dot{r}(t) + K^S\big(r(t)\big) = R^{EXT}(r(t), \ddot{r}(t)) \tag{2.45}$$

Where R^{EXT} consist of forced displacements, velocities, and accelerations from the rigid floating structure motion from the coupled solution. The nonlinearities are significant and of great importance for the vessel-shaped fish farm system studied in this thesis. The FEM solver in SIMO-Riflex applies the Newmark-β method implicit integration to locate the dynamic equilibrium for each time step (MARINTEK, 2016b). The Newmark-β method assumes small strains and the parameters control the numerical stability, numerical damping, and accuracy of the integration, whilst allowing unlimited displacement (Ishie et al., 2016).

2.6.2 Coupled Analysis

In order to simplify the numerical model and reduce the experimental difficulties, many studies have considered the floater and net structures as separate components. Fredriksson (2001) and Fredriksson et al. (2003) first measured the wave spectra, current, mooring tensions, and the

motion responses of a fish cage during an extreme storm. Then, numerical simulations were carried out using the measured data as input for a dynamic FEM. This method of approach is however highly unrealistic, as the floater and nets have strong interaction with each other. The interaction between these components and their force contribution to the system is of great importance in assessing the vessel-shaped fish farm (Fu et al., 2014).

The vessel-shaped fish farm consists of three dependent components; the floating rigid structure, mooring lines, and fish nets. The dynamic response analysis of these individual components can be carried out by conventional quasi-static software analysis tools or in frequency domain. The coupling effect from these components are however significant when considered as a whole system, and thus a coupled analysis must be performed. The Finite Element solver is separate for these components, and will not include coupling effects between them. However, in order to take the coupling effects into consideration, the solvers exchange information at each time step of the analysis.

In the coupled analysis, the mooring lines and fish nets are flexible elements, which are connected to the rigid vessel at common super nodes. At each time step, the dynamic equilibriums for the flexible elements and the rigid vessel are resolved separately. However, the information about external forces and displacements are simultaneously exchanged between the solvers (MARINTEK, 2016b). Equilibrium is therefore obtained for the FEM equations through iteration at each time step.

3 Hydrodynamic Analysis – Vessel in Frequency Domain

Physical phenomena can be observed and described by either the time domain or the frequency domain. In the time domain, phenomenon specified by observable quantities appear as a developing process. This process is described in the time domain by simply listing the quantities as simultaneous functions of time. Time is not a parameter in the frequency domain, and the observables of the phenomenon are left as stationary, interrelated spectra of harmonic components (Gran, 1992).

The analysis may be static or dynamic and require limited computer resources, thus reducing the computational expenses. In the present thesis, a single rigid submerged body is modelled and used in frequency domain analysis. The single rigid body is a simple form of a dynamic structural model and the six traditional global motions of this rigid vessel can then be found, namely: surge, sway, heave, roll, pitch, and yaw.

A frequency domain analysis was performed to study the hydrodynamic properties of the vessel, and investigate the vessel motions in heave, pitch, and roll. Furthermore, the frequency domain analysis provides essential input values for time domain analysis. One wave period and three wave directions were selected for frequency domain analysis in this thesis, and this was assumed to result in sufficient descriptions of the vessel motions. The accuracy of simulation results is improved through optimization of the frequency set and panel models mesh. Modelling principles related to the fineness of the panel models mesh was therefore adhered to and a convergence study performed.

3.1 Numerical Analysis Program and Input

It is challenging to accurately predict the motions of offshore structures and different software is therefore used as calculation tools. Computational Fluid Dynamics based on Navier-Stokes equations with turbulence modelling is considered the most sophisticated way to handle the viscous effects. However, it is computationally too expensive to use this method in the design

loop for offshore structures, particularly in the early design phase (Shao et al., 2016). The DNV GL software Wadam, from the application HydroD, was therefore used to obtain the hydrodynamic properties of the vessel from frequency domain analysis. HydroD is an interactive application for computation of hydrostatics and stability, wave loads, and motion response for ships and offshore structures. The wave loads and motions are computed by Wadam in the SESAM suite of programs (DNV, 2011).

Different wave directions will result in different RAOs. Three wave directions are used for frequency domain analysis in this thesis. The wave directions are set to 0, 45, and 90 degrees, where the waves from a direction of 0 degrees are the heading sea and encounter the vessels bow head on. The vessel will weathervane and wave directions from larger angles are therefore neglected. Furthermore, the vessel is axisymmetric and wave directions of 0, -45, and -90 degrees will have identical simulation results as those of 0, 45, and 90 degrees.

Input describing the location by water depth, water density, air density, and kinematic viscosity and gravitational acceleration must be included in all frequency domain analysis. As previously mentioned, the water depth is set to 120 meters and is used for all simulations throughout this thesis. Figure 3.1 below illustrates the submerged section of the vessel, with wave directions and water depth used for simulations in frequency domain.

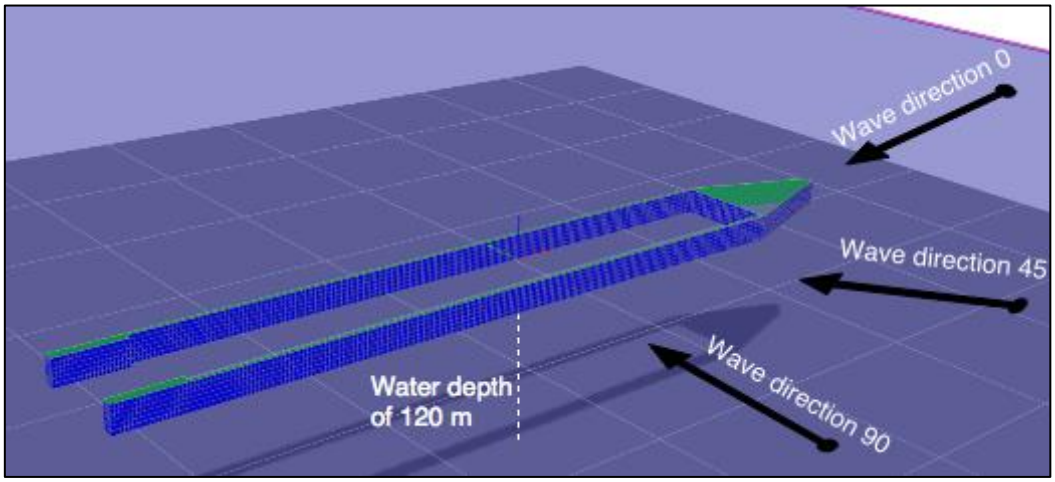

Figure 3.1: Water depth and wave directions for frequency domain analyses

3.1.1 Frequency Set

A frequency set must be chosen to perform hydrodynamic analysis of the vessel. This is done by first setting up a simulation with a linear spread of measurements/frequency to roughly locate the area of amplitude peaks. The more exact location of maximum peak value is then found by increasing the frequency in the area of interest. The hydrodynamic properties heave, roll, and pitch are found from frequency domain analysis in Wadam using the modified frequency set. Computations are normally performed for at least 30 frequencies for a motion analysis of a vessel in the frequency domain (DNV GL, 2014). The frequency sets utilized in this thesis contain 60 frequencies to ensure sufficient measurements and improved accuracy in simulation results.

3.1.2 Panel Model

The panel model consists of quadrilateral panels representing the wet surfaces of the body. The panel method is the discretization of the mean wetted surface into flat panels (DNV GL, 2014). The method uses source points, which are elementary solutions of the Laplace equation. Each panel is prescribed an ideal flow element with a prescribed strength and the Laplace equation is solved subsequently for the inviscid, incompressible flow. The panel model represents the vessel with a series of panels forming the body, and flow properties are calculated for each panel. The panel method has been applied extensively in naval hydrodynamics and aircraft aerodynamics (Erickson, 1990).

For studies of the hydrodynamic properties of the vessel, different panel models were created using the DNV GL design analysis tool GeniE in SESAM. GeniE is an offshore structural engineering software tool for design and analysis of fixed and floating structures. The submerged section of the vessel was modelled based on the assumed dimensions illustrated in Figure 3.2.

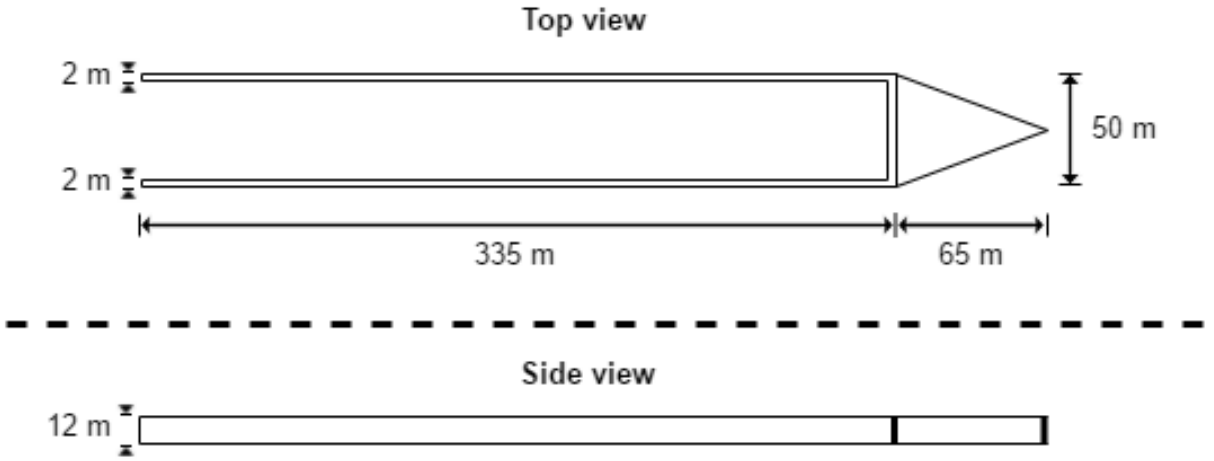

Figure 3.2: Dimensions of vessels submerged section

The panel models are divided into a different number of sections, and the difference between the models is the fineness of their mesh. Convergence tests were carried out to ensure the accuracy of computed loads and motions. Simulation results from panel models with a different number of panels in equal environmental conditions and frequency sets were compared. The different panel models studied for convergence in this thesis were:

- **Panel model 1**: mesh fineness of 1 m long squares overall and a total of 11484 elements
- **Panel model 2**: mesh fineness of 2 m long squares overall and a total of 2978 elements
- **Panel model 3**: mesh fineness of 2 m long squares and a refined area with 1 m squares on the vessels hull. This area contains corners and such abrupt geometry requires a refined mesh to obtain accurate results. The total number of elements is 3911

All three panel models fulfil the principles given in DNV-RP-C205 (DNV GL, 2014):

- Diagonal length of panel mesh should be less than 1/6 of smallest wavelength analysed.
- Fine mesh should be applied in areas with abrupt changes in geometry (edges, corners).
- When modelling thin walled structures with water on both sides, the panel size should not exceed 3-4 times the modelled wall thickness.
- The water plane area and volume of the discretized model should match closely to the real structure.

Since the fine mesh of Panel model 1 contains many elements, the simulation runtime is very long and computationally heavy. Even though the results from simulations run with Panel

model 1 are also the most accurate, the computational requirements are too large for further use in this thesis. It was therefore conducted a convergence study to find the panel model with reduced computational requirements and sufficient accuracy in simulation results.

3.1.3 Composite Model

Large volume structures are inertia-dominated, which means that the global loads due to wave diffraction are significantly larger than the drag induced global loads. Some vessels might also require a Morison load model for the slender members/braces in addition to the diffraction model (DNV GL, 2014). Flow separation will inevitably occur if a structure contains abrupt changes in geometry with sharp corners. For such structures, viscous effects can therefore not be dismissed without further consideration (Sarpkaya and Isaacson, 1981). The vessel-shaped fish farm contains slender elements with sharp corners, and viscous effects must therefore be investigated further. The viscous effects are included in the Wadam simulations by implementing both a Morison element and a defined sea state. The model is then called a composite model, which contains both a panel model and Morison elements.

The composite model is used to apply potential theory and Morison's formula to different parts of the hydro model. The Morison element is used to include added mass and drag forces according to Morison's formula. The hydro property description for a Morison element include added mass and viscous drag coefficients in the two directions perpendicular to the longitudinal element axis (DNV, 2010). The Morison elements are shaped as beams and placed along the vessels sides. This is the area of interest when considering the viscous effects on the vessels RAOs. The RAOs with and without viscous damping are compared to check the contribution from viscous effects.

To add the Morison elements mass and volume to the panel model, Wadam requires that the mass per unit length and the diameter of the Morison element is specified. To reduce the increased total volume and mass, the Morison elements mass per unit length and diameter is given small values compared to the vessel, so that their contribution can be assumed neglectable:

- Mass per unit length: 0.005 kg/m
- Diameter: 0.01 m

Figure 3.3 illustrates the location of the two Morison elements included in the simulation.

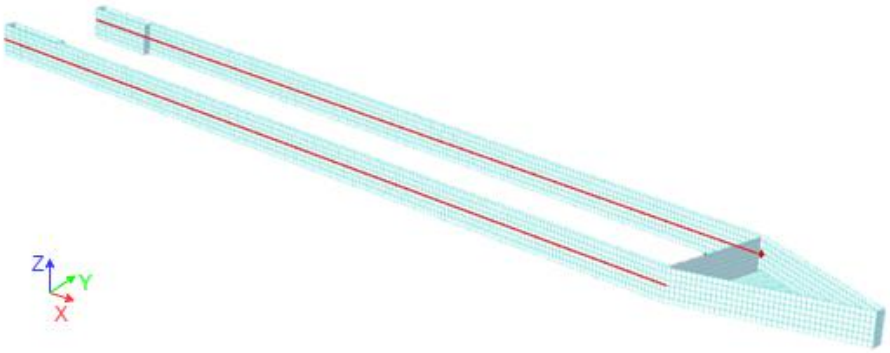

Figure 3.3: Illustration of Morison elements

3.1.3.1 Added Mass Coefficient

The viscous term is included for simulations with a composite model, and the added mass coefficient is a necessary input. The added mass coefficients used in this thesis is found from the fact that the inertia term will dominate for the large geometry of the vessel-shaped fish farm. The Keulegan Carpenter (KC) number is a dimensionless number that describes the relation between drag forces and inertia forces. For dominating inertia term, the KC number has a value lower than 5. For the inertia dominated case studied here in this thesis, the added mass coefficients can be assumed to be independent of KC number and equal to the theoretical value $C_A = 1.0$ for both smooth and rough surfaces (DNV GL, 2014).

3.1.3.2 Drag Coefficient

The drag coefficient is a dimensionless quantity which represents the drag of an object in water, i.e. the objects resistance to movement in water. Drag coefficients are a required input for the Morison element in a composite model. To find values for the drag coefficients, the Reynolds number must be calculated. When calculating the Reynolds number, the motion of the vessel itself is assumed to be zero as the vessel will be moored to the seabed. The vessel movement is limited and the effect on the Reynolds number is negligible. The vessel is therefore assumed stationary for the calculations below. The determination of the drag coefficient for the vessel do not require high accuracy in Reynolds number, thus the surface roughness and thickness of marine growth is neglected.

The Reynolds number is found from the following formulas:

$$Re_{crest} = \frac{u_{max} \cdot D}{v} \tag{3.1}$$

$$u_{\max} = \xi_0 \cdot \omega \cdot e^{k*z} \tag{3.2}$$

$$k = \frac{\omega^2}{g} \tag{3.3}$$

Where:
v is the kinematic viscosity of water

D is the characteristic width

u_{max} is the wave velocity at the wave crest

$k = \frac{\omega^2}{g}$ is the wave number, here for deep water

$\xi_0 = \frac{H_s}{2}$ is the wave amplitude

$\omega = \frac{2\pi}{T}$ is the wave frequency

z is the water depth

g is the gravitational acceleration

The parameters used to calculate the Reynolds number can be found in Table 3.1 below:

Table 3.1: Parameters for calculation of Reynolds number

$\boldsymbol{v}$ $[\mathbf{m^2/s}]$	**D** **[m]**	$\boldsymbol{g}$ $[\mathbf{m/s^2}]$	$\boldsymbol{H_s}$ **[m]**	$\boldsymbol{T}$ **[s]**	$\boldsymbol{z}$ **[m]**
10^{-6}	24	9.81	5	8	2.5 m

Using the above equations and parameters in Table 3.1, the Reynolds number is found to be:

$$Re_{crest} = 55 \cdot 10^6$$

From experiments and numerical simulations of flow normal to a flat plate with corner effects, it is found that the drag coefficient varies from 2 to 2.3 for Reynolds numbers in the range of

250 to $1.5 \cdot 10^5$. It appears that the drag coefficient for flow normal to a plate is not sensitive to the Reynolds number compared to the flow around a circular cylinder. This is because the flow separation point is fixed for the plate corners, while it varies along the surface of a circular cylinder (Tian et al., 2014). The drag coefficient in y-direction is therefore set to 2.3 for the vessel-shaped fish farm. The Morison elements on the vessel and the x-, y-, and z-axis are illustrated in Figure 3.3.

As previously mentioned, the hydrodynamic properties of a Morison element include viscous drag coefficients in the two directions perpendicular to the longitudinal element axis. Thus, the drag coefficient in z-direction must also be included in the simulations. The drag coefficient in z-direction is found from DNV-RP-C205, and is of low value due to the relation between beams width and length in z-direction (DNV GL, 2014). Figure 3.4 below illustrates the relation between the width D, length L, radius R, and wave direction used to determine the drag coefficient.

Rectangle with rounded corners

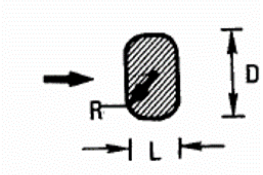

L/D	R/D	C_D	L/D	R/D	C_D
0.5	0	2.5	2.0	0	1.6
	0.021	2.2		0.042	1.4
	0.083	1.9		0.167	0.7
	0.250	1.6		0.50	0.4
1.0	0	2.2	6.0	0	0.89
	0.021	2.0		0.5	0.29
	0.167	1.2			
	0.333	1.0			

Figure 3.4: Drag coefficient for rectangle

The vessel has sharp corners and R/D is thus equal to zero. For flow in z-direction, the length L is 12 meters and the width D is 2 meters, which results in the relation $L/D = 6$. The drag coefficient is therefore set to be 0.89.

In addition to surface roughness and Reynolds number, the KC number also affects the drag coefficient. As previously mentioned, the inertia term will dominate and the KC number will be of low value for the vessel-shaped fish farm. Since the KC number is low, the effect on drag coefficient is neglected for simplification purposes in this thesis.

3.1.3.3 JONSWAP Wave Spectrum

Analytical expressions of the wave spectra are used in practice and must be included in the simulation with composite model for stochastic drag linearization. The JONSWAP wave spectrum was established from the Joint North Sea Wave Project, and wave measurements in the Southern North Sea was used to establish the spectrum. The spectrum can describe the sea conditions under developing wave conditions and for fully developed sea conditions (Gudmestad, 2015).

When utilizing the JONSWAP wave spectrum in Wadam, the following input is required:

- Significant wave height, H_s
- Wave period, T_p
- Spectral peak shape parameter, γ
- Spectral width parameters, σ_a and σ_b

The values of σ_a and σ_b are set to 0.07 and 0.09 respectively. These values are the standard in HydroD and are equal to the standard values set in DNV-RP-C205. The significant wave height is set to $H_S = 5\ m$ and the wave period is set to $T_P = 8\ s$. Using these values, the peak shape parameter is set to $\gamma = 5$ from Equation 2.42. The values used for the JONSWAP wave spectrum in the simulations with composite model is found in Table 3.2 below, and Figure 3.5 illustrates the JONSWAP spectrum for these inputs.

Table 3.2: Input for JONSWAP wave spectrum

H_s [m]	T_p [s]	γ	σ_a	σ_b
5	8	5	0.07	0.09

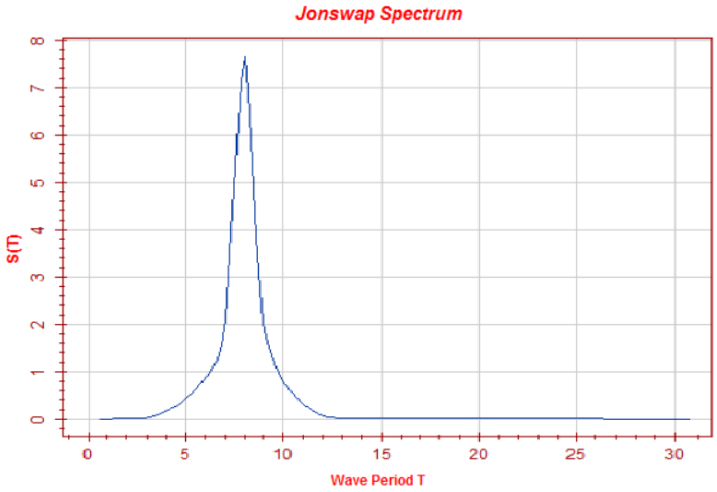

Figure 3.5: JONSWAP wave spectrum from Wadam

3.2 Hydrodynamic Results

The hydrodynamic results are found from conducting a sensitivity study to locate the frequency set to be used for further analysis, and a convergence study of panel models to verify sufficient accuracy in simulation results. A comparison of results obtained from panel model and composite model is performed and the effect of viscous drag and added mass on the vessel RAOs are studied.

3.2.1 Sensitivity Study from Different Frequency Sets

In order to obtain simulation results with sufficient accuracy to be used for further analysis, the frequency set must be optimized to find the true vessel motions. This is done by increasing the frequency of measurements in the area of interest and locate the true peak values for the vessel RAOs. The RAOs for different frequency sets are plotted and compared until the final frequency set is found and used for further analysis.

To roughly locate the peak area for the different RAOs, a linear frequency set was used for the first simulations in Wadam. For the linearly spread frequency set, Figure 3.6 illustrates the amplitude in heave, Figure 3.7 in roll, and Figure 3.8 in pitch. The graphs are not sufficiently accurate and it is necessary to increase the number of measurements in the area of interest, so

that the true peaks and amplitudes are located. From studying the graphs, it was decided to increase the frequency of measurements in the area between 0.4 rad/s and 1.0 rad/s.

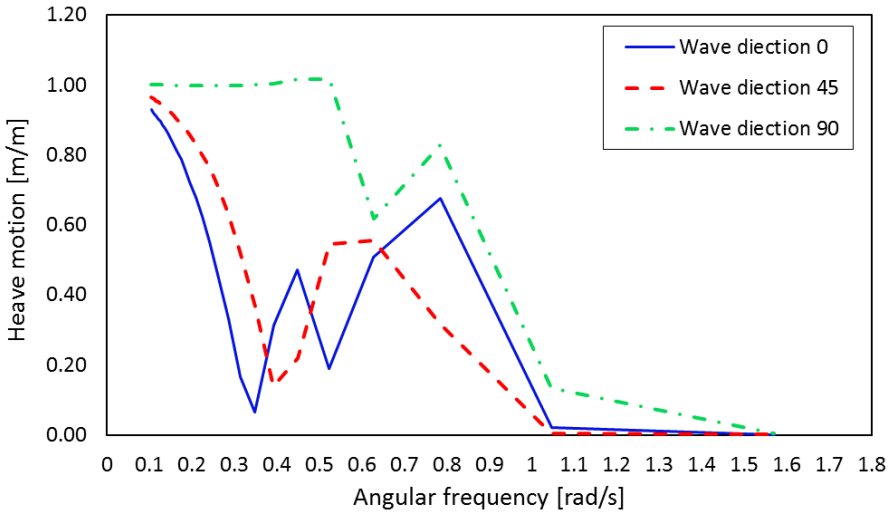

Figure 3.6: Heave low frequency

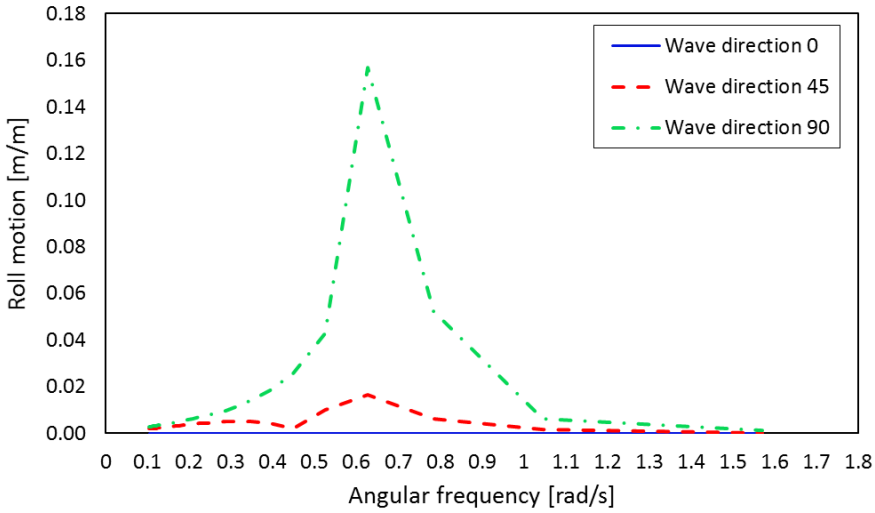

Figure 3.7: Roll low frequency

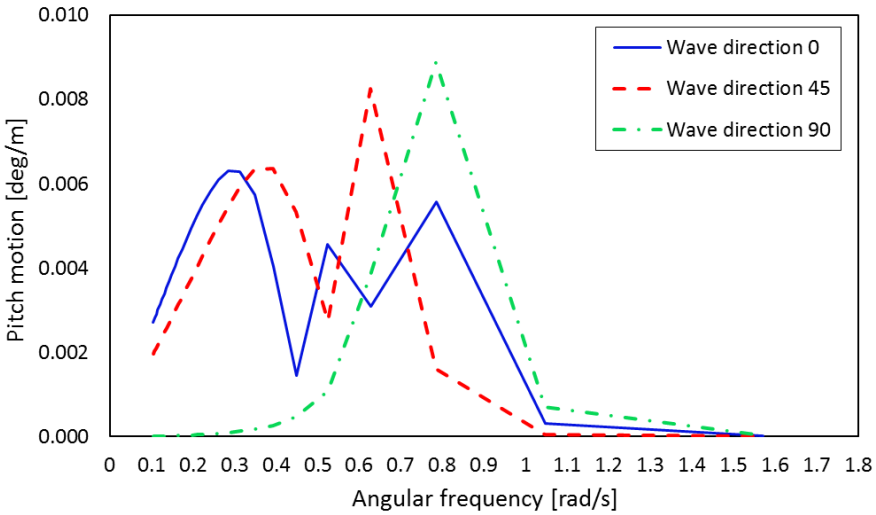

Figure 3.8: Pitch low frequency

The area of interest is located between 0.4 rad/s and 1.0 rad/s for all RAOs investigated. The frequency of measurements was increased for this area using the input function in Wadam. Figure 3.9, Figure 3.10, and Figure 3.11 below illustrates the more accurate results obtained when using modified frequency set in simulation. The results from simulations with increased frequency show the importance of using sufficient frequency of measurements in the peak areas. The graphs are more detailed in the area of interest and thus the amplitude at the different peaks are significantly higher and more representative of the true values. This frequency set was used for convergence study and selection of panel model in Chapter 3.2.2.

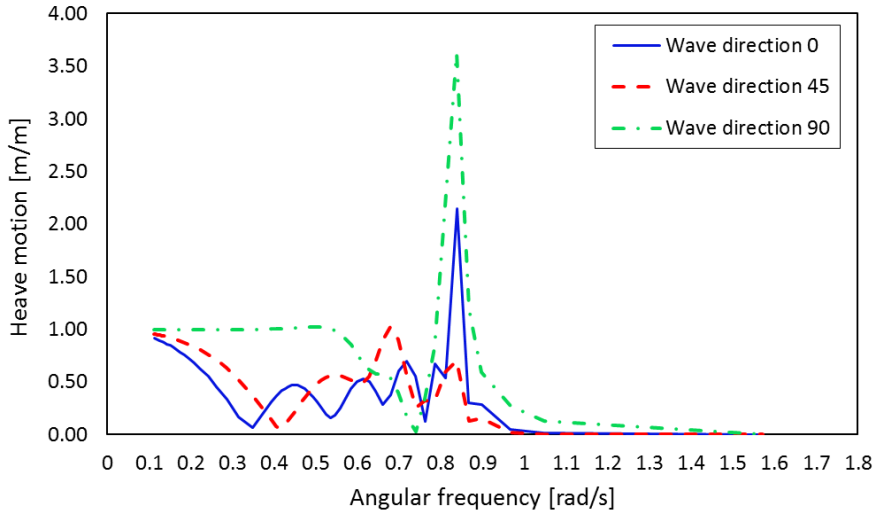

Figure 3.9: Heave modified frequency

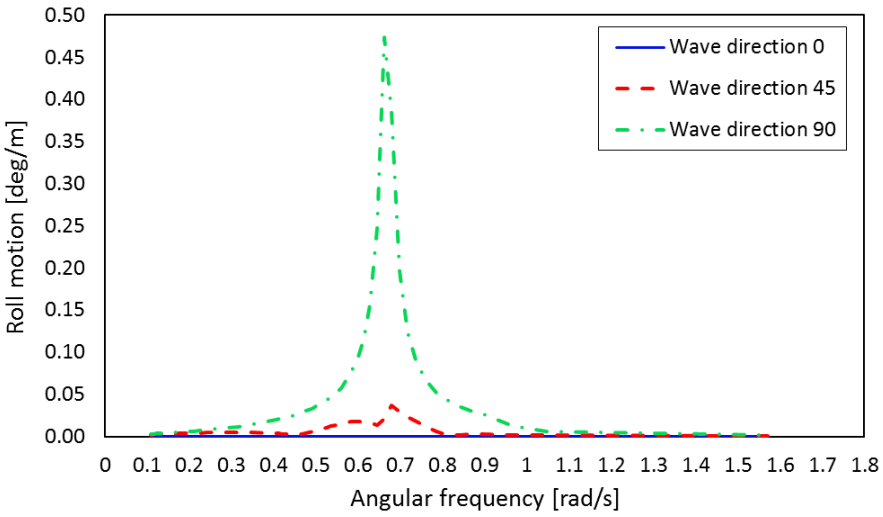

Figure 3.10: Roll modified frequency

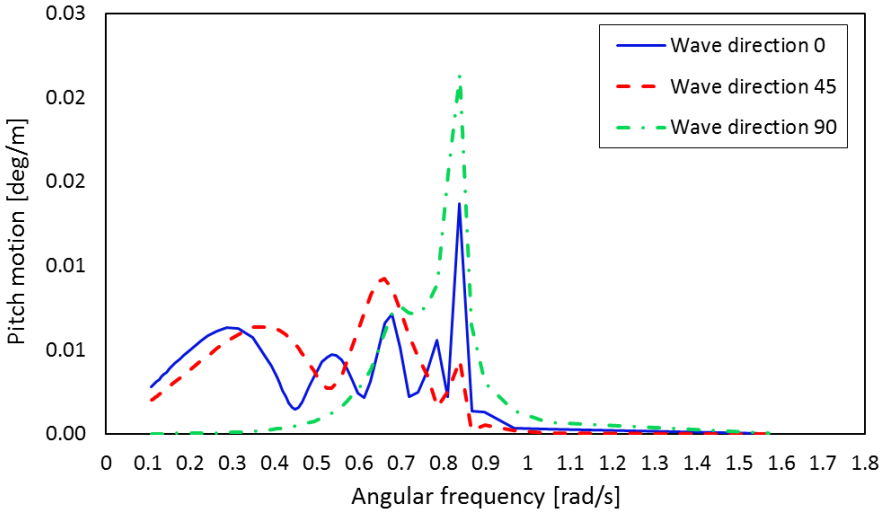

Figure 3.11: Pitch modified frequency

A final frequency set was made after conducting the convergence study and selecting a panel model. The frequency set was altered to increase the accuracy of the vessels RAOs for the chosen panel model and later also the composite model. To obtain more realistic values, a higher accuracy in simulation results are required for analysis of the vessels RAOs, viscous damping, and coupled dynamics. This is achieved from further increasing the number of measurements in the frequency set in the area between 0.6 rad/s and 1.0 rad/s. The vessels RAOs with the optimized frequency set and panel model 3 are illustrated in Figure 3.12, Figure 3.13, and Figure 3.14 below.

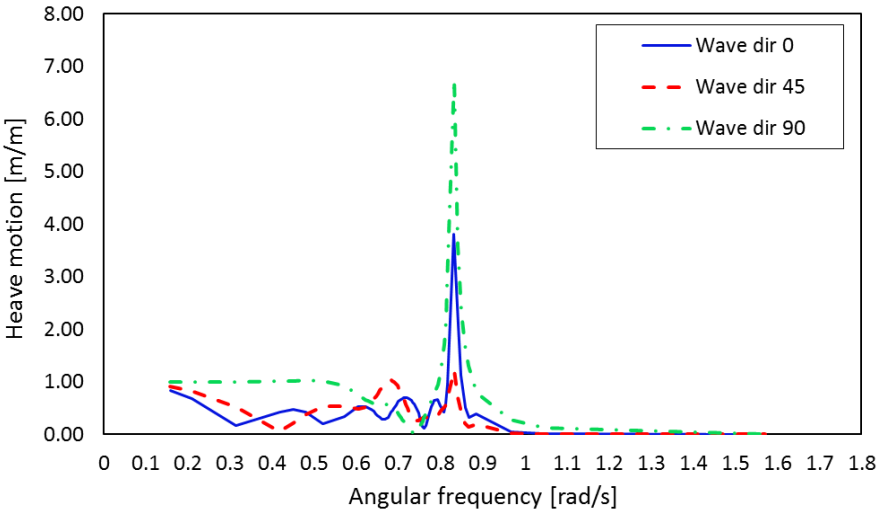

Figure 3.12: Heave final frequency

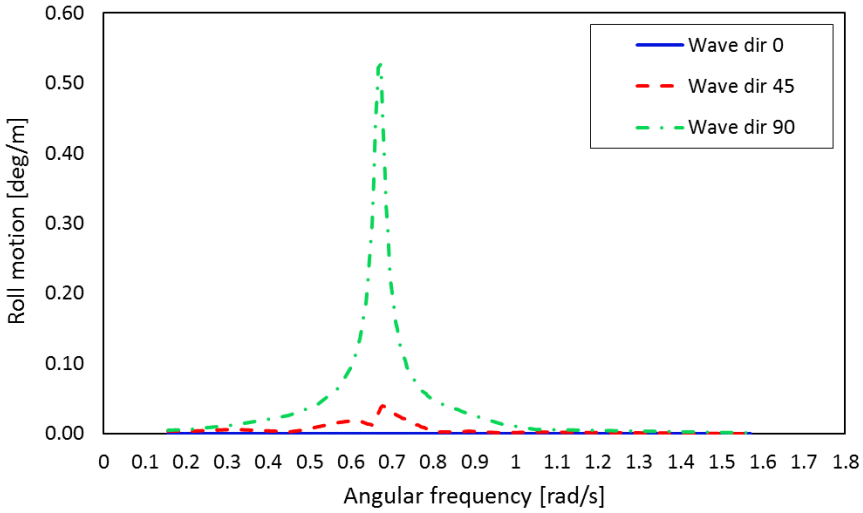

Figure 3.13: Roll final frequency

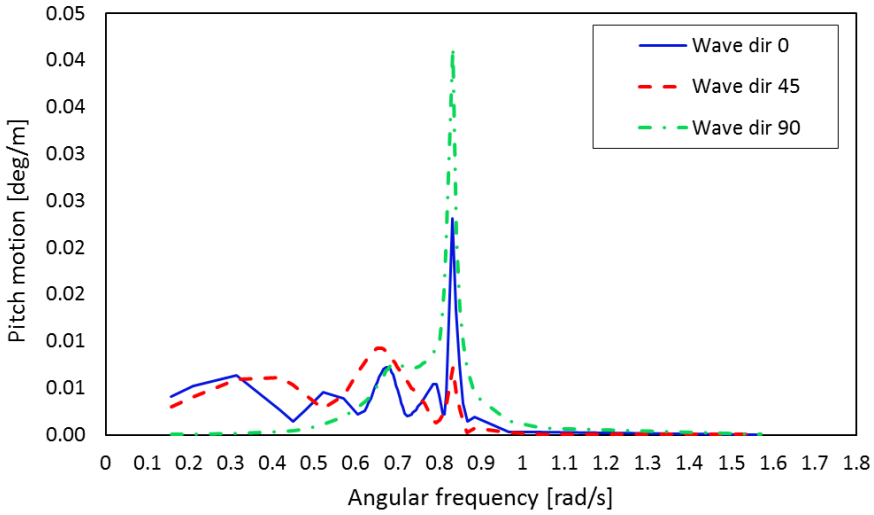

Figure 3.14: Pitch final frequency

When studying the frequency sets, the importance of sufficient measurements in a frequency domain analysis is seen when comparing the different RAOs and their maximum values. Figure 3.15 below shows the different heave RAOs for a wave direction of 0 degrees from the three frequency sets. Additional graphs with comparison of RAOs can be found in Appendix A-1. Table 3.3 below shows the maximum amplitudes for different wave directions, frequency sets and hydrodynamic properties.

Table 3.3: Comparison of frequency sets

Hydrodynamic property	Frequency set	Max. amplitude Wave direction 0	Max. amplitude Wave direction 45	Max. amplitude Wave direction 90
Heave	Linear	0.928	0.964	1.02
	Modified	2.15	1.02	3.63
	Final	3.81	1.23	6.75
Roll	Linear	0	0.017	0.157
	Modified	0	0.037	0.474
	Final	0	0.039	0.527
Pitch	Linear	0.006	0.008	0.009
	Modified	0.014	0.009	0.021
	Final	0.023	0.009	0.041

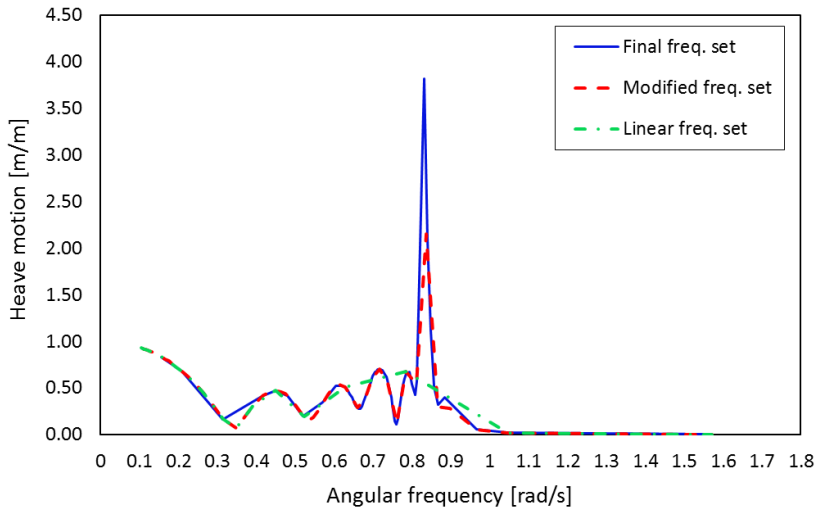

Figure 3.15: Comparison of frequency sets, heave motion for wave direction 0

The importance of sufficient measurements can be seen from the difference in peak values for the different frequency sets. The maximum amplitude from the linear to the final frequency set was increased by:

562% for heave

236% for roll

356% for pitch

From the graphs, one can see that sufficient measurements are especially important in the peak areas, where the difference between the linear frequency set and the optimized frequency set is largest. For measurements outside the peak areas, there is little difference between the three frequency sets.

3.2.2 Convergence Study Using Different Panel Models

The convergence study is performed for different panel models under the same environmental conditions and with the same frequency sets. For the convergence study in this thesis, the modified frequency set developed in Chapter 3.2.1 is used. The runtime for the simulations are therefore only dependent on the panel models and their number of elements. Panel model 1 has a very detailed mesh with many elements, and the runtime is therefore significantly longer than

the other two panel models. Since the two other panel models have a much shorter runtime than panel model 1, the convergence study could result in a tremendous amount of time saved in further studies. Results from the three panel models are compared to check if results from panel model 2 or panel model 3 are accurate enough to be used for further studies. Figure 3.16 below illustrates the difference in mesh fineness for panel model 1 and panel model 2.

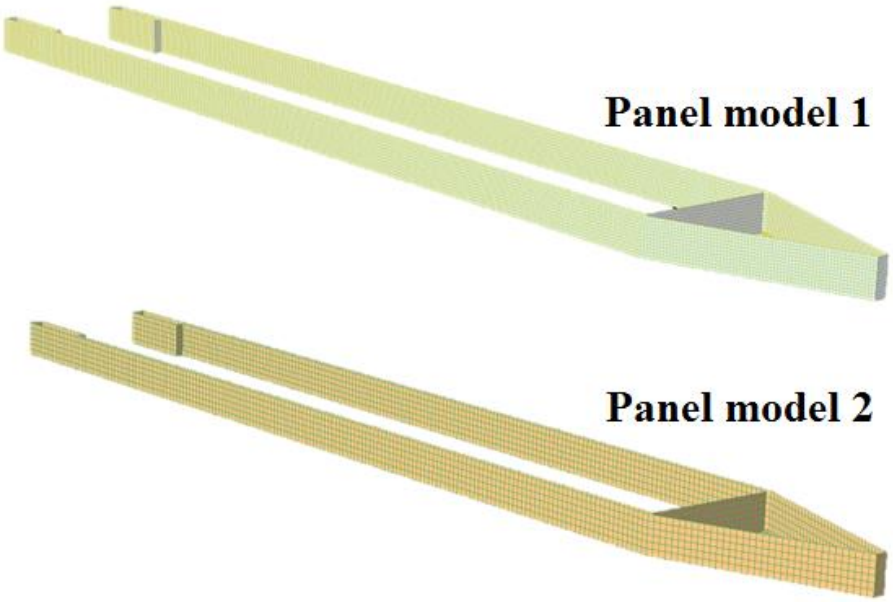

Figure 3.16: Panel model 1 (top) and Panel model 2 (bottom)

The simulation results obtained from panel model 2 and 3 must be similar to those obtained from panel model 1, in order to state convergence. Only if panel model 2 or 3 have convergence, can a different panel model be stated to have sufficient accuracy in its simulation results and panel model 1 be switched out for further studies. When deciding whether the panel models have convergence or not, one must consider the difference in peak values and the graphs similarity in total. For the three panel models facing the wave direction of 90 degrees, Figure 3.17 illustrates the heave, Figure 3.18 the roll, and Figure 3.19 the pitch. All graphs used for the convergence study can be found in the attachments. See Appendix A-2 for graphs with heave, pitch, and roll motions with wave direction of 0 degrees and 45 degrees.

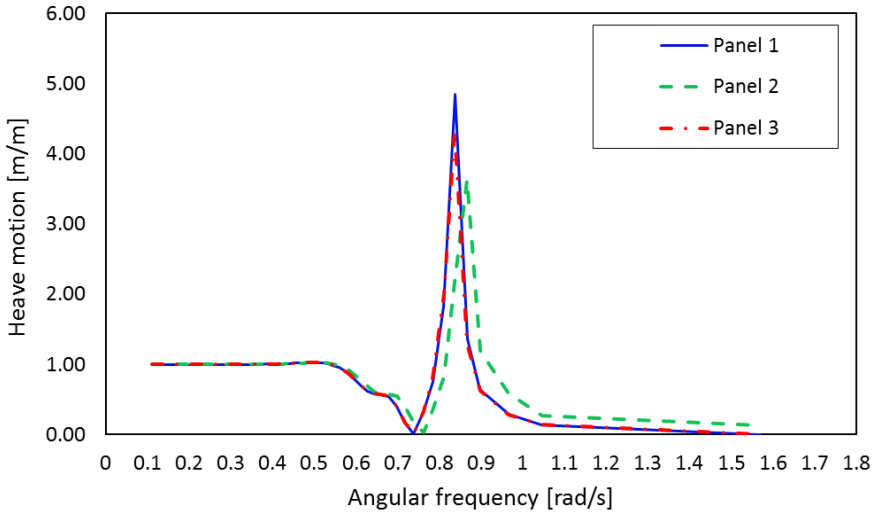

Figure 3.17: Panel model comparison, heave motion for wave direction 90

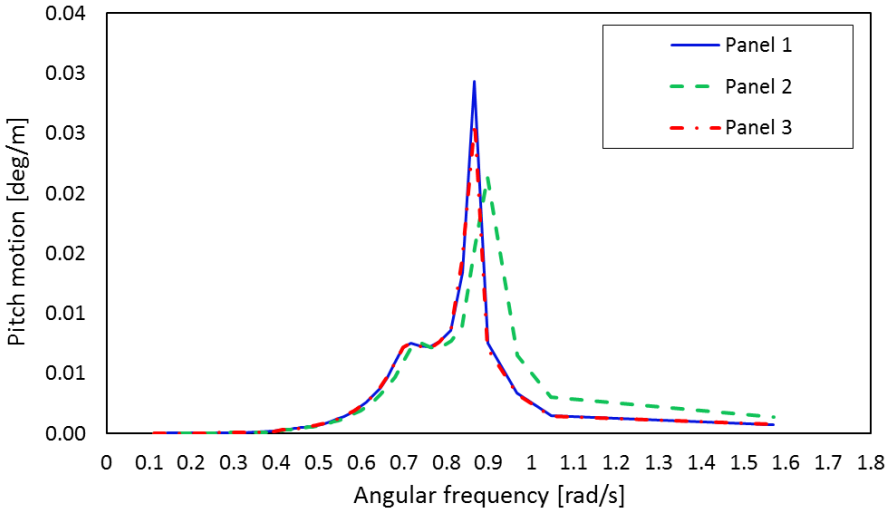

Figure 3.18: Panel model comparison, pitch motion for wave direction 90

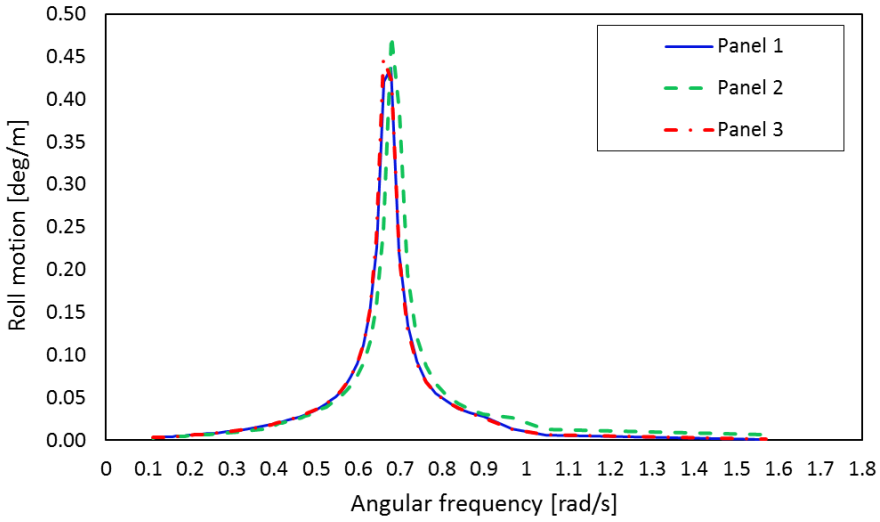

Figure 3.19: Panel model comparison, roll motion for wave direction 90

When comparing the graphs and maximum amplitudes of heave, roll, and pitch for the three panel models, it can be seen that results obtained with panel model 2 is not accurate enough for heave and pitch motions. It is apparent that the mesh used for panel model 2 is to coarse, and the results obtained are too inaccurate. Convergence between panel model 2 and panel model 1 can therefore not be claimed and panel model 2 can not be used for further studies.

Panel model 2 does however have a nearly sufficient accuracy for roll motions, but there are large differences in heave and pitch, and the graphs from panel model 2 and panel model 1 can not be said to have convergence for the wave directions considered. It is therefore apparent that Panel model 2 is too inaccurate and not suitable for further studies.

When comparing the results from panel model 1 and panel model 3, it is found that vessel motions are sufficiently similar for the different wave directions considered. The peak values vary by a small percentage and the graphs are otherwise very similar for heave, roll, and pitch in all the three wave directions. The simulation results are considered sufficiently accurate to state convergence of the two panel models, thus panel model 3 is used for further studies in this thesis. This will reduce the runtime of simulations by a significant amount, as the difference in runtime will greatly increase for the two panel models in further studies with more detailed and computationally heavy simulations. Table 3.4 below shows maximum values for heave, roll, and pitch for the three panel models in different wave directions.

Table 3.4: Maximum RAO amplitudes for different panel models

Hydrodynamic property	Panel model nr. (elements)	Maximum amplitudes Wave dir. 0	Maximum amplitudes Wave dir. 45	Maximum amplitudes Wave dir. 90
Heave	1 - (11484)	2.92	1.02	4.84
	2 - (2978)	2.15	1.02	3.63
	3 - (3911)	2.56	1.02	4.34
Roll	1 - (11484)	0.000	0.040	0.436
	2 - (2978)	0.000	0.037	0.474
	3 - (3911)	0.000	0.039	0.447
Pitch	1 - (11484)	0.018	0.009	0.029
	2 - (2978)	0.014	0.009	0.021
	3 - (3911)	0.016	0.009	0.026

3.2.3 Comparison of Panel Model and Composite Model

The effects of viscous drag and added mass on the vessel motions are seen when comparing the RAOs obtained with composite model to the RAOs obtained with only panel model. When compared to simulation results from panel model, the simulation results from composite model shows that all RAOs has reduced vessel motions in the peak area. All RAOs from composite model and panel model are otherwise nearly identical for sea states outside this peak area. This indicates that the viscous drag forces only influence the largest vessel motions, which is considered reasonable for the inertia dominated vessel studied in this thesis.

The viscous drag will increase damping for large vessel motions and this effect can be seen from the comparison of RAOs. Figure 3.20, Figure 3.21, and Figure 3.22 illustrates the comparison of heave, roll, and pitch RAO for composite model (viscous effects included) and panel model (viscous effects excluded), with a wave direction of 90 degrees with. See Appendix A-3 for comparison of remaining RAOs.

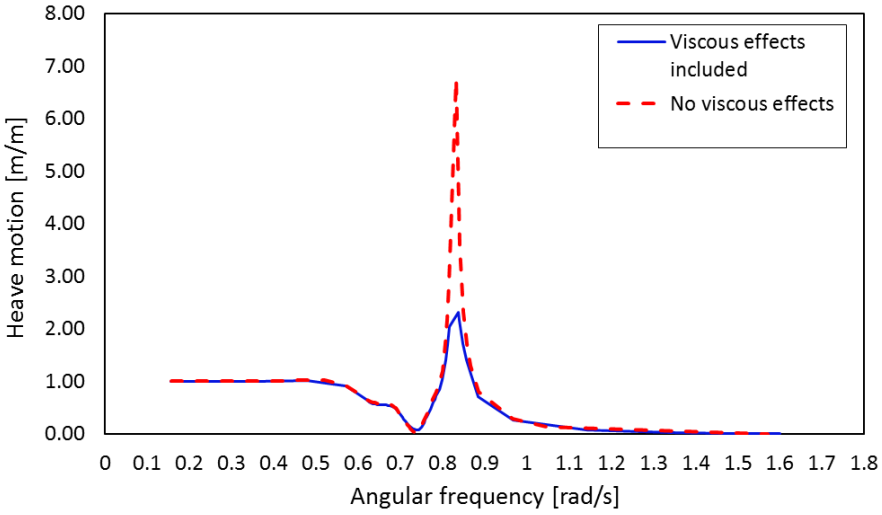

Figure 3.20: Heave, comparison of composite model and panel model

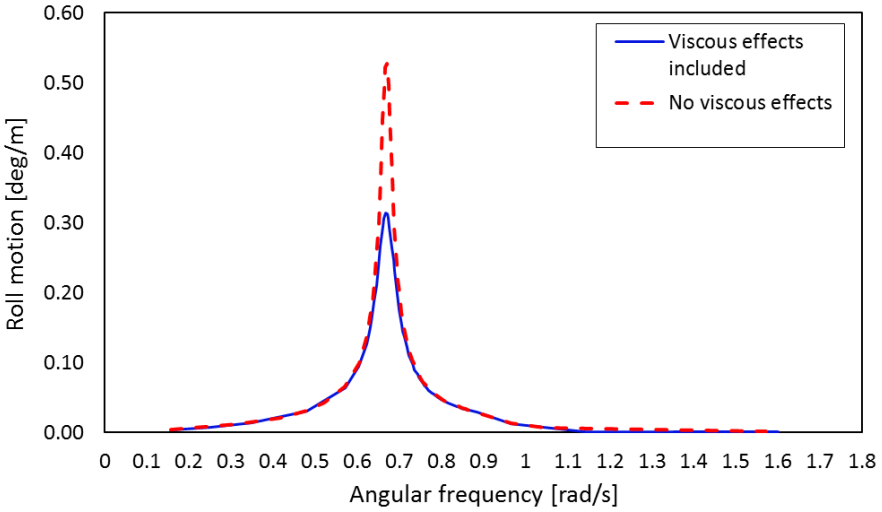

Figure 3.21: Roll, comparison of composite model and panel model

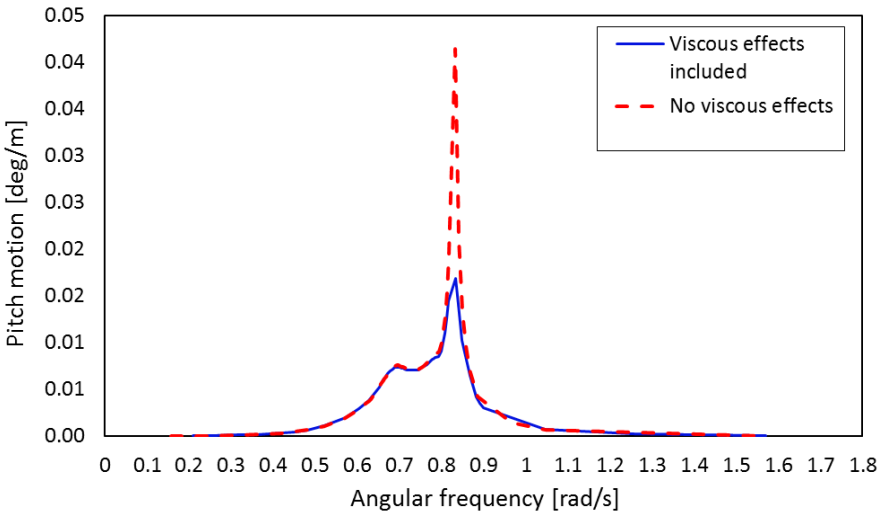

Figure 3.22: Pitch, comparison of composite model and panel model

4 Response Analysis – Coupled Vessel and Mooring System

Precise positioning and motion control of ships is important from a marine operational point of view. Mooring systems and dynamic positioning systems are important means of holding a structure against wind, waves, and current. The dynamic positioning system use thrusters to maintain a vessel stationary during marine operations. This system is expensive and the total costs will increase with the duration of operation. Since the vessel-shaped fish farm must remain in position for long periods of time, it will not be profitable to use a dynamic positioning system for station keeping. The vessel-shaped fish farm will therefore use mooring lines in conjunction with thrusters to remain in position and endure loads from wind, wave, and current forces. A mooring system consist of a number of cables which are attached to the floating structure, with the lower ends of the cables anchored to the seabed (Faltinsen, 1990).

In this chapter, static mooring line calculations are carried out to obtain mooring line parameters for input to time domain simulations. The numerical simulation program SIMO is used to conduct time domain simulations, and the coupled dynamics of the vessel and mooring lines are analysed. From the quasi-static time domain simulations, the capacity and functionality of applied mooring lines is studied.

4.1 Simulation program SIMO

SIMO is a computer program used for simulation of motions and station-keeping of complex systems of floating vessels. Some essential features of SIMO are flexible modelling of multibody systems and nonlinear time domain simulations with environmental forces due to wind, waves, and current (MARINTEK, 2015). In this thesis, SIMO is used for the quasi-static time domain simulations of the vessel and mooring lines. To incorporate the nonlinear effects for the rigid body model, the equations of motion must be solved in time domain. The frequency-dependence can then be included by a convolution integral, or by a state-space

representation of the time-dependent coefficients (Taghipour et al., 2008). For time domain analysis, SIMO uses the convolution integral approach in its formulation (MARINTEK, 2017).

Simulations obtained from SIMO are quasi-static and the mooring line forces are calculated in a quasi-static procedure, which does not consider the mooring line dynamics. Thus, the analyses conducted in SIMO are simplified and will result in smaller vessel motions and mooring line tensions than dynamic analyses which include mooring line dynamics. The time domain analyses in SIMO will however give an idea of the vessel and mooring lines coupled dynamics, and demonstrate the functionality of the mooring lines for different environmental conditions. The fish cages are not included in the SIMO simulations, but a fully dynamic analysis including the vessel, mooring lines, and fish cages was carried out in SIMO-Riflex. The simulation programs are built on software for dynamic analysis and are complete tools for simulation of marine operations from modelling to results (DNV GL, 2016).

SIMO consist of five modules communicating through a file system. The program modules are illustrated in Figure 4.1.

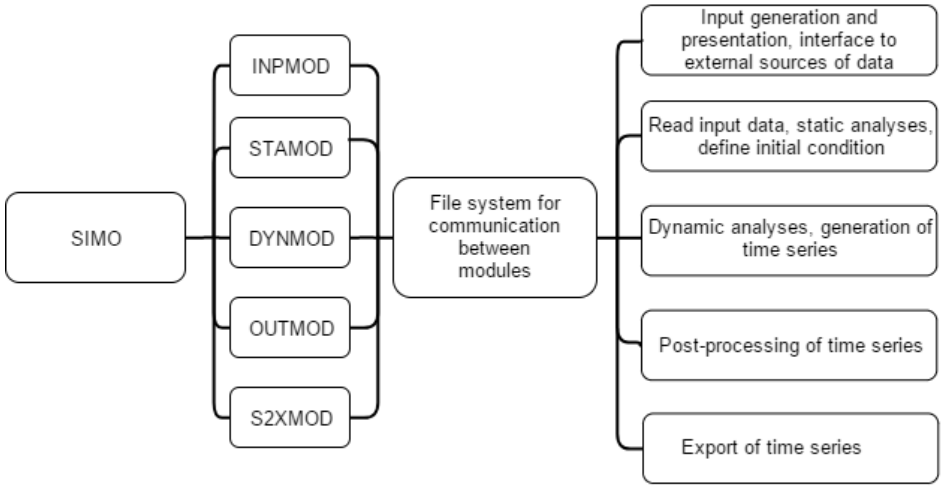

Figure 4.1: SIMO program modules (MARINTEK, 2015)

4.2 Static Calculation of Mooring Lines

To analyse the mooring system, calculations where performed and plots created using MATLAB as a numerical software tool. The static analysis is often carried out in the initial

stages of the catenary mooring system design phase. Load characteristics for a single line and the spread mooring system is established, ignoring the fluid forces on the lines (Chakrabarti, 2005). To perform these calculations, some characteristic values for the mooring lines had to be chosen. The assessment of different mooring line characteristics is not included in the initial static mooring line calculations, but is evaluated in the fully coupled time domain simulations in SIMO-Riflex. The characteristic values used in the mooring line calculations is found in Table 4.1. Figure 4.2 illustrates the mooring line configuration and their connection to the vessel turret.

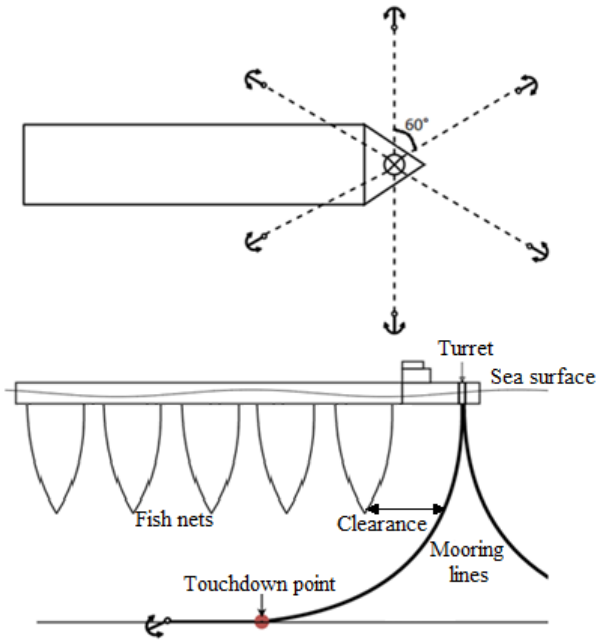

Figure 4.2: Simplified illustration of mooring line configuration

There should not be vertical forces acting on the anchor, since the forces can lift the anchor from the seabed and greatly reduce the mooring systems effect. A section of the mooring line is laid on the seabed, from the touchdown point to the anchor, and the mooring line weight works as a safety against vertical forces on the anchors. For the mooring line calculations in this chapter, it is assumed that the line is horizontal at the lower end, replicating the case with no uplift in the gravity anchor.

Table 4.1: Chosen characteristic values for mooring lines

Water depth [m]	**Submerged weight** [kg/m]	**Pretension** [kN]	**Preangle** [degrees]	**Fairlead to bow** [m]	**Touchdown to anchor** [m]
120	282.5	480	25.9	10	100

The equations used when calculating and plotting the mooring line geometry in MATLAB can be found in Chapter 2.4. The values found from MATLAB and used for mooring lines can be found in Table 4.2 below. The MATLAB code used for these calculations can be found in Appendix B.

Table 4.2: Calculated values for mooring lines

Fish net clearance to mooring line [m]	**Horizontal force at fairlead [kN]**	**Horizontal distance to touchdown point [m]**	**Length of catenary [m]**	**Total length of mooring lines [m]**
40.4	432	181	226	326

The fish net cages should not have physical contact with the mooring lines, since it will result in unwanted friction on the fish net and increased risk of the fish net getting tangled up in a mooring line. Such an event could result in expensive offshore operations, as well as huge costs due to escape of fish, production halt, and damaged equipment. There has not been conducted studies to determine whether the fish net cages should be square-shaped or cone-shaped in this thesis. The square shaped fish cages will result in shorter distance between the fish net and the mooring lines, and it is therefore assumed that the fish net cages are square-shaped for the calculation of clearance between the fish net cage and the nearest mooring line.

When affected by waves and currents, the fish net cages are assumed to drift further away from its initial position than the nearest mooring line. The clearance is therefore considered to be at minimum when the system is in its initial position and not affected by any environmental loads. The minimum clearance is found to be 40.4 meters, and the distance is considered sufficient to avoid contact between the fish net cage and the mooring lines. To obtain an increase in clearance, and further reduce the risk of contact between the mooring lines and fish cages, it was decided to use conical cages for the time domain simulations.

For a full static mooring analysis, algorithms are used to calculate the forces exerted on the vessel from all the catenary lines. The forces are summed up for all mooring lines to give the resultant horizontal restoring and vertical forces. The typical requirement for a full static mooring line analysis is the summation of several vessel offset positions; mean, near, far, and transverse (Rho et al., 2013). The method has disadvantages and conservative assumptions that requires large safety factors to account for uncertainties. The assumptions and complexity of these calculations makes the analysis of mooring lines suitable for implementation to computer software (Chakrabarti, 2005).

4.3 Numerical Modelling in SIMO

As previously mentioned, the time domain simulations in SIMO are quasi-static, and will therefore not include the dynamics of the mooring line system. The analyses will include the vessel motions due to hydrodynamic loads and the mooring lines effect on these motions for different positions of the vessel. The mooring lines must be checked for worst-case scenario, which is when the incoming waves are aligned with a single mooring line and the hydrodynamic loads are spread on as few mooring lines as possible. For the worst-case scenario, it is required that the most exposed mooring line can withstand a substantially larger tension than the other mooring lines. This circumstance is therefore used for time domain simulations and analysis of mooring lines.

For incoming waves that do not face the vessel head on, the vessel will rotate from its initial position and eventually align itself with the incoming waves. The wave direction used for simulations is therefore set to 180 degrees, so that the vessels initial position face the waves and one mooring line is aligned with the incoming waves. Simulations with an incoming wave direction of 150 degrees is also carried out, to illustrate the effect that different wave directions have on mooring line tension and the vessels ability to weathervane. The wave directions, initial position of the vessel, and mooring lines are illustrated in Figure 4.3.

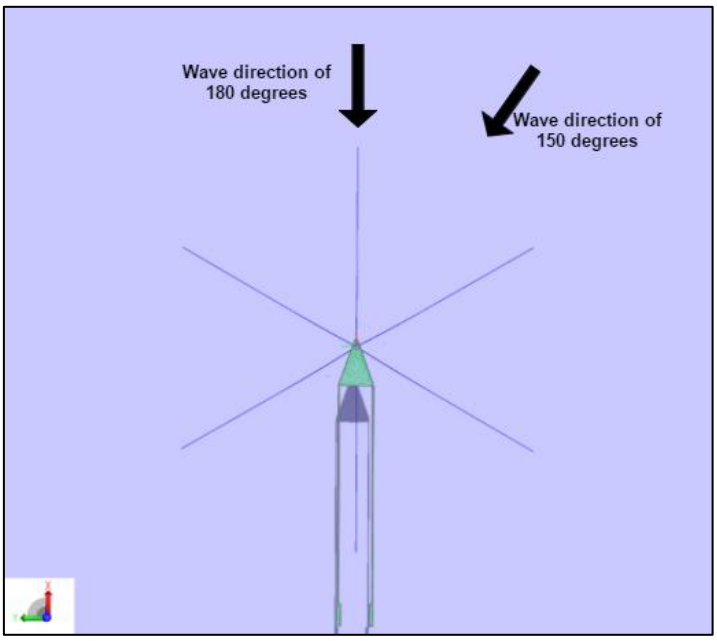

Figure 4.3: Wave directions for time domain simulations SIMO

Simulations with different significant wave heights and peak periods are carried out for both wave directions. The environmental conditions with chosen values can be found in Table 4.3. For the simulation setup in SIMO, input is imported from frequency domain analysis in Wadam and from mooring line calculations from MATLAB. The input parameters imported from Wadam is found in Table 4.4, and input used for mooring lines can be found in Table 4.5. For the dynamic simulation parameters in SIMO, the simulation length is set to 3 hours with a time step of 0.1 seconds.

Table 4.3: SIMA input for JONSWAP wind wave environment

EC	Hs [m]	Tp [s]	$\mathbf{Dir_w}$ [deg]
EC1	2	6	180
EC2	2	6	150
EC3	3	7	180
EC4	3	7	150
EC5	4	9	180
EC6	4	9	150
EC7	5	10	180
EC8	5	10	150

Table 4.4: SIMO input parameters imported from Wadam

Panel model	Geometry, structural mass, centre of gravity, and moment of inertia
Linear damping	Sum of damping for different vessel motions
Hydrostatic stiffness	Stiffness Matrix
Wave drift forces	Wave mean drift forces for different wave directions
Radiation data	Retardation function, added mass and damping

Table 4.5: SIMO input parameters for mooring line

Segmented Line type	**Unit**	**Value**
Length	[m]	338
Diameter	[m]	0.12
Modulus of elasticity	[N/m^2]	$5.07 \cdot 10^{10}$
Factor of elasticity	[-]	2 (standard for chain)
Unit weight in air	[N/m]	2825
Catenary Lines	**Unit**	**Value**
Pretension	[kN]	480
Direction	[degrees]	0, 60, 120, 180, 240, 300
Body Points	**Unit**	**Value**
Fairlead (X, Y, Z)	[m]	(0, 0, -10)

For all the time domain simulations conducted in this thesis, the reference point for the vessels translational- and rotational motions is located at the front of the vessel, above the turret. The simulation results from SIMO and SIMO-Riflex will illustrate the alteration of this reference points location in time. Figure 4.4 below illustrates the mooring line configuration, location of turret and the reference point for vessel motions in time domain analysis.

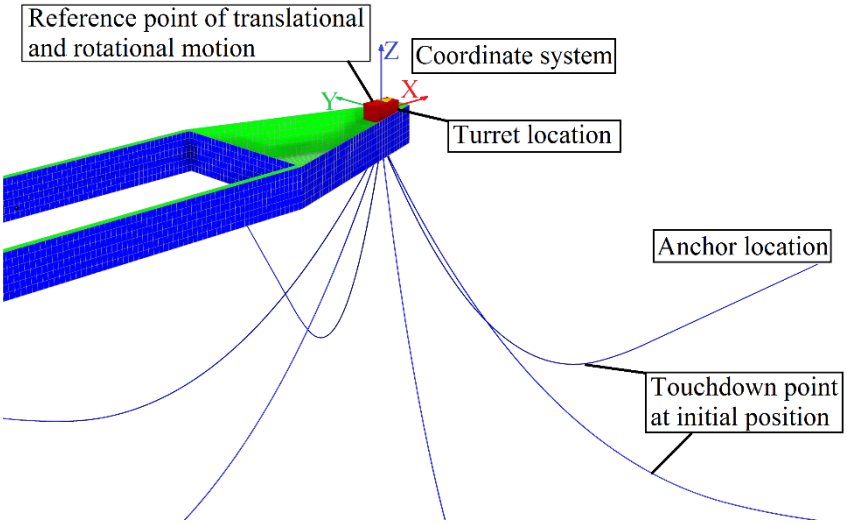

Figure 4.4: Location of reference point for vessel motions in time domain

4.4 Time Domain Simulation Results

For simulations with an incoming wave direction of 180 degrees and a significant wave height of 4 meter or higher, the mooring lines are not capable of withstanding the hydrodynamic loads on the vessel. The most exposed mooring line is lifted from the seabed and reaches a too high tension, which results in failure. As previously mentioned, the mooring line should not be lifted from the seabed, since this results in vertical forces in the anchor.

The mooring lines capacity is therefore insufficient and it is necessary to improve the configuration of the mooring lines. Different mooring lines will be analysed in SIMO-Riflex time domain simulations studies, where measures that could increases the mooring lines capacity were investigated. Figure 4.5 illustrates the simulation with EC7, where the mooring line is lifted from the seabed and reaches a tension beyond its capacity.

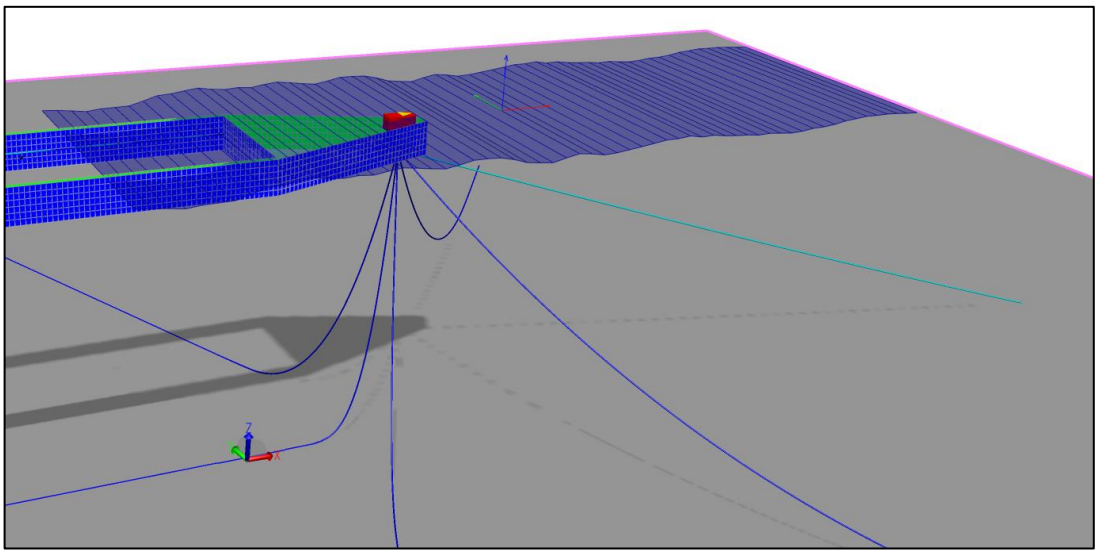

Figure 4.5: Mooring line lifted from the seabed for EC7

4.4.1 Vessel Motions

4.4.1.1 Translational Motion in X-direction

Figure 4.6 and Figure 4.7 below illustrates the vessels translational motion in x-direction, for EC1 and EC2, respectively. Additional simulation results of the vessels translational motions can be found Appendix C. When comparing the vessels translational motion for the two environmental conditions, the maximum translational motion is higher for the incoming wave direction of 150 degrees (maximum displacement of 17.1 meters), than 180 degrees (maximum displacement of 24.4 meters). This is due to the misalignment between the vessel and the incoming waves. Prior to the vessels alignment with the incoming waves, the waves will affect a much larger area of the vessel and generate larger vessel motions through an increase in hydrodynamic forces. After weathervaning, the vessel is aligned with the incoming waves and the translational motion will be significantly reduced from this point on.

For the cases with significant wave height of 2, 3, and 4 meters, the translational motion in x-direction is considered sufficiently small for marine operations. All translational motion in x-direction have a time period of approximately 200 seconds between each peak value, which is also considered satisfactory, as the position of the vessel is not rapidly altered.

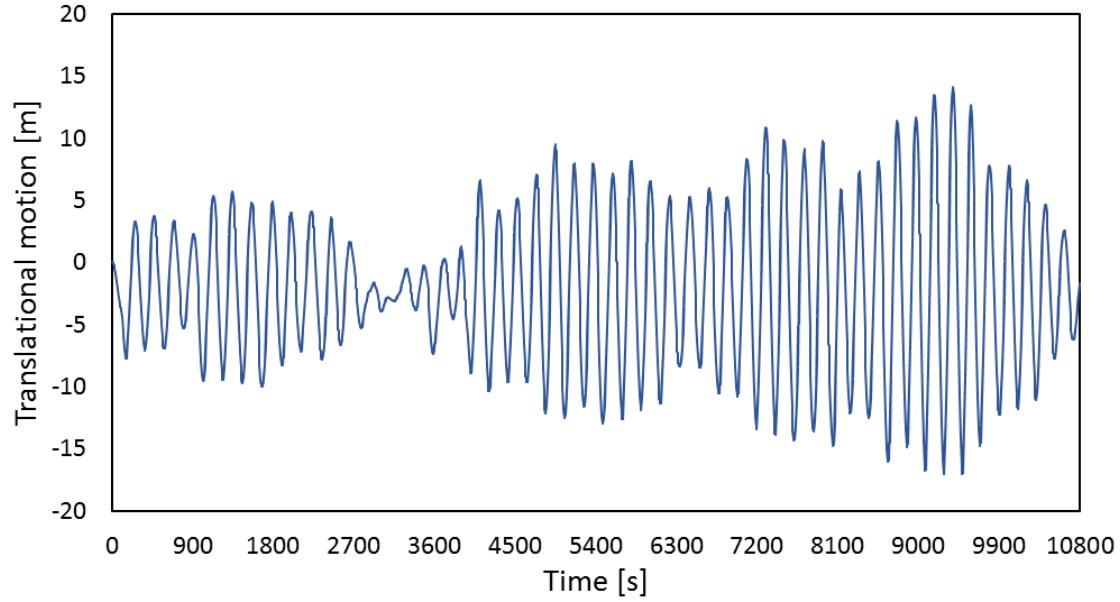

Figure 4.6: Translation motion in X-direction, EC1

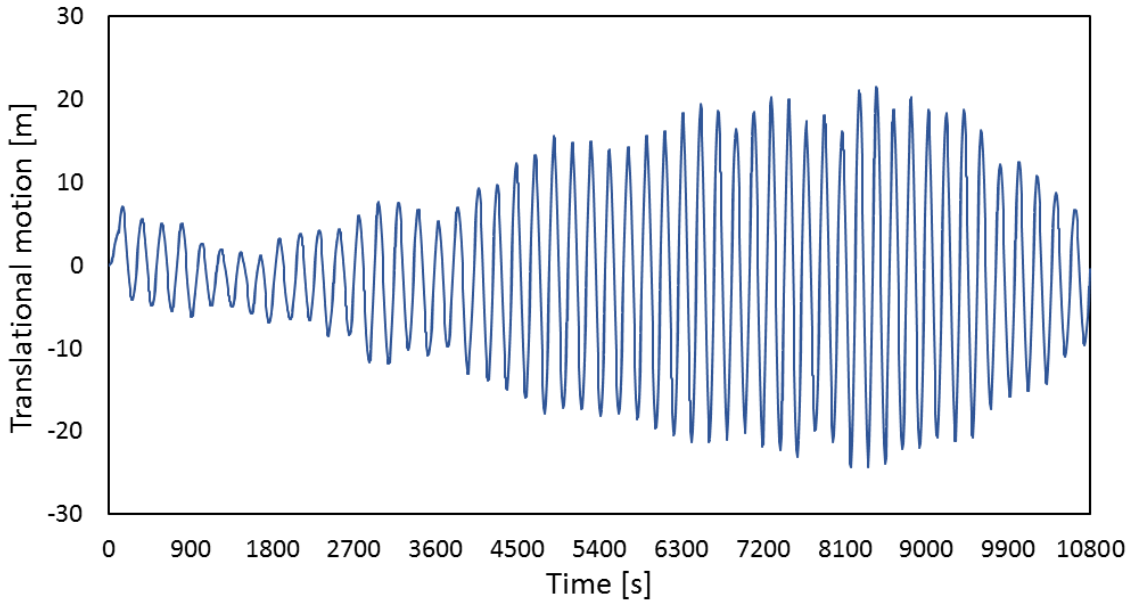

Figure 4.7: Translational motion in X-direction, EC2

4.4.1.2 Translational Motion in Y-direction

Figure 4.8 and Figure 4.9 below illustrate the vessels translational motion in y-direction, for EC1 and EC2. Additional simulation results of the vessels translational motions can be found Appendix C. When comparing the translational motion of the vessel for the two environmental

conditions, it can be seen that the vessel weathervanes in the early phase of simulations with EC2. This behaviour is a result of hydrodynamic forces on the vessel side, and vessel motions are therefore large in the early simulation phase. The vessel stabilizes after approximately 600 seconds of simulation and obtains a change in mean position of 1.2 meters.

Simulations with an incoming wave direction of 180 degrees have approximately no hydrodynamic forces acting in the y-direction, and thus nearly no motions or mooring line forces in y-direction. The vessels translational motions are therefore very low for simulations with EC1, EC3, EC5, and EC7. Vessel motions are however larger for simulations with an incoming wave direction of 150 degrees, due to the hydrodynamic forces and responding restoring forces acting in y-direction.

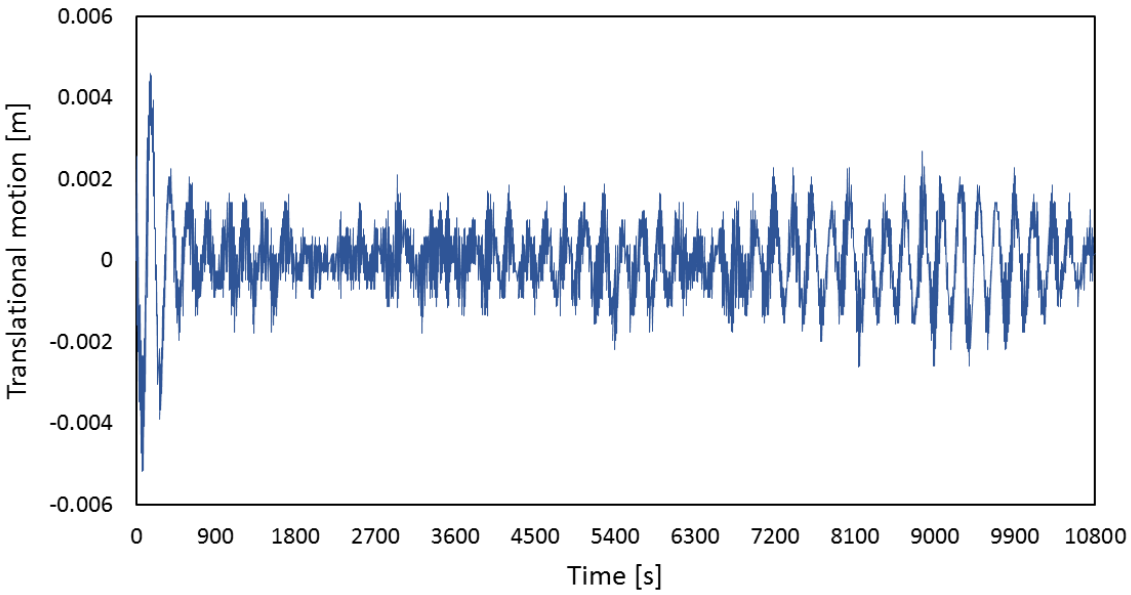

Figure 4.8: Translational motion in Y-direction, EC1

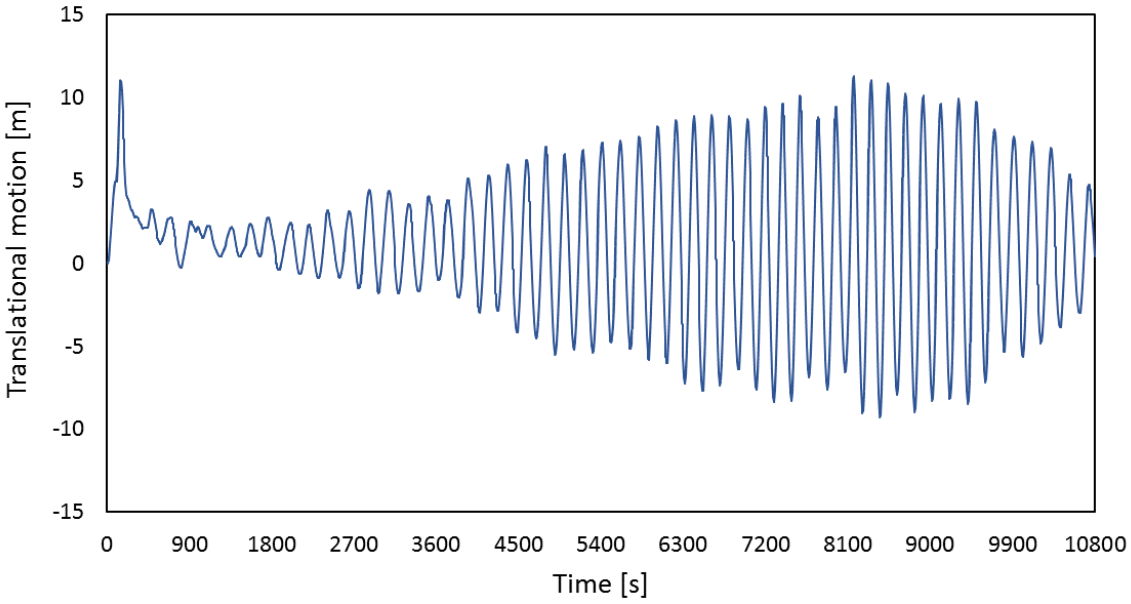

Figure 4.9: Translation motion in Y-direction, EC2

4.4.1.3 Rotational Motion About X-axis

Figure 4.10 and Figure 4.11 illustrate the vessels rotational motion about the x-axis, for simulations with EC1 and EC2 respectively. When comparing the rotational motion of the vessel for the two wave directions, it can be seen that the vessel has low roll motion amplitudes for simulations with EC1, as the vessel will face the waves and there are little hydrodynamic forces acting on the vessel sides. However, the vessel has large rotational motions in the early phase of simulations with EC2, and these rotational motions occur due to the incoming wave affecting the vessels starboard side. The vessel will then weathervane so that the bow faces the waves after approximately 600 seconds, and the roll motions will eventually subside. The rotational motions are reduced when the vessel has weathervaned and the rotational amplitudes are then similar to the results obtained with incoming wave direction of 180 degrees.

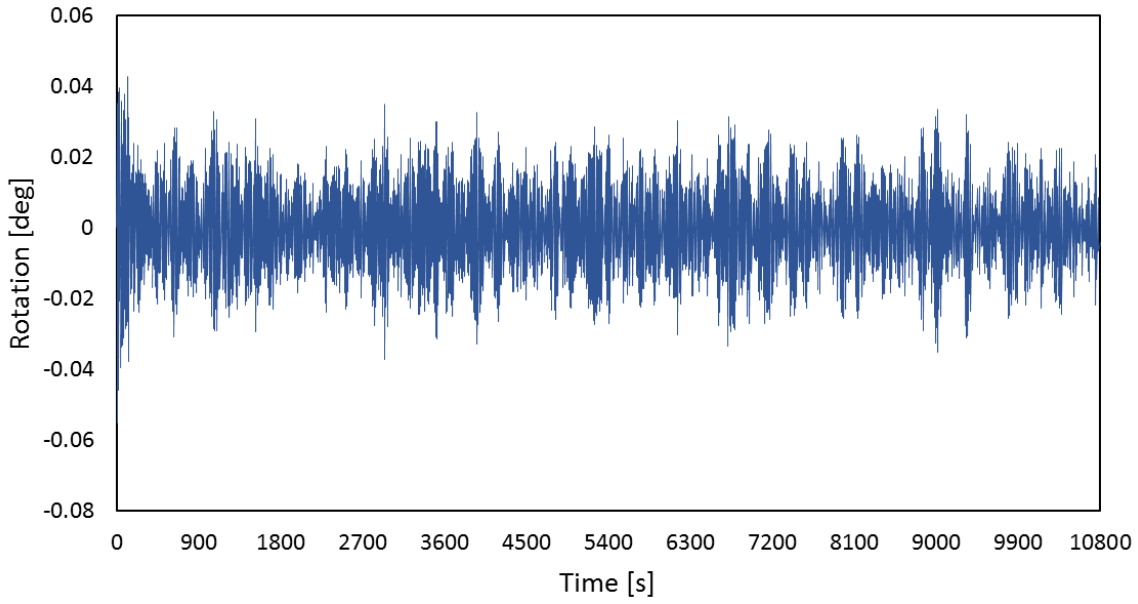

Figure 4.10: Rotational motion about X-axis, EC1

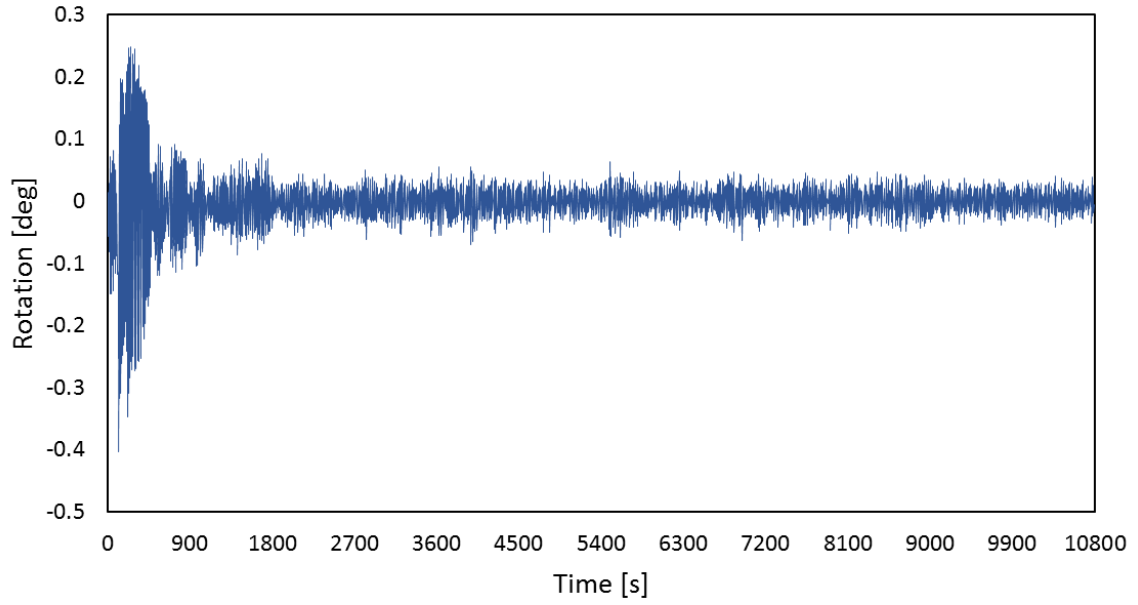

Figure 4.11: Rotational motion about X-axis, EC2

5 Response Analysis – Coupled Vessel, Fish Nets, and Mooring Lines

When the vessel-shaped fish farm is moored to the seabed, it becomes a coupled dynamic system with complex loadings. For the case studied in this thesis, the coupling between the vessel, fish nets, and slender mooring lines is of great importance. Time domain simulations are therefore carried out to analyse the vessel motions with attached mooring lines and fish nets. The time domain simulations are carried out using the SINTEF Ocean software SIMO and SIMO-Riflex, in the SIMA suite of programs. The equation of motion is integrated in these time domain simulations, where damping, added mass, and influences from coupling are included.

5.1 Simulation Program SIMO-Riflex

The tremendous growth of the aquaculture industry necessitates and motivates the use of offshore locations for future fish farming (Lader et al., 2007). This will require new technologies, such as structures that are compliant with the high energy of the open ocean. Development and design of these structures will depend upon numerical tools that can simulate and predict the structural response in specific offshore sea states. Numerical models are important design tools, which can predict the response of aquaculture structures in specific sea load conditions, how they move and deform, structural stresses, and global wave and current loads (Lader et al., 2007). It is therefore an increasing interest from the aquaculture industry to use advanced numerical data tools in the development of technical fish farm solutions. There is also a new trend of engineering companies and ship consultants increasingly offering their services to aquaculture. This developing trend must be considered positive with regards to the advance in competence used in the development of new aquaculture concepts.

The numerical simulation program SIMO-Riflex is used to generate the fully coupled dynamic analysis of the vessel-shaped offshore fish farm with installed fish nets and mooring lines. The coupled program compute both static and dynamic simulations of the structure, and is based on

a nonlinear finite element formulation (Keshavarz, 2011). Riflex is a finite element solver with a wide range of applications. The program was first developed as a tool for analysis of flexible marine riser systems, but has also been used for other types of slender structures, such as umbilicals, mooring lines, pipelines, and conventional risers (Keshavarz, 2011). In the early 1990s, numerical models for floating collars and fish nets were implemented to Riflex, but the models have not been in much use since then.

Now that there is strong interest in the aquaculture industry for software simulation tools, the numerical models are more frequently used and modified (Aksnes, 2016). Riflex has high potential for analysis of aquaculture systems, due to the hydrodynamic models for slim bodies, which characterize highly nonlinear aquaculture constructions. Nonlinearity is of crucial importance for analysis of aquaculture constructions, and Riflex is expected to develop into the state-of-art program for analysis of such of constructions.

Riflex does however include some limitations, with a complicated user interface that requires a high level of user competence. The aquaculture models are also very complex, and the simulations are numerically demanding, especially for large systems such as the vessel-shaped offshore fish farm studied in this thesis. Setting up the numerical models for fish nets in Riflex is a time consuming process, and a modelling tool for easier input of aquaculture constructions is therefore under development (Aksnes, 2016).

Riflex is exclusively used for modelling and simulation of the slender flexible structures, while SIMO is used for modelling and simulation of the vessel (and simplified mooring system). The coupled numerical program SIMO-Riflex can fulfil both of these tasks, and carry out the time domain simulations for the whole fish farm system with coupling of the slender flexible bar elements and vessel. The components modelled by SIMO and Riflex for the coupled SIMO-Riflex simulations are illustrated in Figure 5.1.

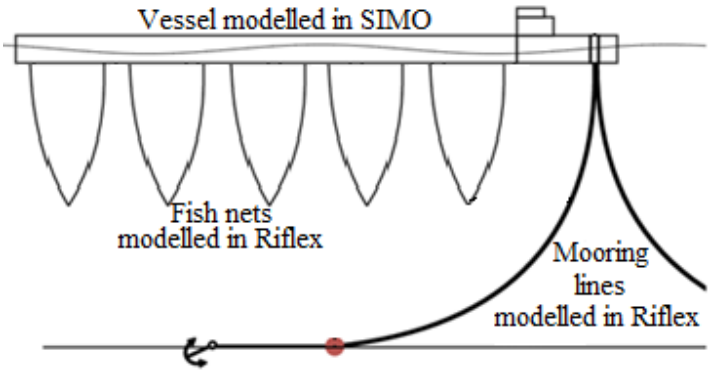

Figure 5.1: Components modelled in SIMO and Riflex for SIMO-Riflex simulations

SIMO-Riflex is built up of five subprograms or modules, that communicate through a file system as illustrated in Figure 5.2.

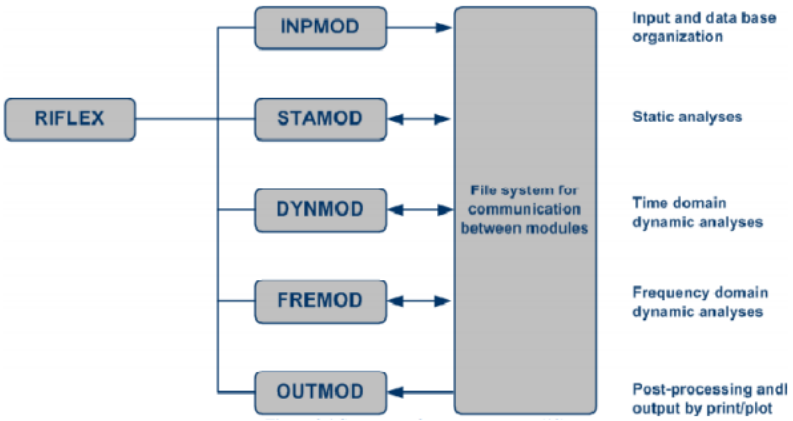

Figure 5.2: Structure of Riflex system (MARINTEK, 2016a)

The INPMOD module reads most of the input data i.e. material properties and environmental parameters, and a data base is organized for use in subsequent analyses. Several analyses can then be carried out by the other modules, without having to rerun INPMOD. The STAMOD module is used to exert several types of static analyses. The static results are used directly in parameter studies and define the initial data for a dynamic analysis. Based on the input given in INPMOD, STAMOD will generate element mesh, stress-free configuration, and key data for finite element analysis (MARINTEK, 2016a).

The DYNMOD module is used to perform time domain dynamic analyses, and is based on the environment data and static data obtained from STAMOD. Several dynamic analyses can be carried out without rerun of INPMOD and STAMOD. The response time series are stored on

file for postprocessing in OUTMOD. The OUTMOD module performs postprocessing of results from STAMOD and DYNMOD, and time series can be exported in standardized file formats for further postprocessing (MARINTEK, 2016a).

5.2 Numerical Modelling in SIMO-Riflex

The model is exported from SIMO to SIMO-Riflex, containing the values previously imported from Wadam, found in Table 4.4. The mooring lines capacity was found to be insufficient for simulations with a significant wave height of 4 meters or higher. Based on the mooring lines performance in SIMO, new mooring line parameters are established for the fully coupled time domain simulations in SIMO-Riflex. Furthermore, fish nets and new environments are modelled for the time domain analyses conducted in this chapter.

5.2.1 Modelling of Mooring Lines

The mooring lines used in SIMO simulations were unsatisfactory, and a short assessment of different mooring lines was therefore conducted from SIMO-Riflex time domain results. The mooring lines capacity was improved by utilizing a different type of chains, with increased weight and length. Three different studless chains of grade K4 were briefly analysed, and their parameters were found from tabulated mooring component data, given by Chakrabarti (2005). The chain properties are presented in Table 5.1 below.

Table 5.1: Chain mooring parameters

Parameters	**Chain 1**	**Chain 2**	**Chain 3**
Weight in water [kg/m]	419	492	530
Breaking strength [kN]	20266	23023	24420

The capacity of the three chain mooring lines were compared using simulation results from EC11. As previously mentioned, the vessel should detach from the turret and move inshore for more extreme weather conditions. Designing mooring lines for more severe weather would result in over dimensioning and unnecessary costs.

Sections of chain lifted from the seabed were compared for the three chain types, and the capacity was deemed sufficient for chain 2 and chain 3. A too large section of the mooring line was lifted from the seabed for chain 1, and it was therefore considered inadequate. The chain selected for further studies was chain 2, since the excess weight from chain 3 will result in unnecessary fairlead tension.

The standards indicate the drag coefficient for new chain mooring lines to be set as 2.4, but the drag coefficient is set to 2.6 to account for marine growth for the studless chain (Chakrabarti, 2005). Mooring lines are modelled as slender bar elements in SIMO-Riflex, and the parameters used for modelling can be found in Table 5.2. The mooring lines in SIMO-Riflex and their numbering are illustrated in Figure 5.3.

Table 5.2: SIMO-Riflex input parameters for mooring lines

Generic axisymmetric cross section	**Unit**	**Value**
Mass coefficient	[kg/m]	492
External area	[m^2]	0.15
Cross-section type	[-]	Bar
Quadratic drag coefficients	[-]	$CQ_x = 0.1$ and $CQ_y = 2.6$
Added mass coefficients	[-]	$CA_x = 0.0$ and $CA_y = 1.0$
Axial force corresponding to relative elongation	[N]	$4.67 \cdot 10^8$
Line type	**Unit**	**Value**
Length	[m]	450
Number of elements	[-]	80
Element length	[m]	5.625
Supernode - constraint	**Unit**	**Value**
Anchor 1 - fixed (x,y,z)	[m]	(400, 0, -120)
Anchor 2 - fixed (x,y,z)	[m]	(200, 346, -120)
Anchor 3 - fixed (x,y,z)	[m]	(-200, 346, -120)
Anchor 4 - fixed (x,y,z)	[m]	(-400, 0, -120)
Anchor 5 - fixed (x,y,z)	[m]	(-200, -346, -120)
Anchor 6 - fixed (x,y,z)	[m]	(225, -346, -120)
Fairlead - slaved (x,y,z)	[m]	(0, 0, -12)

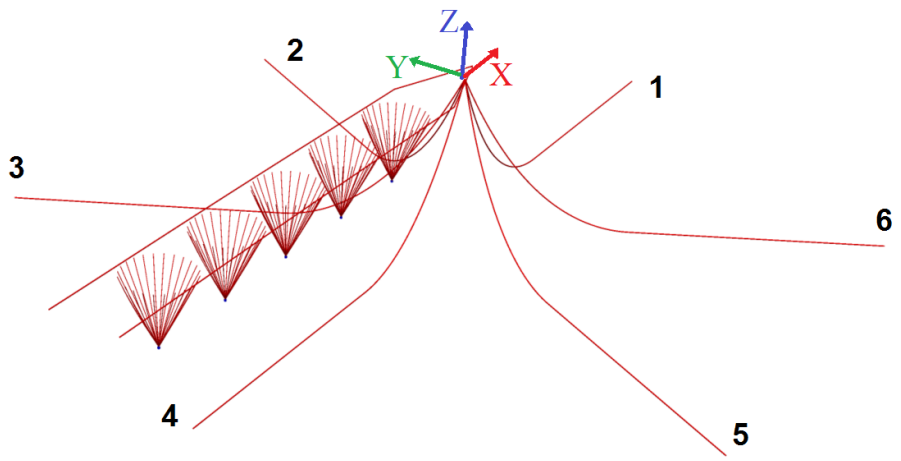

Figure 5.3: SIMO-Riflex mooring lines with numbering

5.2.2 Modelling of Flexible Fish Nets

There are in principle two approaches to model the most important part of most aquacultural structures, namely the behaviour of a net and the forces acting on it. One of these approaches is to model the net as individual knots and twines, and calculating the total drag forces on the net as the sum of drag on the individual elements (Lader et al., 2007). This detailed approach will lead to high accuracy in simulations and results, but is deemed a very time-consuming approach for the large fish farm studied in this thesis.

The second approach is the one used in this thesis, where the net is modelled by dividing it into super elements, which contain properties that simulate the nettings knot and twine structure. The hydrodynamic drag and lift components on the net element is calculated by means of coefficients that are dependent on the nets solidity ratio (Løland, 1991). A FEM approach is then utilized to calculate the response on the structure. Calculating the hydrodynamic forces from drag and lift coefficients has shown to be an efficient method, that provides practical and accurate results, although it does not consider all details of the flow or net structure (Lader et al., 2007).

The fish nets are modelled using slender lines with fish net cross section, and each conical fish cage is built up of 24 slender lines. These slender lines are connected to supernodes, one end at the vessel and the other at the bottom weight. Figure 5.4 below illustrates the slender lines and screens that make up the fish nets, and the supernodes they are connected to.

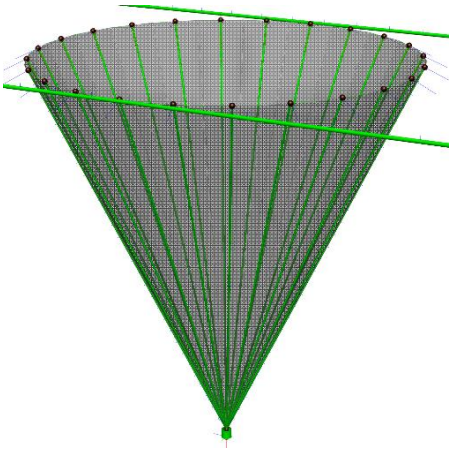

Figure 5.4: Fish net with supernodes and slender lines

In order to acquire the inputs for fish nets in SIMO-Riflex, the program MATLAB was used to carry out calculations. MATLAB script used for these calculations can be found in Appendix D. The total number of twines for every slender element is calculated from Equation 5.1, and the total number of vertical twines from Equation 5.2.

$$n = \frac{L_{avg}}{d} * S_n \tag{5.1}$$

$$n_{vertical} = \frac{L_{avg}}{\lambda} \tag{5.2}$$

$$\lambda = \frac{2d + \sqrt{(2d)^2 - 4S_n d^2}}{2S_n} \tag{5.3}$$

Where n is the total number of twines, L_{avg} is the average width of one net beam, d is the twine diameter, S_n is the Solidity ratio, $n_{vertical}$ is the number of vertical twines, and λ is the width of each opening in the net, i.e. the distance between each vertical twine.

The axial stiffness of the net is calculated from the material properties and geometry, using Equation 5.4. Net average external area and mass is calculated using Equation 5.6 and Equation 5.7, respectively.

$$k = E * A_{twine} * n_{vertical} \tag{5.4}$$

$$A_{twine} = \frac{\pi}{4} * d^2 \tag{5.5}$$

$$A_{net} = A_{twine} * n \tag{5.6}$$

$$m_{net} = A_{net} * \rho \tag{5.7}$$

Where k is the axial stiffness, E is the modulus of elasticity, A_{twine} is the area of one twine, A_{net} is the area of one net section, and m_{net} is the mass of the net. The constants used for the calculation of fish cage is found in Table 5.3, and are found from Li et al. (2013) and from fish net properties by Aqualine (2016).

The current velocity reduction factor is calculated from the simple expression for the velocity reduction behind a panel $u = rU$ given by Løland (1991), where u is the velocity in the wake behind the panel and $r = 1 - 0.46CD$. For simplification purposes, each fish net is given one velocity reduction factor. The velocity reduction factors presented in Table 5.4 are found from calculations in MATLAB, and can be found in Appendix D. For the multidirectional sea condition considered in Chapter 5.3.2, the velocity reduction factors are assumed based on the area affected by waves and current loads.

Table 5.3: Constants used for fish cage calculations

Parameter	**Unit**	**Value**
Solidity ratio, S_n	[-]	0.30, 0.15
Twine diameter, d	[m]	0.003
Density of net, ρ	[kg/m]	1710
Young's modulus, E	[MPa]	350

Table 5.4: Riflex input parameters for flexible fish nets

Fish net cross section	**Unit**	**Value**
Mass	[kg/m]	1.6814
External area	[m^2]	0.00098328
Cross-section type	[-]	Bar
Solidity ratio	[-]	0.30
Net width top	[m]	5.56
Net width bottom	[m]	0.0
Added mass, tangential direction	[kg/m]	$Amx = 0.01$
Added mass, normal direction	[kg/m]	$Amy = 1.08$
Axial force corresponding to relative elongation	[N]	$1.79 \cdot 10^5$
Current velocity reduction factor for fish net 1, 2, 3, 4, and 5	[-]	0.954, 0.862, 0.769, 0.677, 0.585
Current velocity reduction factor for fish net 1, 2, 3, 4, and 5 (Multidirectional simulation)	[-]	0.954, 0.90, 0.90, 0.90, 0.90
Bottom weight cross section	**Unit**	**Value**
Mass	[kg/m]	8000
External area	[m^2]	2.0
Cross-section type	[-]	Bar
Axial stiffness, constant	[N]	$1.0 \cdot 10^8$

5.2.3 Modelling of Rigid Fish Nets

A model with simplified rigid nets is included in this thesis, and its functionality is investigated through a short sensitivity study. In reality, the nets used for fish farming are flexible structures that experience different degrees of deformation depending on the wave and current conditions. There are strong nonlinearities in the hydrodynamic forces on the nets, and nonlinear models are therefore usually required to model the nets. Deformation is neglected when using rigid nets, and the simplification is therefore expected to overestimate the hydrodynamic forces and viscous effects from the nets. The nets are however expected to have less influence on the large support vessels motions than for a traditional flexible collar fish cage (Li et al., 2017).

Moreover, the nets are more than 10 meters below the free surface and the wave forces on the nets are significantly reduced.

The simplified rigid model can be used to study the influences of the nets on the global responses of the system. Furthermore, time domain simulations with rigid nets are less computationally heavy than simulations with flexible nets, and could potentially save the researcher a tremendous amount of time. For the rigid model in this thesis, each conical cage was simplified as 24 vertical Morison beams, and equivalent added mass coefficients and diameters were computed based on the chosen solidity ratio. The equivalent drag coefficients for these circular Morison beams were obtained according to Aksnes (2016) and calculated from Equation 2.23.

$$\theta = 90 - tan^{-1}\left(\frac{D_{avg}}{h}\right) \tag{5.8}$$

$$C_{d_{Rigid}} = C_{d_{twine}} \cdot n \tag{5.9}$$

Where θ is the angle of the fish net relative to the flow direction, D_{avg} is the average diameter of the fish net, and h is the height of the fish net. Further is $C_{d_{Rigid}}$ the equivalent drag coefficient for the rigid net and $C_{d_{twine}}$ is the drag coefficient for one twine, which is calculated from Equation 2.23 by the input of solidity ratio S_n.

In order to investigate the potential overestimation of hydrodynamic forces and viscous effects from the rigid nets on the system, a sensitivity study was carried out. In the sensitivity study, the maximum mooring line tension was compared for simulations with rigid and flexible fish cage models. For the modelling of rigid nets, an equivalent drag coefficient was calculated based on a solidity ratio of 0.15. Thus, the flexible nets were modelled with a solidity ratio of 0.15 for the comparison of rigid and flexible nets in Chapter 5.3.1. The parameters used for modelling of rigid nets were found from calculations using the equations in Chapter 2.3. The MATLAB script with calculations can be found in Appendix D. The rigid nets are modelled from slender beam elements with drag and lift coefficients found from solidity ratio. Parameters

used for modelling can be found in Table 5.5 below, and Figure 5.5 illustrates the slender beam elements that make up the rigid nets.

Table 5.5: Riflex input parameters for rigid fish nets

Generix axisymmetric cross section	**Unit**	**Value**
Mass	[kg/m]	1.6814
External area	[m^2]	0.07854
Cross-section type	[-]	Beam
Quadratic drag coefficient in tangential direction	[-]	0.05
Quadratic drag coefficient in normal direction	[-]	1.946
Added mass per unit length in normal direction	[-]	1.0
Axial stiffness - Constant	[N]	$1.0 \cdot 10^9$
Bending stiffness – Constant	[Nm^2]	$1.0 \cdot 10^8$
Torsion stiffness – Constant	[Nm^2/rad]	$1.0 \cdot 10^8$

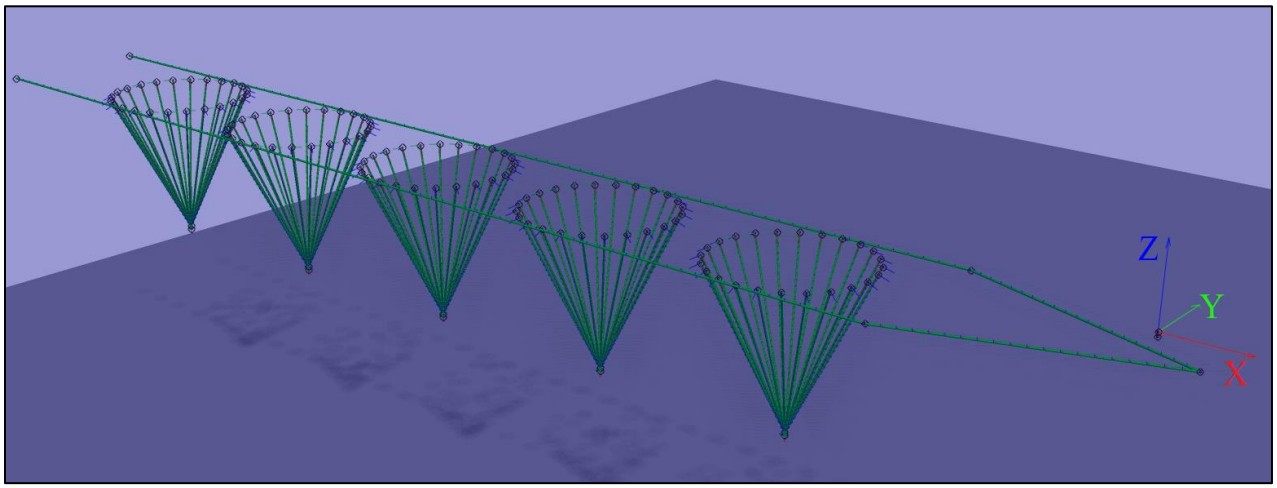

Figure 5.5: Rigid nets and supernodes

5.2.4 Modelling of Waves and Currents

For the time being, SIMO-Riflex can not run irregular wave conditions for systems containing fish net models. For this reason, the environmental conditions used for time domain simulations in this thesis only run regular waves. The amplitudes chosen for time domain simulation can be found in Table 5.6. As previously mentioned, the fully dynamic simulations for the vessel-shaped fish farm system is complex in modelling and computationally demanding to run. For simulations with misaligned sea and weathervaning of the system, the complexity increases further. Therefore, only one environmental condition with misaligned waves and current is carried out in the present work.

From observations from the North Sea, it is concluded that a misalignment between waves and current of up to 30 degrees is common, while misalignment larger than 60 degrees occurs less than 5% of the time (Bachynski, 2014). A sea state with misaligned wave and current condition of 30 degrees was therefore carried out in this thesis. Wave and current directions which resulted in the vessels alignment with one mooring line was found and implemented in EC12. The vessel position in EC12 after weathervaning is illustrated in Figure 5.6 below.

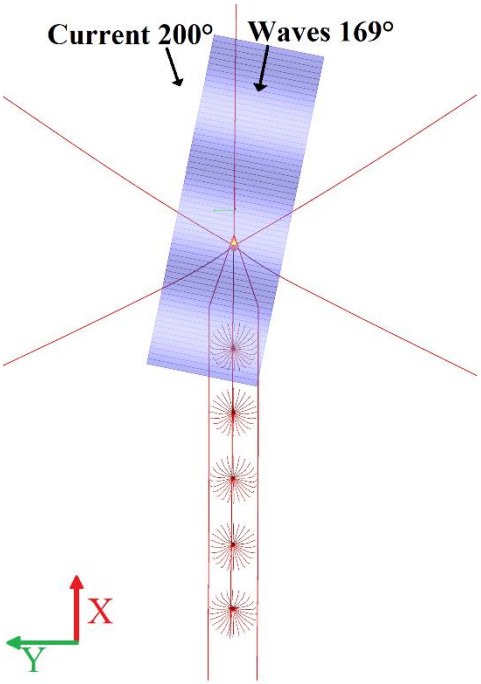

Figure 5.6: Vessel position in EC12

For more harsh environments than those studied here, it is expected and recommended that the vessel-shaped fish farm will disconnect from the mooring turret, and move inshore to wait for weather. The nets will otherwise have too large deformations, with a decrease in fish welfare and increased risk of fish mortality. Such harsh environments will also result in high fish net tensions, with risk of snap loads due to large vessel motions. The environmental conditions are therefore limited to a regular wave height of 4 meters. The current velocity is limited to 1.0 m/s in compliance with the conclusion made by Huang et al. (2008), who concluded that farming sites should not be situated in areas with current velocities exceeding 1.0 m/s, unless technological devices to overcome volume deformation has been implemented.

As previously mentioned, the current is assumed unidirectional, with uniformly distributed and constant velocity over varying water depth. This assumption is made for simplification purposes, and will result in higher mean current velocities, and thus reduce the risk of underestimation of the hydrodynamic forces on the nets and mooring lines. The current velocity is therefore modelled as constant down to a water depth of 100 meter in the present work.

Table 5.6: Environmental conditions for SIMO-Riflex

EC	Amp [m]	Tp [s]	V_c [m/s]	$\mathbf{Dir_w}$ [deg]	$\mathbf{Dir_C}$ [-]
9	2.0	6.0	0.20	180	180
10	3.0	8.0	0.30	180	180
11	4.0	10.0	0.40	180	180
12	3.0	8.0	0.30	169	200

5.3 Time Domain Simulation Results

5.3.1 Comparison of Rigid and Flexible Fish Net Models

A sensitivity study was carried out by comparing the mooring line tension from a rigid model, a flexible model without reduction factor, and a flexible model with reduction factor. Drag forces on the fish net is mostly affected by current forces, and simulations with only current is therefore used in this sensitivity study. The rigid model is less computationally demanding than

the flexible models, but is expected to overestimate the hydrodynamic forces and viscous effects from the nets, due to neglecting deformation. If the rigid model overestimates the hydrodynamic forces and viscous effects, this can be seen from the mooring line tension. Only if the rigid model has satisfactory results in the sensitivity study can it be used for further analyses. By comparing the drag forces between the two flexible models, the importance of including the velocity reduction factor is illustrated.

Simulations with current velocities varying from 0.1 m/s to 1.0 m/s, with an increment of 0.1 m/s, were used to investigate the difference in maximum mooring line tension for the three models. The results from the most exposed mooring line is shown in Figure 5.7, and results from all mooring lines for three different current velocities are shown in Figure 5.8, Figure 5.9, and Figure 5.10 below. The mooring line numbering is illustrated in Figure 5.3.

From the graphs, it is evident that the rigid model overestimates the hydrodynamic forces and viscous effects, especially for strong currents, and can therefore not be used for further studies in time domain. The graphs also illustrate the importance of velocity reduction factor as the velocity reduction factor reduces the flow velocity through the nets, and thus the drag forces. Therefore, the flexible model with no reduction factor also overestimates the drag force, and velocity reduction factors must be included in further studies. Compared to the rigid model however, the drag forces increase more proportionally to the flexible fish nets with increasing current velocities. Table 5.7 shows the maximum mooring tension in the most exposed mooring line for three current velocities and the difference between the three models.

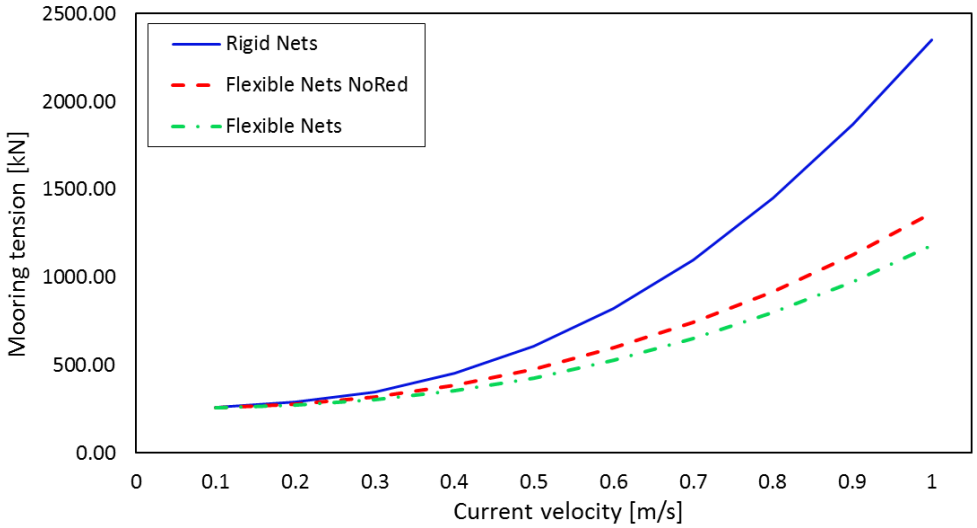

Figure 5.7: Tension in mooring line 1 for different current velocities and fish net models

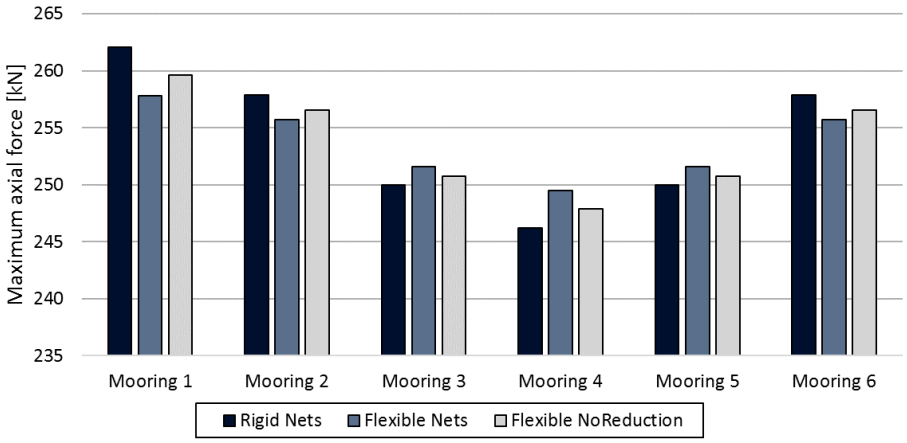

Figure 5.8: Mooring line tensions in 0.1 m/s current

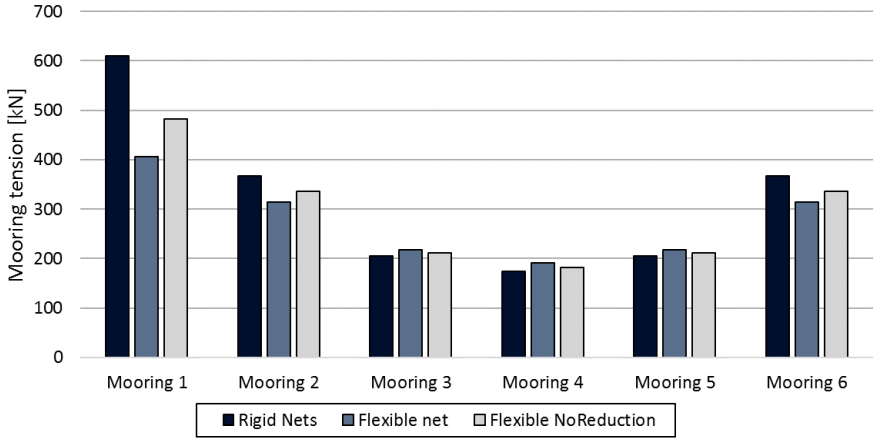

Figure 5.9: Mooring line tensions in 0.5 m/s current

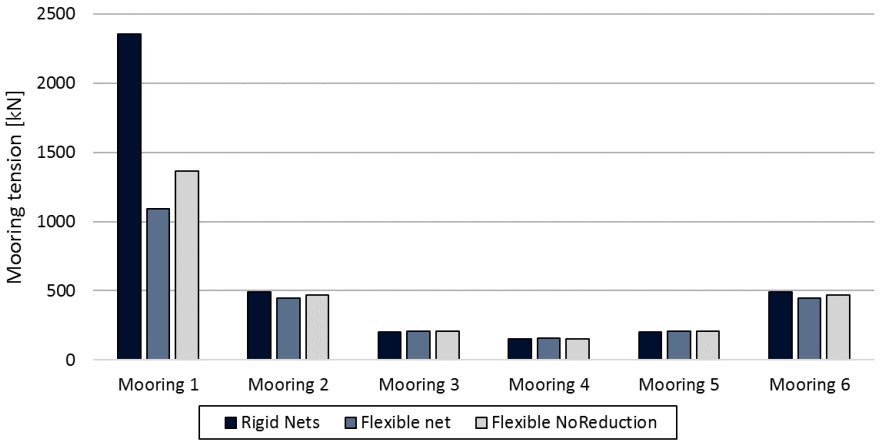

Figure 5.10: Mooring line tensions in 1.0 m/s current

Table 5.7: Percentage increase in maximum mooring line tension for different fish cage models

Current velocity [m/s]	Rigid vs Flex NoRed [%]	Rigid vs Flex [%]	Flex vs Flex NoRed [%]
0.1	0.944	1.65	0.696
0.5	26.7	50.5	18.9
1	72.1	114.9	24.9

5.3.2 Mooring Line Tension and Drift-Off

Simulations with EC9, EC10, EC11, and EC12 were carried out to study the motions of the coupled fish farm system, and the capacity of the mooring lines in wave and current conditions. The graphs in this chapter show that the vessel-shaped fish farm has reached its stable position and is in equilibrium for all the environmental conditions considered. At the initial drift-off, in the transient phase of simulations, there is high mooring tensions due to the sudden appearance of waves and currents. Such harsh environmental conditions will in reality build up over time, and the tension peaks will be significantly reduced.

By comparing the mooring line tensions with the drift-off distances, it is evident that the mooring tension increases for increasing drift-off distance, as more of the mooring line is lifted from the seabed. Furthermore, the vessel moves 7.8 meters forward when weathervaning in the early phase of simulation of EC12, and the tension decreases as sections of the mooring line is

lowered to the sea bottom. Mooring tension data for the four different environmental conditions are found in Table 5.8 below, and the time series is illustrated in Figure 5.11.

The mean displacement in x-direction increases by 91% from EC9 to EC10, and by 28% from EC10 to EC11. Further, the mooring line tension increases by 101% from EC9 to EC10, and by 78% from EC10 to EC11. For increasing wave heights and current velocities, the hydrodynamic forces on the system do not increase linearly. Thus, the increase in mooring tension and drift-off is nonlinear. The drift-off distances for the four different environmental conditions are found in Table 5.9, and the time series is illustrated in Figure 5.12.

The mooring tension and drift-off from EC12 and EC10 are found to be approximately equal. In simulations with the misaligned sea from EC12, current and wave loads will affect a larger area of the fish farm system. However, the total hydrodynamic forces on the system do not increase. This is concluded to be a result of interference between current and wave forces, which reduce the total resulting hydrodynamic loads on the vessel-shaped fish farm system.

The vessel motions and variations in mooring tension will increase for larger wave heights. Standard deviation is used to illustrate the increased variation in vessel motions and mooring tensions for different environmental conditions. The variation in mooring tension can be seen in Figure 5.11 and the standard deviation can be found in Table 5.8. Since the simulations run with constant current velocity and regular waves, the vessels translational motions in x-direction has low variances. Thus, the vessels pitch and heave motions are the main drivers for the variation in mooring tension in the conducted simulations.

Table 5.8: Mooring tension data for EC9, EC10, EC11, and EC12

EC	Maximum Tension [kN]	Mean Tension in Steady Phase [kN]	Standard Deviation in Steady Phase [kN]
EC9	1350	1120	3.65
EC10	3030	2250	21.9
EC11	6638	4006	40.4
EC12	2589	2206	18.8

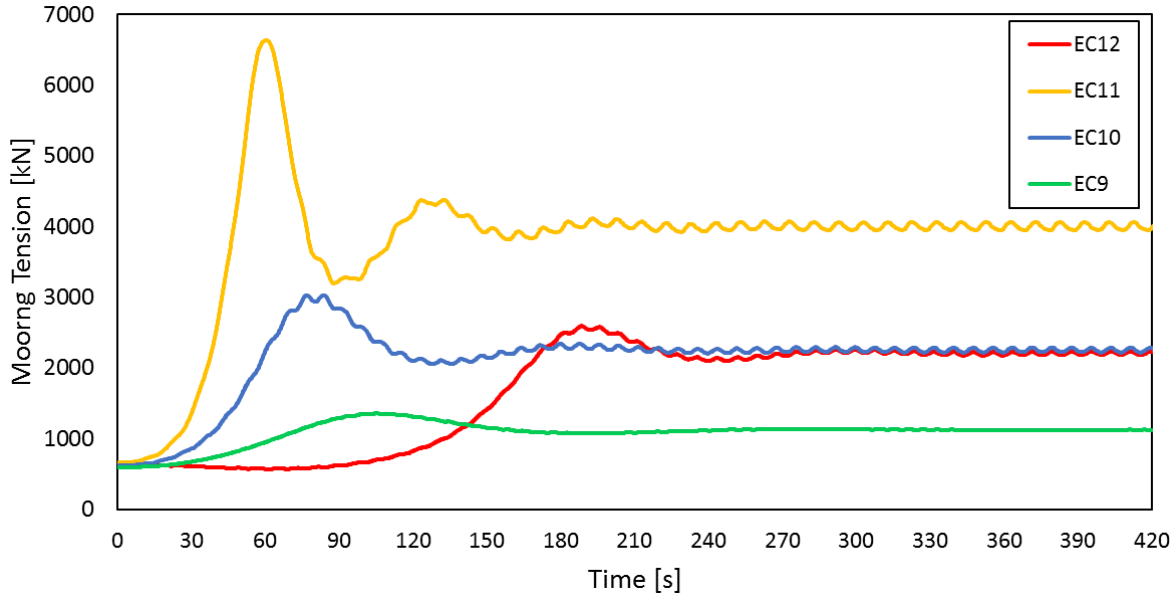

Figure 5.11: Maximum mooring line tension EC9, EC10, EC11, and EC12

Table 5.9: Displacement in x-dir for EC9, EC10, EC11, and EC12

EC	Max Displacement [m]	Mean Displacement in Steady Phase [m]	Standard Deviation in Steady Phase [m]
EC9	17.1	13.8	0.016
EC10	29.0	25.2	0.021
EC11	36.5	32.2	0.076
EC12	26.9	24.8	0.0394

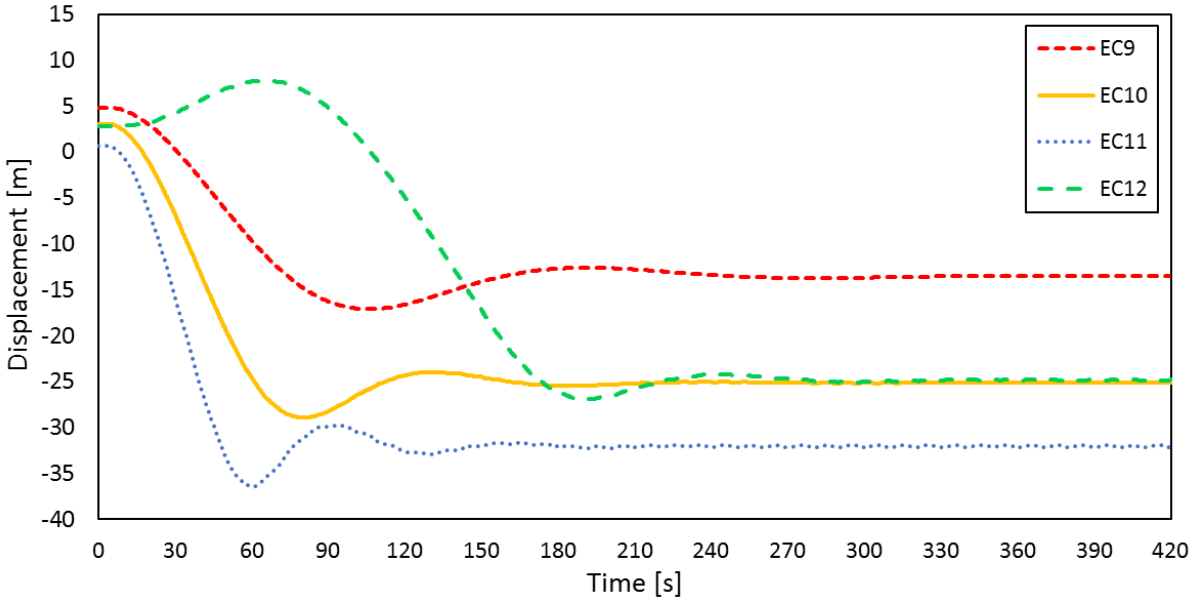

Figure 5.12: Displacement in X-dir for EC9, EC10, EC11, and EC12

5.3.3 Fish Net Tension in Current

A sensitivity study was conducted to study the effect of varying current velocities on axial tension in fish nets. Tensions from the foremost and rearmost fish net were studied in heading sea, with steady current velocities (Vc) from 0.2 m/s to 1.0 m/s. The tensions were measured from the connection between the vessel and the fish nets, in the upstream and downstream section of the net. The tension in the upstream section of the nets increase almost linearly for increasing current velocities. Total tension is lower in the rearmost net, due to shadowing effects from current velocity reduction factors.

For the downstream section of the nets, the tension decreases for Vc up to 0.6 m/s for the foremost net, and for Vc up to 1.0 m/s for the rearmost net. The upstream and downstream tensions are correlated, and the tension in the downstream section starts to increase when the tension in the upstream section reaches approximately 7800 N. Such a development in tension is a result of the fish nets deformation in current. When affected by current loads, the net will start to deform, and the bottom weights position is altered. The upstream section of the net is then stretched out from the bottom weight, while the tension in the downstream section of the net is reduced, as the bottom weight is lifted upwards. When the Vc increases further, the back of the net is affected by higher current loads, and the axial tension increase. As the front of the

net is in constant stretch from the bottom weight, the drag loads increase almost linearly and thus also the axial tension. Figure 5.13 illustrates the foremost net in Vc of 0.4 m/s and 0.8 m/s, and demonstrates the discussed conditions.

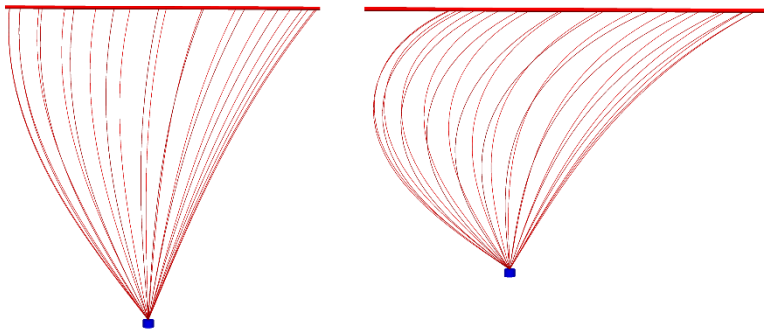

Figure 5.13: Net deformation from simulations with current velocity of 0.4 m/s (left) and 0.8 m/s (right)

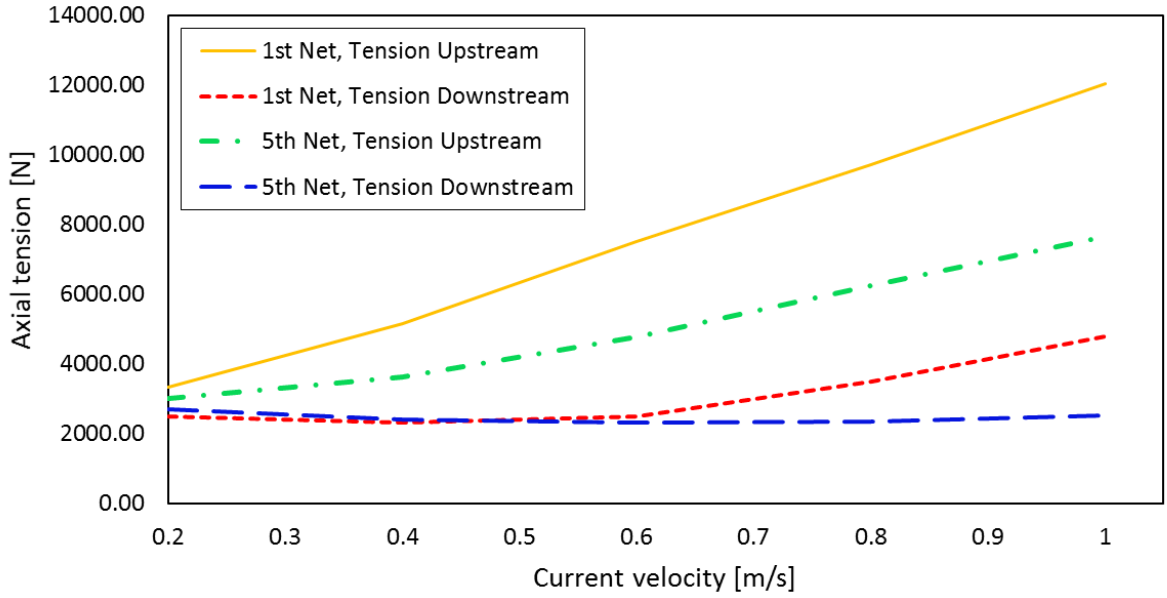

Figure 5.14: Fish net tension for different current velocities

5.3.4 Fish Net Tension in Waves and Current

The fish net located closest to the vessel bow will endure the largest hydrodynamic loads, since the other fish nets will benefit from the shadow effect due to current velocity reduction. Axial tension is therefore measured for the upstream and downstream section of the fish net located in closest proximity to the bow. Furthermore, the highest axial tension in the fish net is found

in the connection between the nets and the vessel, and the connection is therefore chosen as reference point for measuring tensions. The environmental conditions used for time domain simulations are EC9, EC10, and EC11.

Similar to the plots of mooring tensions and drift-off distances, the axial tension in fish nets go through the transient phase in the early stage of simulation. As previously mentioned, the environmental conditions will build up over a longer period of time in a real open sea, and the tensions in the transient phase are deemed unrealistic. The fish nets maximum, minimum, and mean tensions can be found in Table 5.10 and Table 5.11, together with the standard deviation. The tables also contain the percentage increase in tension and standard deviation from EC9 to EC10 and EC11.

For the upstream section of the net, the mean axial tension and standard deviation increase for an increase in wave height and current velocity. This increase is caused by increased vessel motions and the nonlinear coupling between the motions of the vessel, bottom weight, and fish net. The nonlinearities and coupled motions can be seen from the non-sinusoidal curves in Figure 5.15, Figure 5.16, and Figure 5.17.

As discussed and illustrated in Chapter 5.3.3, the tension in the downstream section of the net decreases for current velocities up to 0.6 m/s. This development is also found in the simulations using heading sea with a conjunction of waves and current. The values presented in Table 5.11 shows that the mean tensions decrease in the downstream section of the net, for increasing wave heights and current velocities. This development is caused by lifting of the bottom weight and the resulting net deformations. However, the standard deviation increases due to increased wave heights, and the maximum tension in the back of the net is higher for EC11 than EC9, despite lower mean tension.

Table 5.10: Axial tension in the steady phase, fish net upstream

EC	Max Tension [m]	Mean Tension [N]	Min Tension [N]	Standard Deviation [N]
EC9	3620	3309	2948	208
EC10	5092	4501	3601	480
EC11	6969	5444	4022	888
EC Compared	**Increase in Max Tension [%]**	**Increase in Mean Tension [%]**	**Increase in Mean Tension [%]**	**Increase in Standard Deviation [%]**
EC9-EC10	40.7	36.0	22.1	131
EC9-EC11	92.5	64.5	36.4	327

Table 5.11: Axial tension in the steady phase, fish net downstream

EC	Max Tension [m]	Mean Tension [N]	Min Tension [N]	Standard Deviation [N]
EC9	2671	2447	2210	137
EC10	2631	2384	1781	208
EC11	2967	2380	1686	353
EC Compared	**Increase in Max Tension [%]**	**Increase in Mean Tension [%]**	**Increase in Mean Tension [%]**	**Increase in Standard Deviation [%]**
EC9-EC10	-1.50	-2.54	-19.4	52.6
EC9-EC11	11.1	-2.74	-23.7	158.4

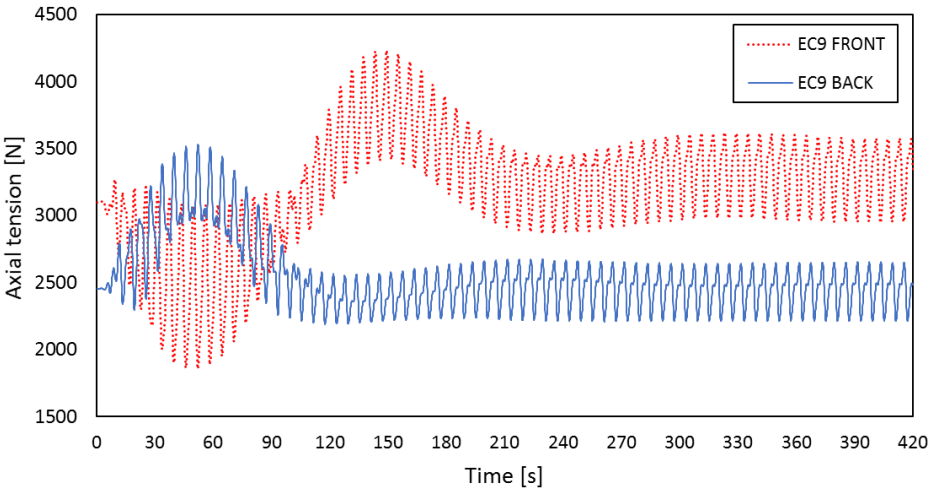

Figure 5.15: Axial tension in fish net, EC9

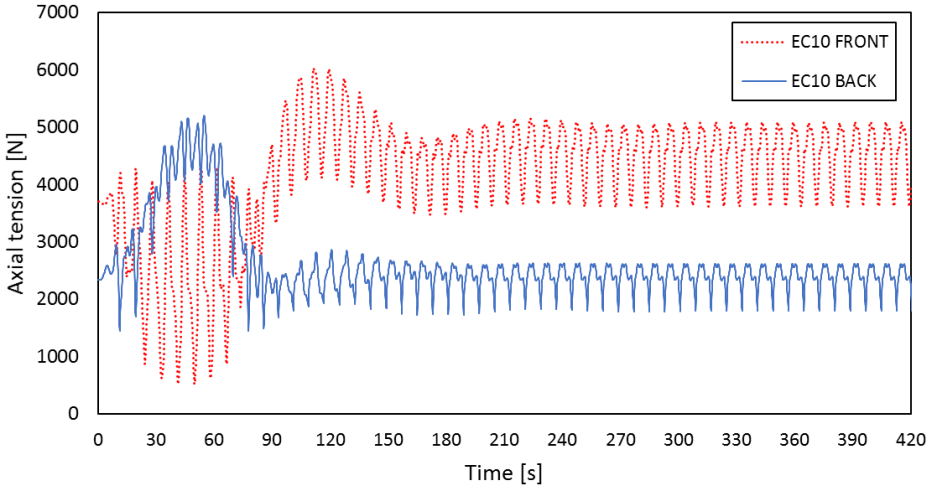

Figure 5.16: Axial tension in fish net, EC10

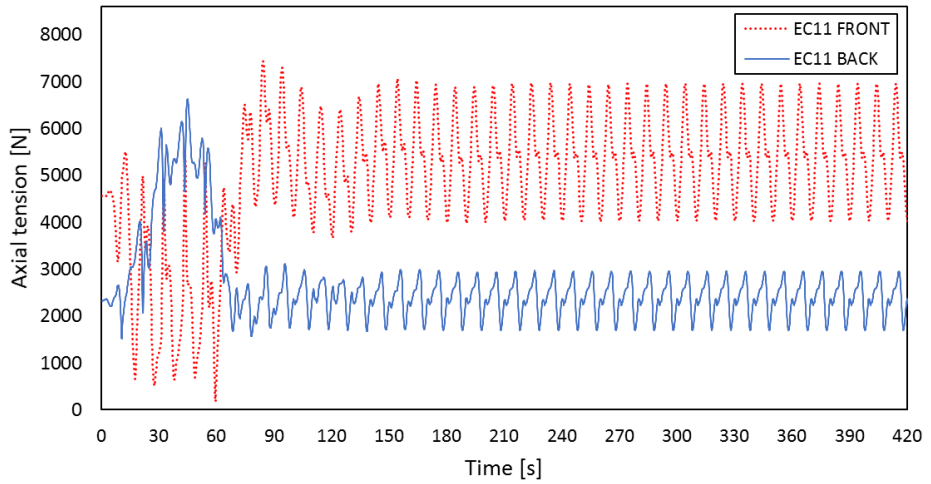

Figure 5.17: Axial tension in fish net, EC11

5.3.5 Sensitivity Study on Solidity Ratio

A sensitivity study was carried out by comparing the upstream fish net tension in the foremost net for varying solidity ratios from 0.15 to 0.45, with an increment of 0.05. As previously mentioned, drag forces on the fish net is mostly affected by current forces, and simulations with steady currents are therefore used for this sensitivity study. The current velocity used for simulations was set to 0.4 m/s, and additional parameters can be found in Table 5.3 and Table 5.4. The results clearly illustrate the increase in drag forces on the net for increased solidity ratios, and the axial tension in the net increase almost linearly. This development, and dependency between solidity ratio and fish net tensions, demonstrate the effects of fouling on the nets over time. Figure 5.18 illustrates the upstream fish net tension for varying solidity ratios.

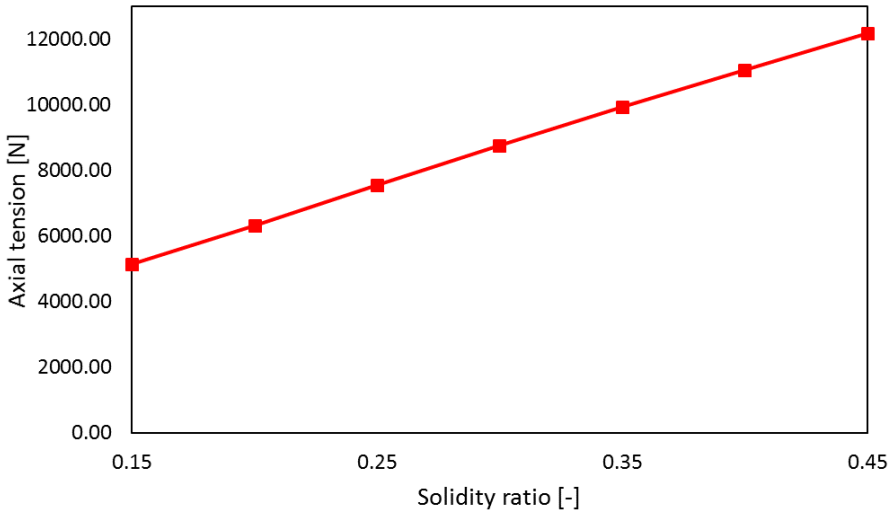

Figure 5.18: Upstream fish net tension for varying solidity ratios

6 Conclusions and Further Work

6.1 Conclusions

The objective of this thesis was to perform dynamic analyses of a floating vessel-shaped fish farm concept, using numerical simulation programs. The aim was to analyse vessel motions, mooring lines, and coupled vessel motions with installed mooring lines and fish nets.

Hydrodynamic properties of the vessel hull were performed in the frequency domain, from where the RAOs in heave, roll, and pitch were obtained. A convergence study on different panel models was carried out to verify sufficient accuracy for further studies, and significantly reduce the runtime and computational expenses for future simulations. Further, the effects of viscous drag forces on the vessel RAOs were studied, and it was found that the highest amplitudes of motion were reduced, while the effect on vessel motions outside the peak area was negligible. The hydrodynamic data acquired from frequency domain analyses was exported from Wadam to SIMO, the program used for time domain analysis of the vessel hull and simplified mooring system.

Quasi-static time domain simulations with irregular waves were carried out using the numerical simulation program SIMO. The vessel and mooring lines coupled dynamics were studied, and the mooring lines functionality and capacity were analysed. The mooring lines capacity was found to be insufficient for simulations with a significant wave height of 4 meters or higher. Based on the mooring lines performance in SIMO, new mooring line parameters were established for the fully coupled time domain simulations in SIMO-Riflex.

The numerical simulation program SIMO-Riflex was used to generate the fully coupled time domain analysis of the vessel-shaped fish farm, with installed fish nets and mooring lines. A sensitivity study was carried out by comparing mooring tensions in steady current conditions, for three different fish net models; rigid model, flexible model, and flexible model with no current velocity reduction factor. It was concluded that the rigid model overestimates drag force on the nets mainly due to neglecting net deformation, with an overestimation of 114.9 % in 1.0

m/s steady current. Furthermore, the flexible fish nets with no current velocity reduction factor was found to overestimate the drag forces due to neglecting shadowing effects, with an overestimation of 24.9 % in 1.0 m/s steady current. It is therefore recommended that neither of the simplified models should be used for dynamic analyses of aquaculture systems.

Development of tensions in the foremost and rearmost fish nets were studied in steady current conditions, with velocities varying from 0.2 m/s to 1.0 m/s. For the downstream section of the net, it was found that the tension decreases for increasing current velocities up to 0.6 m/s. The decrease in tension was found to be induced by lifting of the bottom weight, and resulting net deformation. In the upstream section of the net, the drag loads were found to increase almost linearly with increasing current velocities. To further study the fish net tension development, analyses with a conjunction of regular waves and steady currents were carried out. The results demonstrated the effect of nonlinear coupled motions, and further confirmed the mutual dependency between the fish nets deformation and the forces affecting it.

Motions of the coupled fish farm system and efficiency of mooring lines were studied from time domain simulations with regular waves and steady currents, for three unidirectional and one multidirectional sea condition. The simulation results demonstrated the nonlinear increase in hydrodynamic loads on the system, and the vessels pitch and heave motions were found to be the main drivers of variation in mooring tensions. Comparing a multidirectional and a unidirectional sea condition showed insignificant differences in hydrodynamic forces on the system.

6.2 Further Work

The work with analysis of fish farm systems for open sea is a complex and novel engineering challenge, and further work must be carried out to further strengthen knowledge on dynamics of aquaculture installations. The recommendations for further work and improvements in this chapter is based on the dynamic analyses conducted in this thesis, and the presented results.

For the present implementation in SIMO-Riflex, the drag force on net panels depends on current velocity and the net solidity. Simplified current velocity reduction factors were implemented in

this study, and since Riflex is not capable of calculating the current velocity reduction factors, a more detailed assessment is recommended for further studies. Separate velocity reduction factors should be implemented for each section of the net, with values depending on the current direction and the deformation of the upstream panels.

Time domain simulations with irregular sea could not be carried out in the present work, as irregular waves were not supported in Riflex at the time of writing. For future studies, it is recommended that the vessel-shaped fish farm system is studied in irregular wave conditions. Furthermore, it is recommended that additional multidirectional wave and current conditions are studied in time domain analyses, to better understand the motions of the vessel-shaped fish farm concept.

It is recommended that further studies aim to optimize the geometry of the vessel-shaped fish farm. The vessel geometry can be optimized by altering the main vessel geometries and conducting analysis of the corresponding vessel motions. Costs and production efficiency should also be included for optimization of the vessel geometry.

7 References

AKSNES, V. 2016. Modelling of Aquaculture Net Cages in SIMA, MARINTEK.

AKVAGROUP. 2016. AKVA group bildegalleri [Online]. Available: http://www.akvagroup.com/nyheter/bildegalleri [Accessed 06.02.2017].

AQUALINE. 2016. Aqualine not tabell - Nylon [Online]. Available: http://aqualine.no/media/not/nottabell-nylon.pdf [Accessed 11.03.2017].

ASCHE, F., GUTTORMSEN, A. G. & NIELSEN, R. 2013. Future challenges for the maturing Norwegian salmon aquaculture industry: An analysis of total factor productivity change from 1996 to 2008. Aquaculture, 396-399, 43-50.

BACHYNSKI, E. E. 2014. Design and Dynamic Analysis of Tension Leg Platform Wind Turbines. Philosophiae Doctor, NTNU.

BENNETT. 2016. Havfarm [Online]. Available: http://www.bennett.no/jobber/havfarm/ [Accessed 23.01.2017].

BJELLAND, H. V., FØRE, M., LADER, P., KRISTIANSEN, D., HOLMEN, I. M., FREDHEIM, A., GRØTLI, E. I., FATHI, D. E., OPPEDAL, F., UTNE, I. B. & SCHJØLBERG, I. 2015. Exposed Aquaculture in Norway. OCEANS 2015 - MTS/IEEE Washington.

BORGMAN, L. E. 1967. Random Hydrodynamic Forces on Objects. The Annals of Mathematical Statistics, 38, 37-51.

CHAKRABARTI, S. 2005. Elsevier Ocean Engineering Series: Handbook of Offshore Engineering (2-volume set), Volume 1 and 2, St. Louis, St. Louis, GB: Elsevier Science.

CHAKRABARTI, S. K. 1987. Hydrodynamics of Offshore Structures. Southampton, Computational Mechanics Publications.

DNV 2010. SESAM User Manual WADAM - Wave Analysis by Diffraction and Morison Theory. Det Norske Veritas.

DNV 2011. SESAM User Manual HydroD, Wave load & stability analysis of fixed and floating structures.

DNV GL 2014. Environmental conditions and environmental loads, DNV-RP-C205.

DNV GL. 2016. SESAM MARINE, Manage risk of marine operations with visual simulation of calculations. Available: https://www.dnvgl.com/services/software-for-marine-operations-sesam-marine-2321 [Accessed 14.04.2017].

EGERSUND NET. 2016. Kjegleformet Notpose [Online]. Available: http://www.egersundnet.no/produkter/notposer/kjegleformet-notpose [Accessed 15.04.2017].

ERICKSON, L. L. 1990. Panel Methods-An Introduction. NASA TP-2995. Available: https://ntrs.nasa.gov/archive/nasa/casi.ntrs.nasa.gov/19910009745.pdf [Accessed 28.01.2017].

FALTINSEN, O. M. 1990. Sea Loads on Ships and Offshore Structures. Cambridge University Press.

FREDRIKSSON, D. W. 2001. Open ocean fish cage and mooring system dynamics. PhD thesis, University of New Hampshire.

FREDRIKSSON, D. W., SWIFT, M. R., EROSHKIN, O., TSUKROV, I., IRISH, J. D. & CELIKKOL, B. 2005. Moored fish cage dynamics in waves and currents. Oceanic Engineering, IEEE Journal of, 30, 28-36.

FREDRIKSSON, D. W., SWIFT, M. R., IRISH, J. D., TSUKROV, I. & CELIKKOL, B. 2003. Fish cage and mooring system dynamics using physical and numerical models with field measurements. Aquacultural Engineering, 27, 117-146.

FU, S., XU, Y., HU, K., ZHONG, Q. & LI, R. 2014. Experimental investigation on hydrodynamics of a fish cage floater-net system in oscillatory and steady flows by forced oscillation tests. Journal of Ship Research, 58, 20-29.

GRAN, S. 1992. A Course in Ocean Engineering. Developments in Marine Technology. Elsevier Science Publishers, Amsterdam - London - New York - Tokyo 1992.

GUDMESTAD, O. T. 2015. Marine technology and operations : theory & practice, Southampton, WIT Press.

HASSELMAN K., BARNETT T.P., BOUWS E., CARLSON H., CARTWRIGHT D.E., ENKE K., EWING J.A., GICNAPP H., HASSELMANN D.E., KRUSEMAN P., MEERBURG A., MÜLLER P., OLBERS D. J., RICHTER K., SELL W. & WALDEN H. 1973. Measurements of Wind-Wave Growth and Swell Decay During the Joint North sea Wave Project (JONSWAP). Hamburg.

HUANG, C.-C., TANG, H.-J. & LIU, J.-Y. 2008. Effects of waves and currents on gravity-type cages in the open sea. Aquacultural Engineering, 38, 105-116.

ISHIE, J. U., MUK, C. O. & KAI, W. 2016. Structural Dynamic Analysis of Semi-submersible Floating Vertical Axis Wind Turbines. University of Stavanger, Norway.

JOURNÉE, J. M. J. & MASSIE, W. W. 2001. Offshore Hydromechanics, Delft University of Technology.

KAWAKAMI, T. 1964. The theory of designing and testing fishing nets in model. In: Fishing Gear of the World 2, Fishing News, London, pp. 471-482.

KESHAVARZ, L. 2011. Analysis of Mooring System for a Floating Production System. M.Sc.Eng., Norwegian University of Science and Technology.

KRISTIANSEN, D., LADER, P., JENSEN, Ø. & FREDRIKSSON, D. 2015. Experimental study of an aquaculture net cage in waves and current. China Ocean Engineering, 29, 325-340.

KRISTIANSEN, T. & FALTINSEN, O. M. 2012. Modelling of current loads on aquaculture net cages. Journal of Fluids and Structures, 34, 218-235.

LADER, P., JENSEN, A., SVEEN, J. K., FREDHEIM, A., ENERHAUG, B. & FREDRIKSSON, D. 2007. Experimental investigation of wave forces on net structures. Applied Ocean Research, 29, 112-127.

LADER, P. F. & ENERHAUG, B. 2005. Experimental investigation of forces and geometry of a net cage in uniform flow. Oceanic Engineering, IEEE Journal of, 30, 79-84.

LADER, P. F., ENERHAUG, B., FREDHEIM, A. & KROKSTAD, J. 2003. Modeling of 3D Net Structures Exposed to Waves and Current, Trondheim, Norway, SINTEF Fisheries and Aquaculture.

LADER, P. F. & FREDHEIM, A. 2006. Dynamic properties of a flexible net sheet in waves and current—A numerical approach. Aquacultural Engineering, 35, 228 - 238.

LI, L., FU, S., XU, Y., WANG, J. & YANG, J. 2013. Dynamic responses of floating fish cage in waves and current. Ocean Engineering, 72, 297 - 303.

LI, L., JIANG, Z. & ONG, M. C. 2016. A Preliminary Study of a Vessel-Shaped Offshore Fish Farm Concept. ASME 36th International Conferences on Ocean, Offshore and Artic Engineering OMAE2017, 2017 Trondheim, Norway.

LØLAND, G. 1991. Current forces on and flow through fish farms. Doctoral Thesis, Division of Marine Hydrodynamics Norwegian Institute of Technology.

LØLAND, G. 1993. Current forces on, and water flow through and around, floating fish farms. Journal of the European Aquaculture Society, 1, 72-89.

MARINTEK 2015. SIMO User Manual.

MARINTEK 2016a. Riflex 4.8.5 User Guide.

MARINTEK 2016b. RIFLEX Theory Manual.

MARINTEK 2017. SIMO Theory Manual.

MOSKOWITZ, L. 1964. Estimates of the power spectrums for fully developed seas for wind speeds of 20 to 40 knots. Journal of Geophysical Research, 69, 5161-5179.

NAESS, A. & MOAN, T. 2013. Stochastic Dynamics of Marine Structures, Cambridge University Press.

ORCINA. 2016. Displacement RAOs [Online]. Available: https://www.orcina.com/SoftwareProducts/OrcaFlex/Documentation/Help/Content/html/VesselTheory,RAOsandPhases.htm [Accessed 06.02.2017].

PLASTFORUM. 2016. Nedsenkbare Atlantis på vei mot noe [Online]. Plastforum. Available: http://www.plastforum.no/default.asp?menu=8&id=6296 [Accessed 13.01.2017].

REFAMED. 2015. TLC DESIGN [Online]. Available: http://www.refamed.com/gabbie_mare/tlc_system.html [Accessed 12.01.2017].

REINERTSEN, H., DAHLE, L. A., JØRGENSEN, L. & TVINNEREIM, K. 1993. Fish Farming Technology, A.A. Balkema, P.O.Box 1675, 3000 BR Rotterdam, Netherlands.

RHO, Y.-H., KIM, K., JO, C.-H. & KIM, D.-Y. 2013. Static and dynamic mooring analysis – Stability of floating production storage and offloading (FPSO) risers for extreme environmental conditions. International Journal of Naval Architecture and Ocean Engineering, 5, 179-187.

SARPKAYA, T. & ISAACSON, M. 1981. Mechanics of wave forces on offshore structures, New York, Van Nostrand Reinhold.

SHAO, Y. L., YOU, J. & GLOMNES, E. B. 2016. Stochastic linearization and its application in motion analysis of cylindrical floating structure with bilge boxes. International Conference on Ocean, Offshore and Arctic Engineering OMAE2016. Busan, South Korea.

SUNDE, L. M., HEIDE, M. A., HAGEN, N., FREDHEIM, A., FORÅS, E. & PRESTVIK, Ø. 2003. Teknologistatus i havbruk. SINTEF fiskeri og havbruk. Report number: STF80 A034002.

TAGHIPOUR, R., PEREZ, T. & MOAN, T. 2008. Hybrid frequency–time domain models for dynamic response analysis of marine structures. Ocean Engineering, 35, 685-705.

TIAN, X., ONG, M. C., YANG, J. & MYRHAUG, D. 2014. Large-eddy simulation of the flow normal to a flat plate including corner effects at a high Reynolds number. Journal of Fluids and Structures, 49, 149-169.

TSUKROV, I., EROSHKIN, O., FREDRIKSSON, D., SWIFT, M. R. & CELIKKOL, B. 2003. Finite element modeling of net panels using a consistent net element. Ocean Engineering, 30, 251-270.

WOLFRAM, J. 1999. On alternative approaches to linearization and Morison's equation for wave forces. Proceedings of the Royal Society of London. Series A: Mathematical, Physical and Engineering Sciences, 455, 2957-2974.

ZHAO, Y.-P., LI, Y.-C., DONG, G.-H., GUI, F.-K. & TENG, B. 2007. A numerical study on dynamic properties of the gravity cage in combined wave-current flow. Ocean Engineering, 34, 2350-2363.

Appendix A - Frequency Domain Results

A-1 Comparison of RAOs with different frequency sets

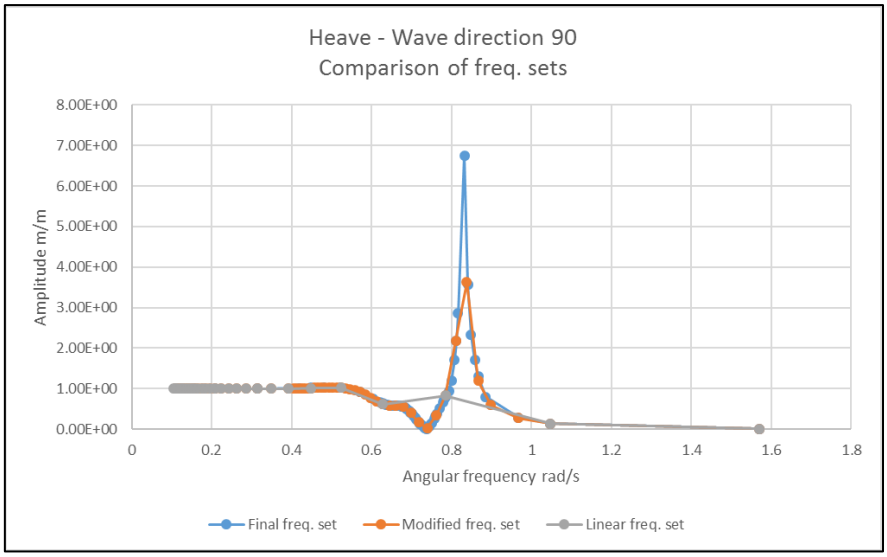

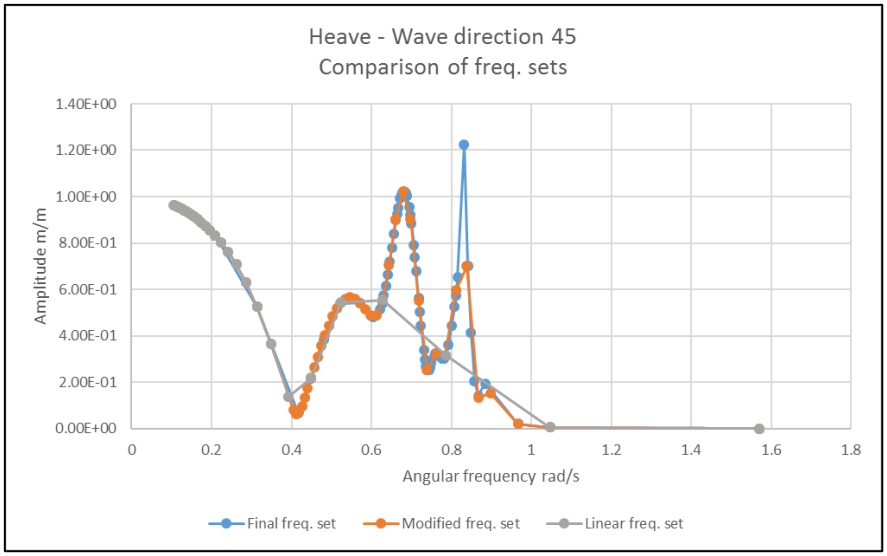

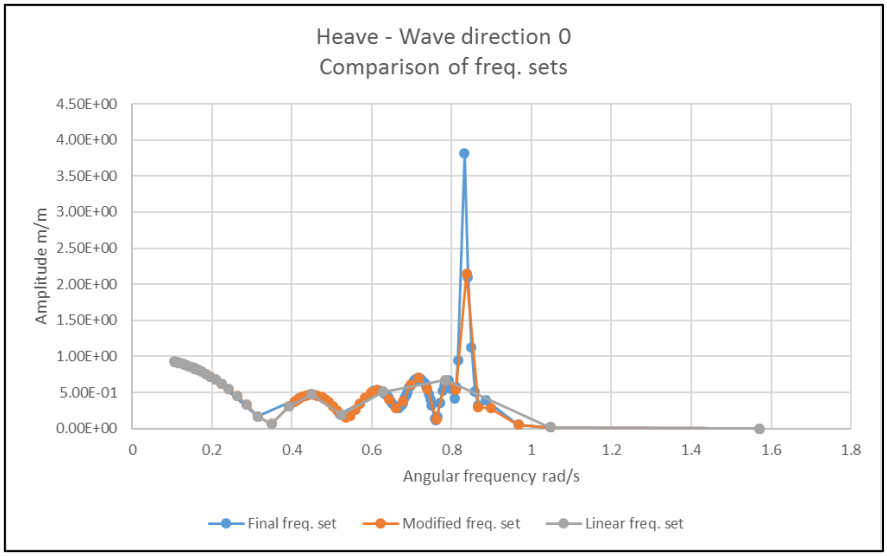
Heave - Wave direction 0
Comparison of freq. sets
Amplitude m/m
4.50E+00
4.00E+00
3.50E+00
3.00E+00
2.50E+00
2.00E+00
1.50E+00
1.00E+00
5.00E-01
0.00E+00
0
0.2
0.4
0.6
0.8
1
1.2
1.4
1.6
1.8
Angular frequency rad/s
Final freq. set
Modified freq. set
Linear freq. set

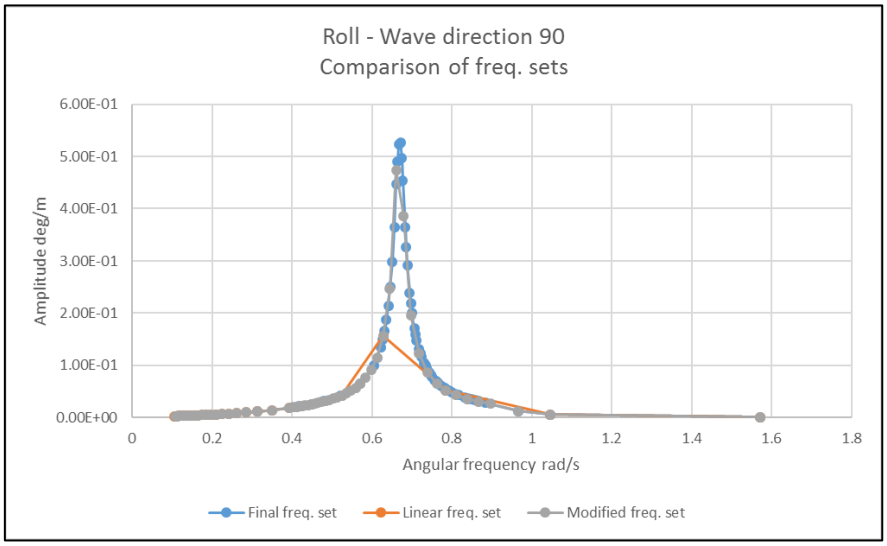
Roll - Wave direction 90
Comparison of freq. sets
Amplitude deg/m
6.00E-01
5.00E-01
4.00E-01
3.00E-01
2.00E-01
1.00E-01
0.00E+00
0
0.2
0.4
0.6
0.8
1
1.2
1.4
1.6
1.8
Angular frequency rad/s
Final freq. set
Linear freq. set
Modified freq. set

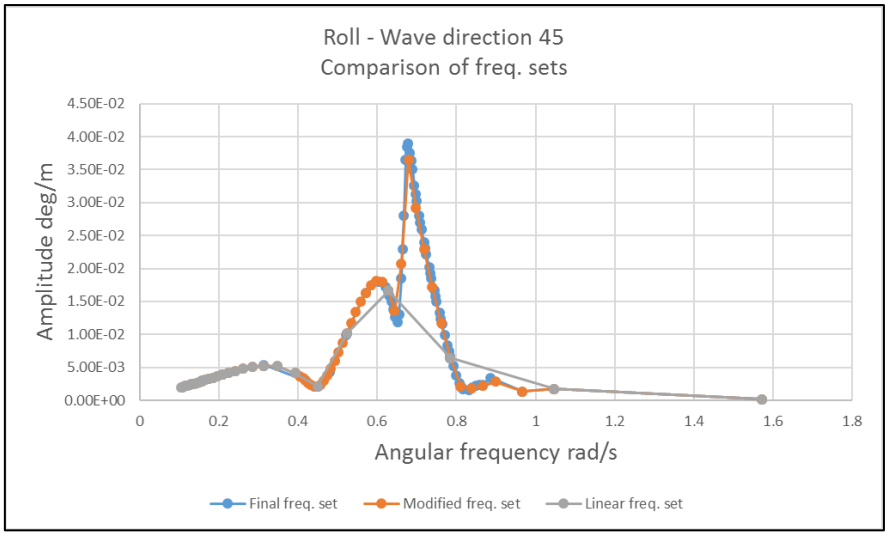
Roll - Wave direction 45
Comparison of freq. sets
Amplitude deg/m
4.50E-02
4.00E-02
3.50E-02
3.00E-02
2.50E-02
2.00E-02
1.50E-02
1.00E-02
5.00E-03
0.00E+00
0
0.2
0.4
0.6
0.8
1
1.2
1.4
1.6
1.8
Angular frequency rad/s
Final freq. set
Modified freq. set
Linear freq. set

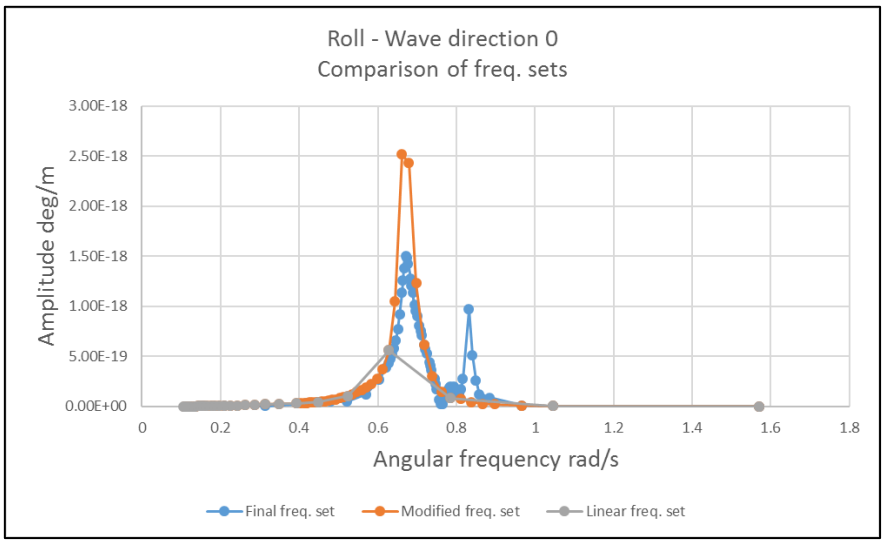
Roll - Wave direction 0
Comparison of freq. sets
Amplitude deg/m
3.00E-18
2.50E-18
2.00E-18
1.50E-18
1.00E-18
5.00E-19
0.00E+00
0
0.2
0.4
0.6
0.8
1
1.2
1.4
1.6
1.8
Angular frequency rad/s
Final freq. set
Modified freq. set
Linear freq. set

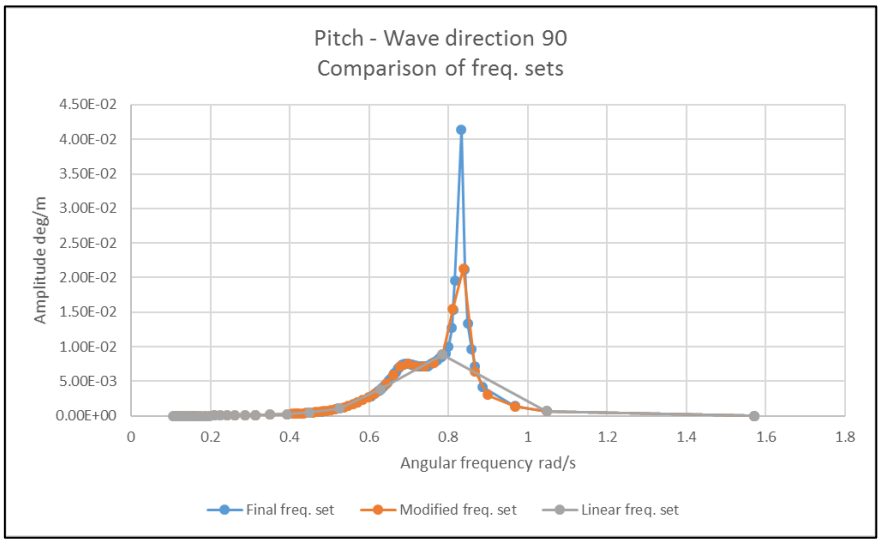
Pitch - Wave direction 90
Comparison of freq. sets
Amplitude deg/m
4.50E-02
4.00E-02
3.50E-02
3.00E-02
2.50E-02
2.00E-02
1.50E-02
1.00E-02
5.00E-03
0.00E+00
0
0.2
0.4
0.6
0.8
1
1.2
1.4
1.6
1.8
Angular frequency rad/s
Final freq. set
Modified freq. set
Linear freq. set

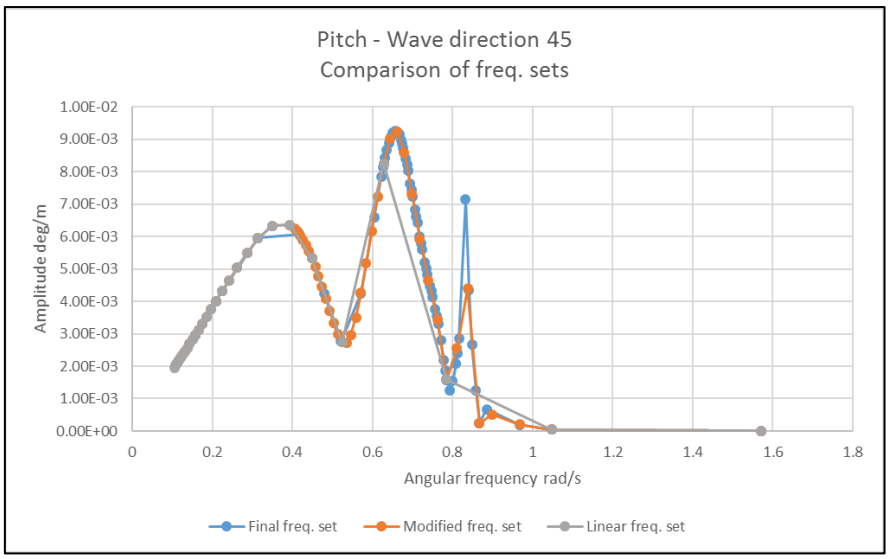
Pitch - Wave direction 45
Comparison of freq. sets
Amplitude deg/m
1.00E-02
9.00E-03
8.00E-03
7.00E-03
6.00E-03
5.00E-03
4.00E-03
3.00E-03
2.00E-03
1.00E-03
0.00E+00
0
0.2
0.4
0.6
0.8
1
1.2
1.4
1.6
1.8
Angular frequency rad/s
Final freq. set
Modified freq. set
Linear freq. set

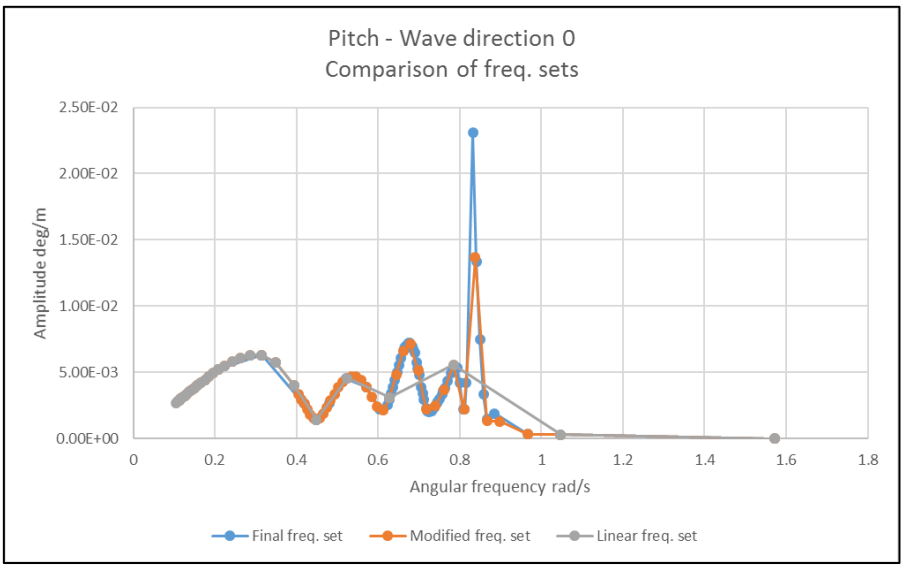
Pitch - Wave direction 0
Comparison of freq. sets
2.50E-02
2.00E-02
1.50E-02
1.00E-02
5.00E-03
0.00E+00
Amplitude deg/m
0
0.2
0.4
0.6
0.8
1
1.2
1.4
1.6
1.8
Angular frequency rad/s
Final freq. set
Modified freq. set
Linear freq. set

A-2 Panel model comparison

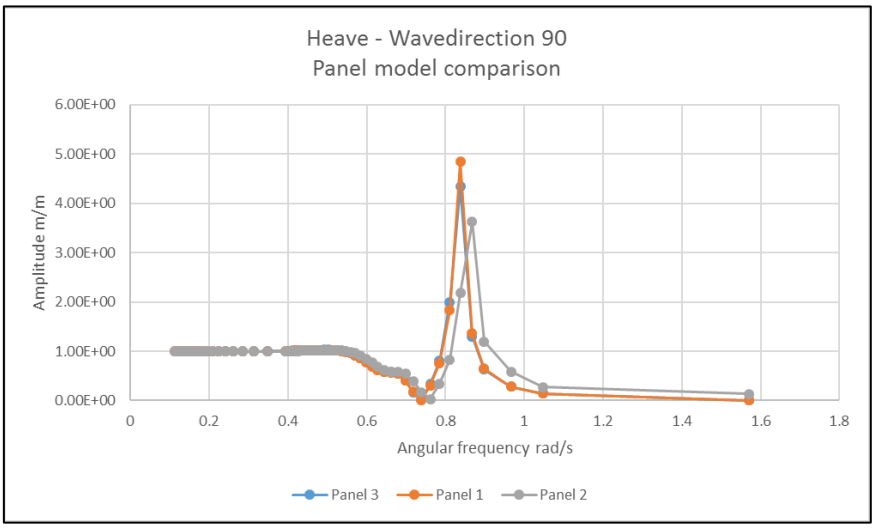

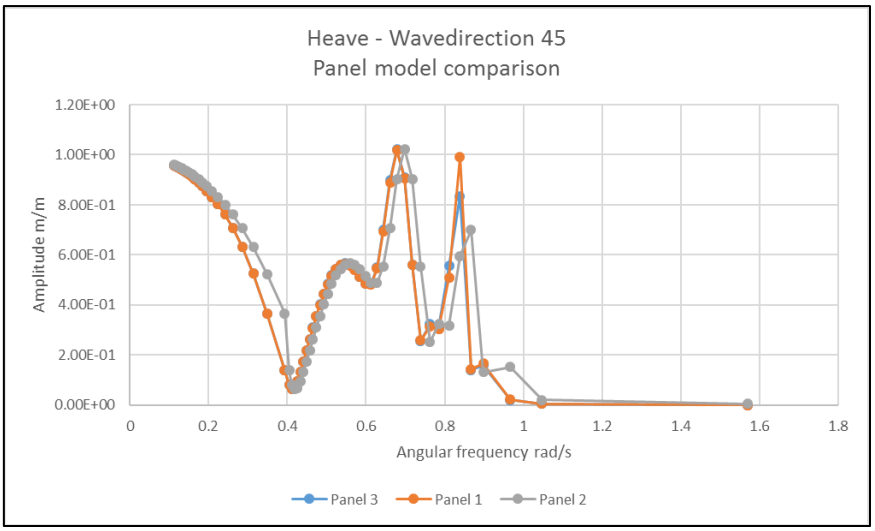

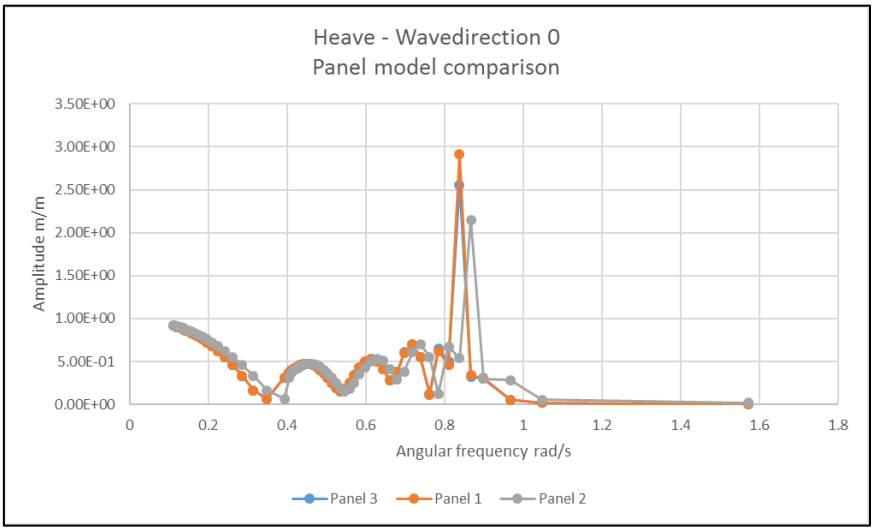

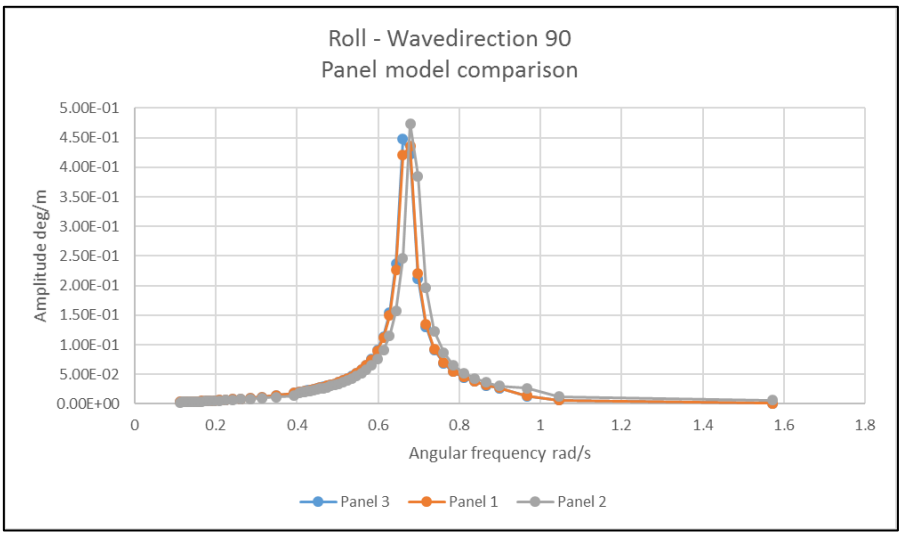
Roll - Wavedirection 90
Panel model comparison
Amplitude deg/m
5.00E-01
4.50E-01
4.00E-01
3.50E-01
3.00E-01
2.50E-01
2.00E-01
1.50E-01
1.00E-01
5.00E-02
0.00E+00
0
0.2
0.4
0.6
0.8
1
1.2
1.4
1.6
1.8
Angular frequency rad/s
Panel 3
Panel 1
Panel 2

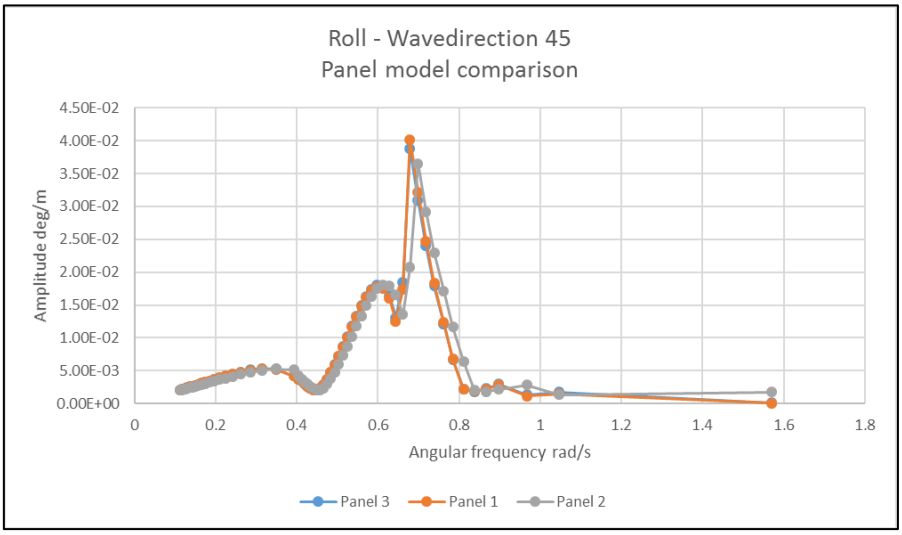
Roll - Wavedirection 45
Panel model comparison
Amplitude deg/m
4.50E-02
4.00E-02
3.50E-02
3.00E-02
2.50E-02
2.00E-02
1.50E-02
1.00E-02
5.00E-03
0.00E+00
0
0.2
0.4
0.6
0.8
1
1.2
1.4
1.6
1.8
Angular frequency rad/s
Panel 3
Panel 1
Panel 2

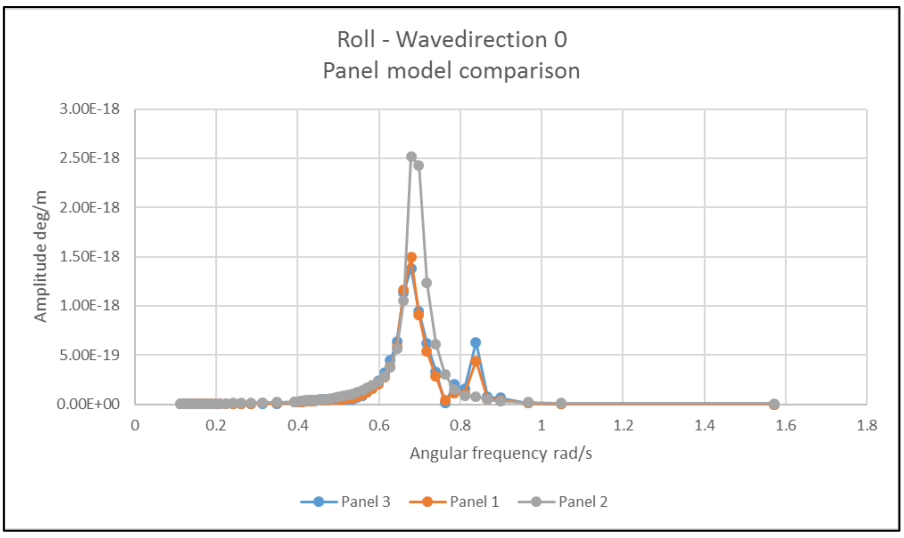
Roll - Wavedirection 0
Panel model comparison
Amplitude deg/m
3.00E-18
2.50E-18
2.00E-18
1.50E-18
1.00E-18
5.00E-19
0.00E+00
0
0.2
0.4
0.6
0.8
1
1.2
1.4
1.6
1.8
Angular frequency rad/s
Panel 3
Panel 1
Panel 2

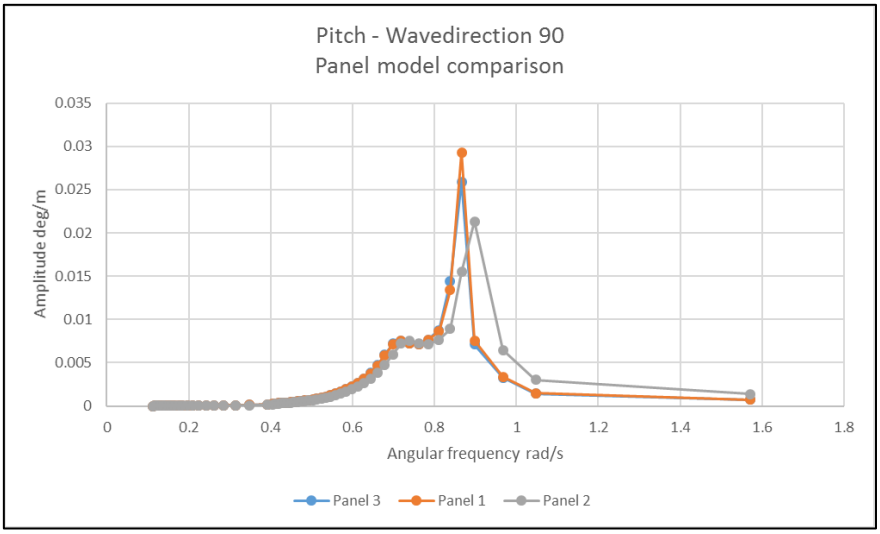
Pitch - Wavedirection 90
Panel model comparison
Amplitude deg/m
0.035
0.03
0.025
0.02
0.015
0.01
0.005
0
0
0.2
0.4
0.6
0.8
1
1.2
1.4
1.6
1.8
Angular frequency rad/s
Panel 3
Panel 1
Panel 2

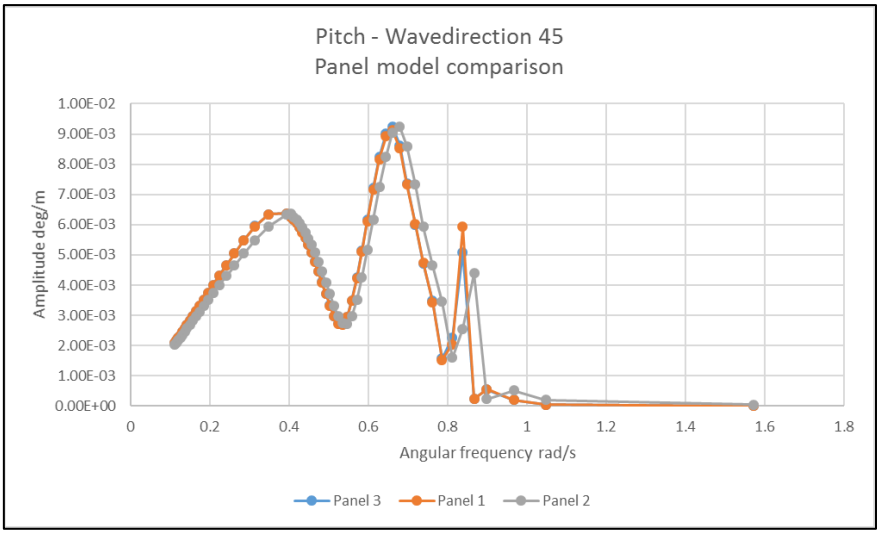
Pitch - Wavedirection 45
Panel model comparison
Amplitude deg/m
1.00E-02
9.00E-03
8.00E-03
7.00E-03
6.00E-03
5.00E-03
4.00E-03
3.00E-03
2.00E-03
1.00E-03
0.00E+00
0
0.2
0.4
0.6
0.8
1
1.2
1.4
1.6
1.8
Angular frequency rad/s
Panel 3
Panel 1
Panel 2

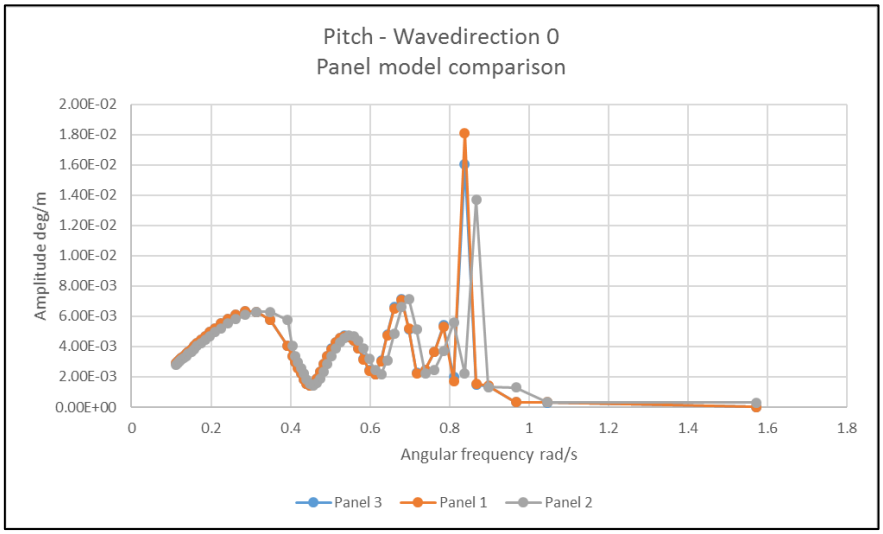
Pitch - Wavedirection 0
Panel model comparison
Amplitude deg/m
2.00E-02
1.80E-02
1.60E-02
1.40E-02
1.20E-02
1.00E-02
8.00E-03
6.00E-03
4.00E-03
2.00E-03
0.00E+00
0
0.2
0.4
0.6
0.8
1
1.2
1.4
1.6
1.8
Angular frequency rad/s
Panel 3
Panel 1
Panel 2

A-3 Comparison of included/excluded viscous effects

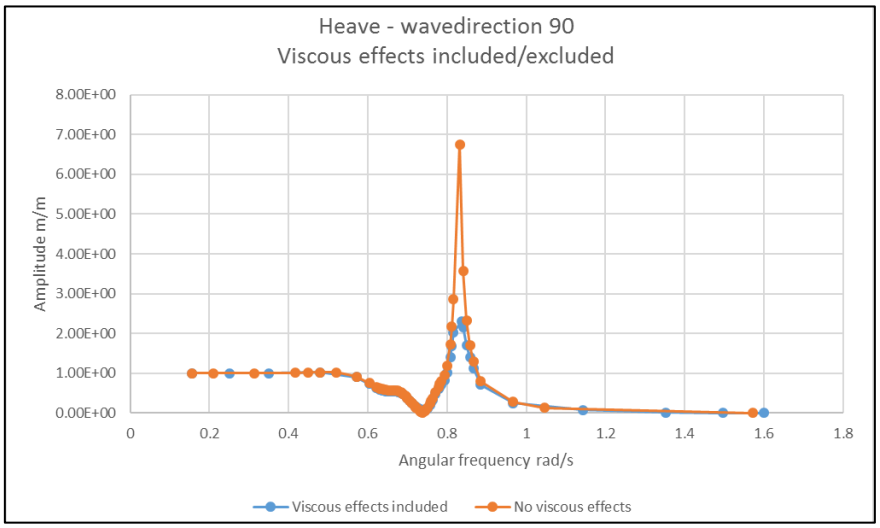

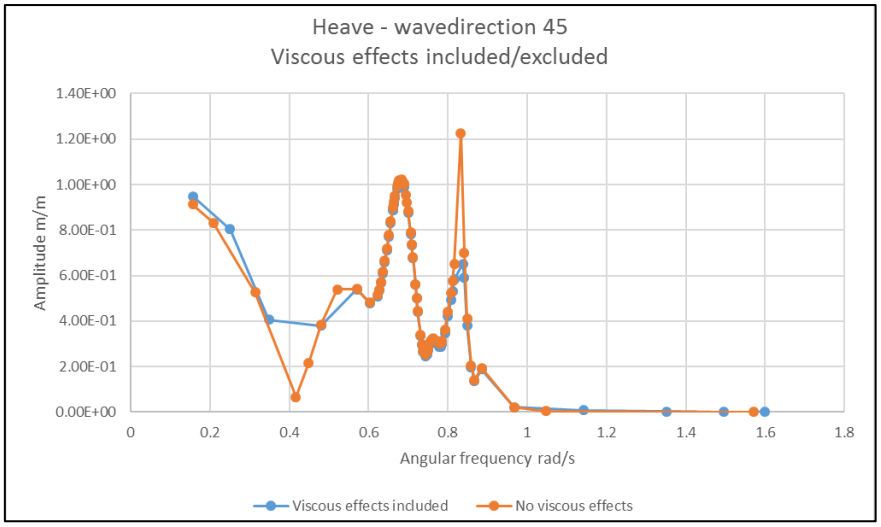

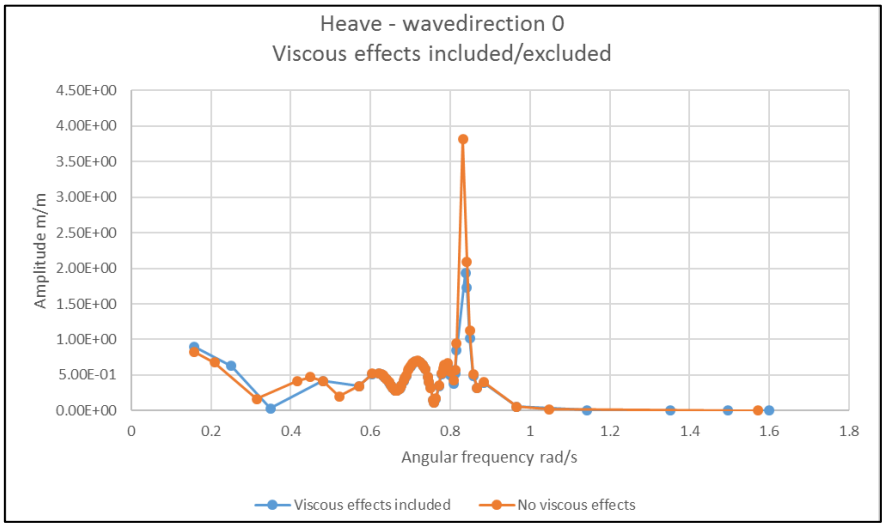

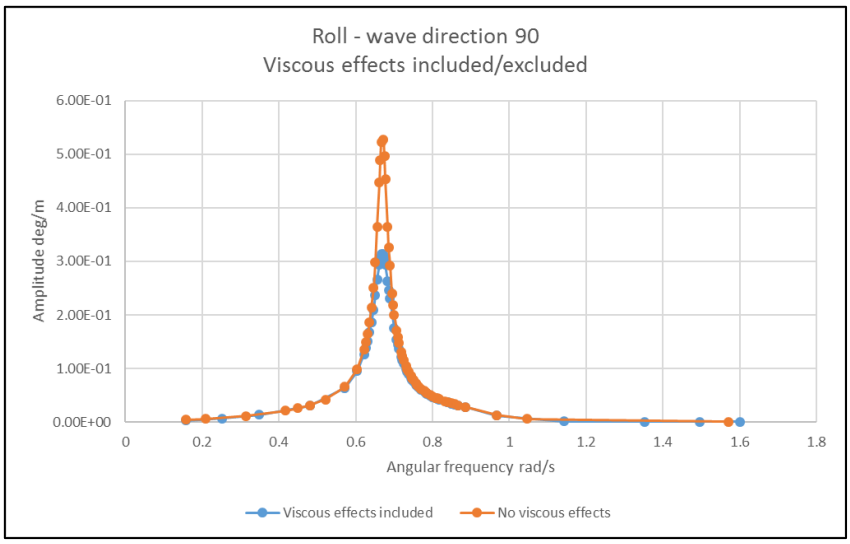
Roll - wave direction 90
Viscous effects included/excluded
Amplitude deg/m
6.00E-01
5.00E-01
4.00E-01
3.00E-01
2.00E-01
1.00E-01
0.00E+00
0
0.2
0.4
0.6
0.8
1
1.2
1.4
1.6
1.8
Angular frequency rad/s
Viscous effects included
No viscous effects

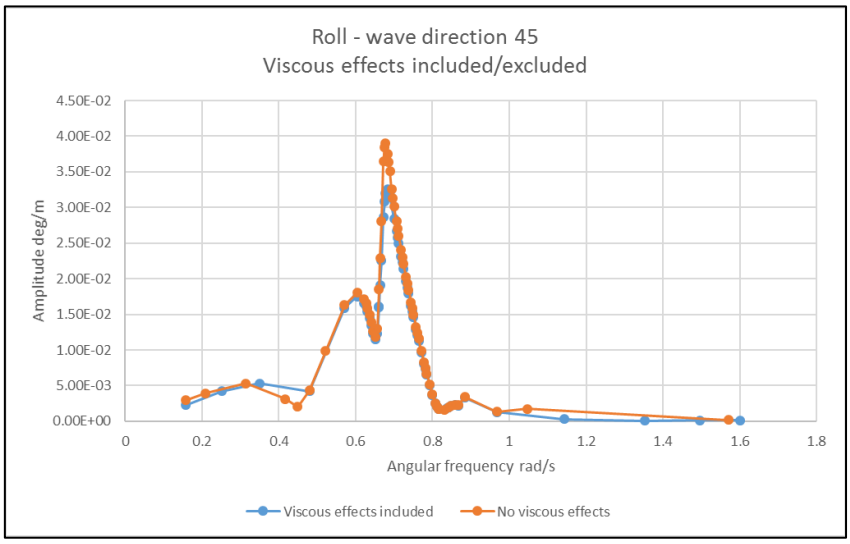
Roll - wave direction 45
Viscous effects included/excluded
Amplitude deg/m
4.50E-02
4.00E-02
3.50E-02
3.00E-02
2.50E-02
2.00E-02
1.50E-02
1.00E-02
5.00E-03
0.00E+00
0
0.2
0.4
0.6
0.8
1
1.2
1.4
1.6
1.8
Angular frequency rad/s
Viscous effects included
No viscous effects

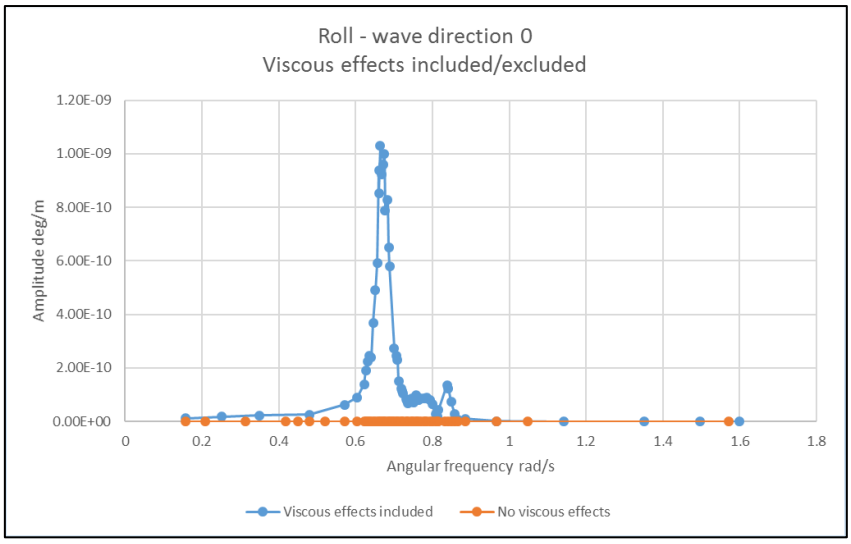
Roll - wave direction 0
Viscous effects included/excluded
Amplitude deg/m
1.20E-09
1.00E-09
8.00E-10
6.00E-10
4.00E-10
2.00E-10
0.00E+00
0
0.2
0.4
0.6
0.8
1
1.2
1.4
1.6
1.8
Angular frequency rad/s
Viscous effects included
No viscous effects

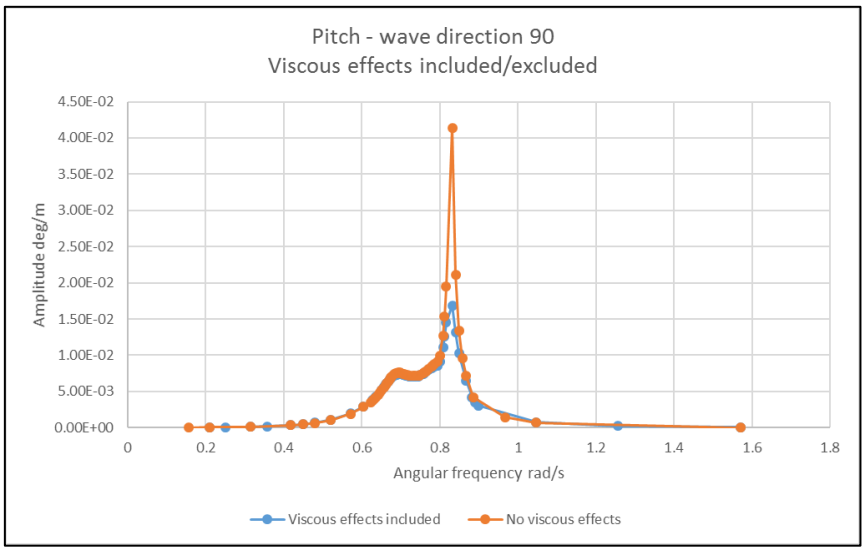
Pitch - wave direction 90
Viscous effects included/excluded
Amplitude deg/m
4.50E-02
4.00E-02
3.50E-02
3.00E-02
2.50E-02
2.00E-02
1.50E-02
1.00E-02
5.00E-03
0.00E+00
0
0.2
0.4
0.6
0.8
1
1.2
1.4
1.6
1.8
Angular frequency rad/s
Viscous effects included
No viscous effects

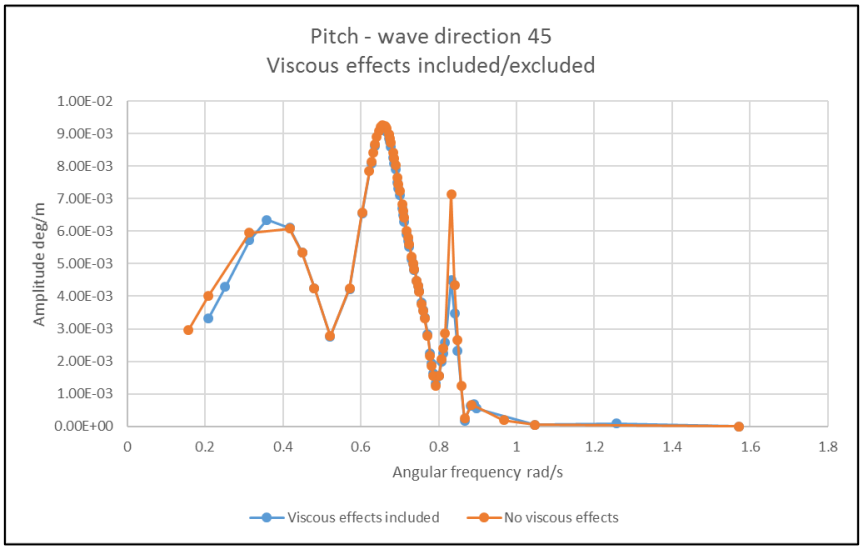
Pitch - wave direction 45
Viscous effects included/excluded
Amplitude deg/m
1.00E-02
9.00E-03
8.00E-03
7.00E-03
6.00E-03
5.00E-03
4.00E-03
3.00E-03
2.00E-03
1.00E-03
0.00E+00
0
0.2
0.4
0.6
0.8
1
1.2
1.4
1.6
1.8
Angular frequency rad/s
Viscous effects included
No viscous effects

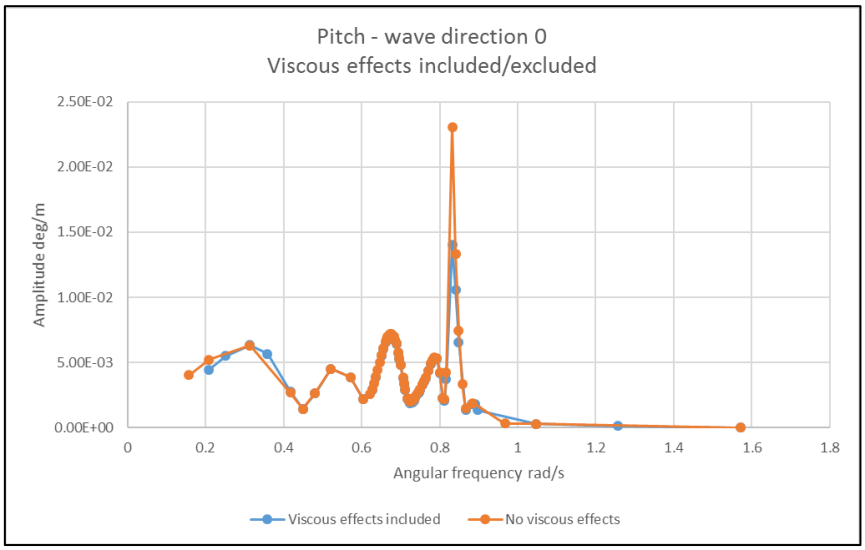
Pitch - wave direction 0
Viscous effects included/excluded
Amplitude deg/m
2.50E-02
2.00E-02
1.50E-02
1.00E-02
5.00E-03
0.00E+00
0
0.2
0.4
0.6
0.8
1
1.2
1.4
1.6
1.8
Angular frequency rad/s
Viscous effects included
No viscous effects

Appendix B - MATLAB Code for Mooring Line

```
% Water depth, 120 meters
h = 0:1:120;

% Horizontal load [N] - equal to drag load
% With Preangle of 25.9 degrees and Pretension of 480 kN
phi = 25.9;
T_pre = 480000;
H = T_pre*(cosd(phi))

% Submerged weight per meter [N/m]
W = 282.5*10

% Distance to touchdown point [m]
L = (H/W)*acosh(((W*h)/H)+1);

indexmax = find(max(L) == L);
Lmax = L(indexmax)

% x is used as lenght for further calculations
x = L;

% Geometric profile of catenary
y = (H/W)*(cosh((W/H)*x)-1);

y_max = (H/W)*(cosh((W/H)*Lmax)-1);

% Distance from touchdown point to anchor
x2 = -100:1:0;
indexmax2 = find(max(x2) == x2);
y2 = zeros(1,indexmax2);

% Coordinates of touchdown point
x_td = 0;
y_td = 0;

% Plot of mooring line geometry
figure(1)
plot(L,y,'b')
grid on;
hold on
plot(x2,y2,'b')
hold on
plot(x_td,y_td,'ro','MarkerSize',13)
axis tight
xlabel('Distance from touchdown point [m]')
ylabel('Distance to seabed [m]')
title('Catenary geometry')
```

```
H = 4.3179e+05

W = 2.4564e+03

Lmax = 195.2089
```

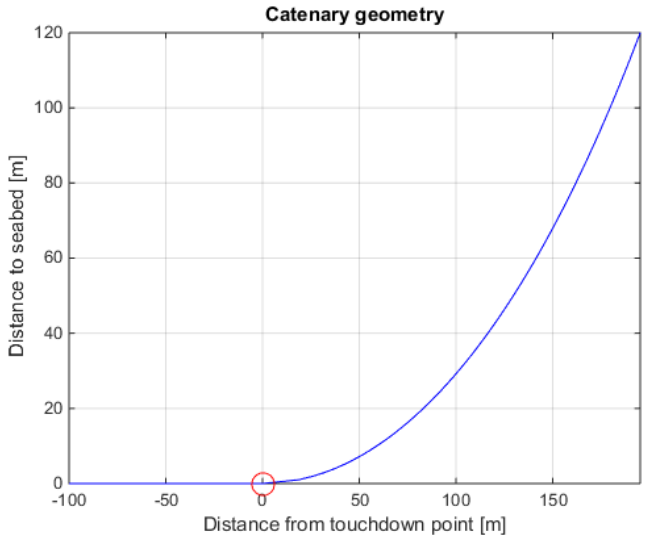

Catenary Length

```
s = (H/W)*(sinh((W*Lmax)/H))

%Tension
T = sqrt((H^2)+(W*s).^2)

% Vertical load [N]
V = W*s

%Max tension in kg
Tkg = T/10
```

```
s = 237.8810

T = 7.2656e+05

V = 5.8433e+05

Tkg = 7.2656e+04
```

Fish Cage Net

```
% Position of the fish net closest to the mooring line.
% % Given that the fish net is a square net and that the closest side is
% % located 80 m behind the turret. And that the net is 50 m deep.
D_tur = 80;
d_fish = 120-50;

L_fish = (H/W)*acosh(((W*d_fish)/H)+1);
i_fish = Lmax-D_tur;
i = ones(1,61)*i_fish;
j = 60:1:120;

% Distance between mooring line and bottom of fish cage. [m]
clearence = L_fish-i_fish

% Plot of mooring line geometry and simplified fish cage
figure(2)
plot(L,y,'b')
grid on;
hold on
plot(x2,y2,'b')
hold on
plot(x_td,y_td,'ro','MarkerSize',13)
hold on
plot(i,j,'m')

axis tight
xlabel('Distance from touchdown point [m]')
ylabel('Distance to seabed [m]')
title('Catenary geometry')
```

```
clearence = 36.8765
```

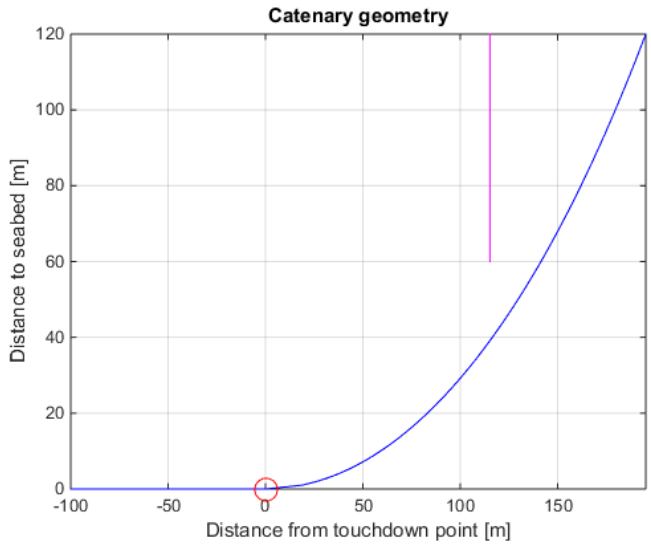

Appendix C – Translational Motions from SIMO

Translation in X-direction for Hs 2m, Tp 6s, Dir 180

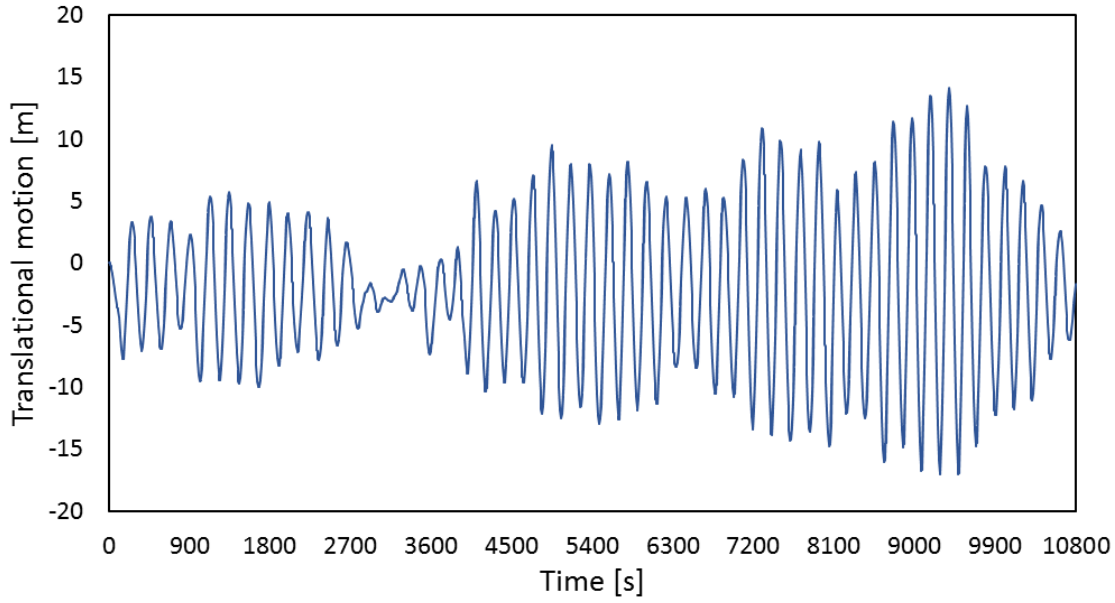

Translation in X-direction for Hs 2m, Tp 6s, Dir 150

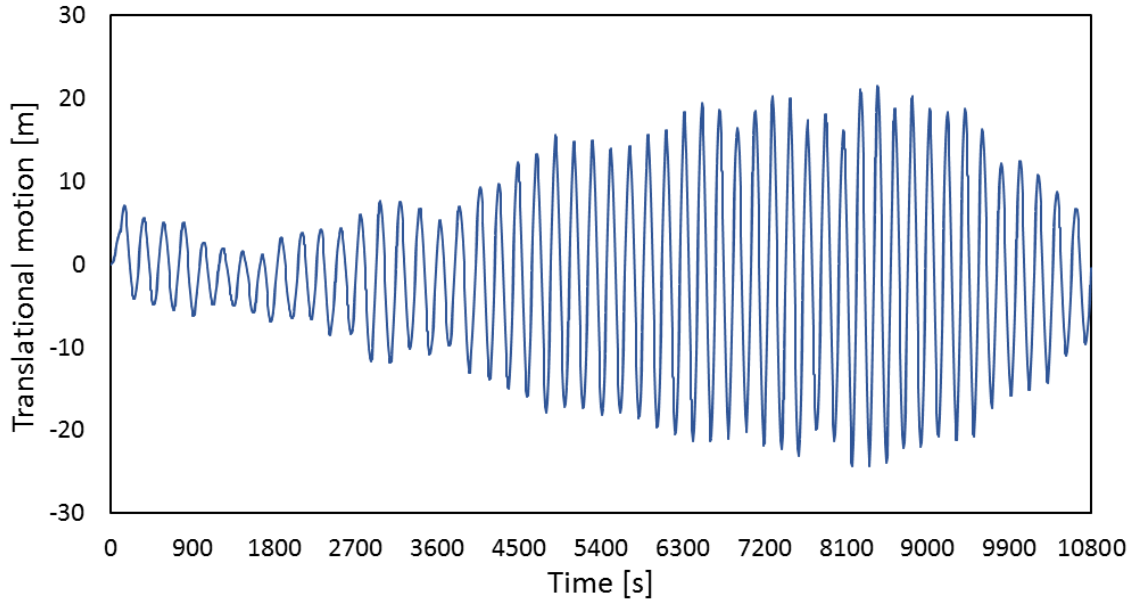

Translation in Y-direction for Hs 2m, Tp 6s, Dir 150

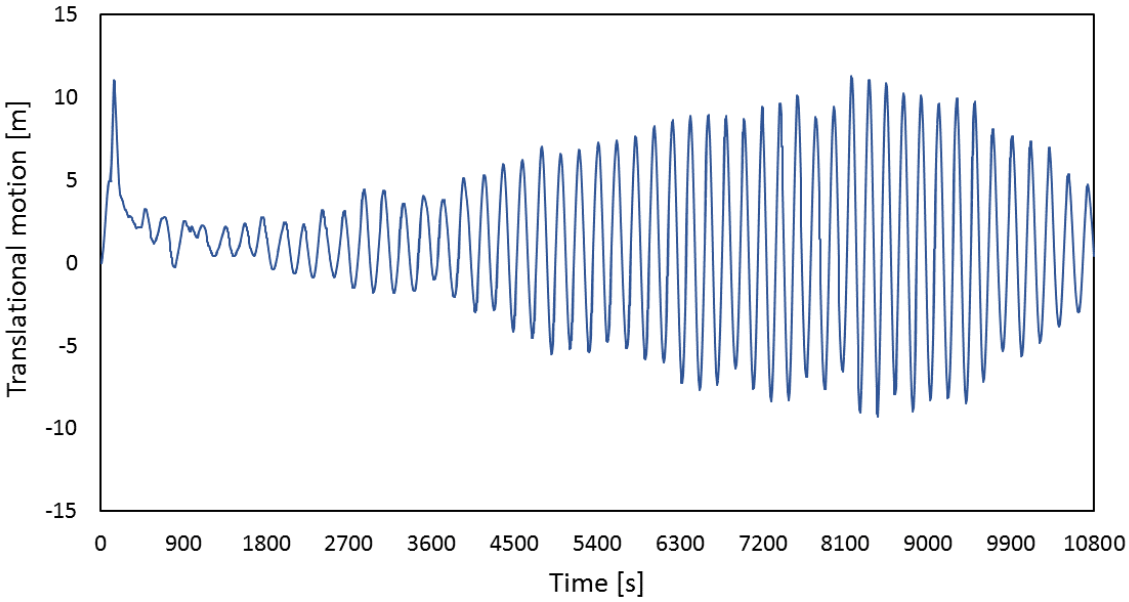

Translation in X-direction for Hs 3m, Tp 7s, Dir 180

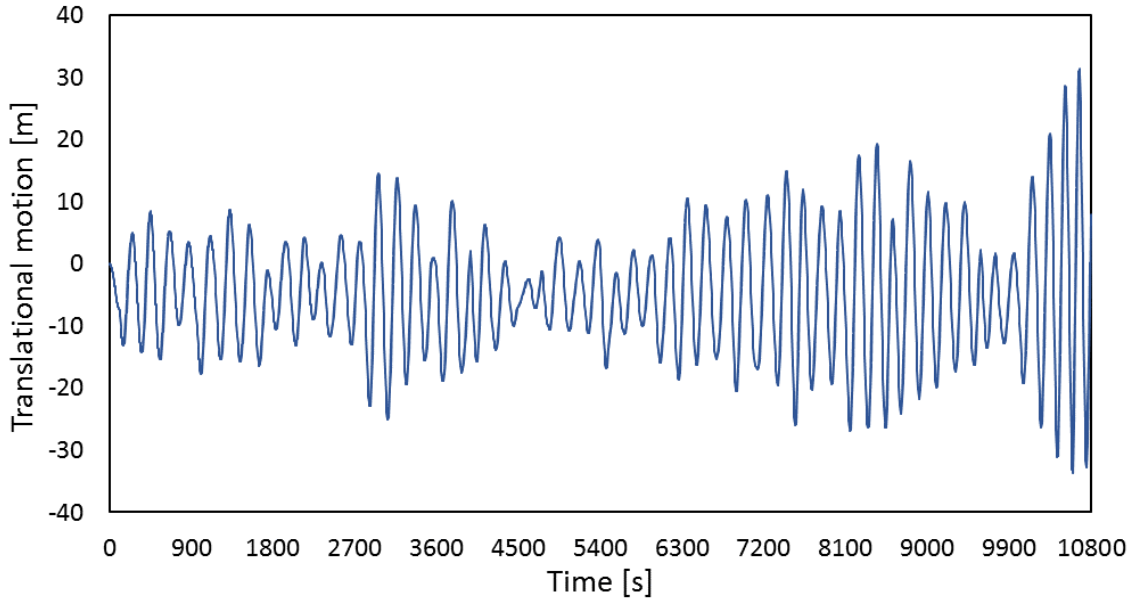

Translation in Y-direction for Hs 4m, Tp 9s, Dir 150

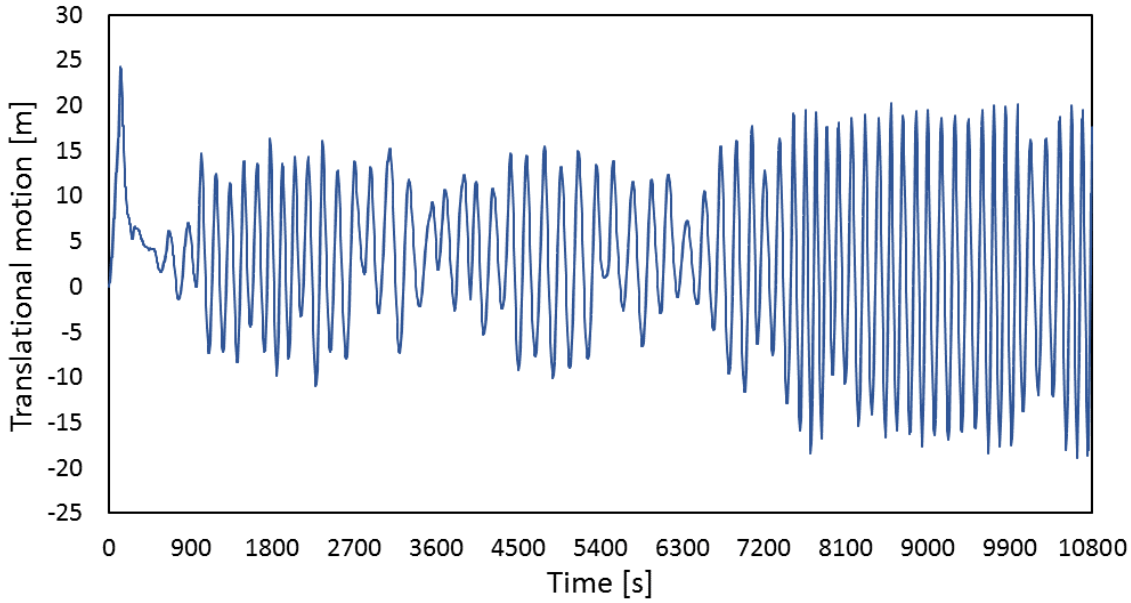

Appendix D – MATLAB code for fish nets

```
% Floater node 1 position, X1
X1 = 69.4;
% Floater node 1 position, Y1
Y1 = 5.52;
% Floater node 2 position, X2
X2 = 68.7;
% Floater node 2 position, Y2
Y2 = 0.0;

% Distance between floater nodes, L [m]
L = sqrt((X1-X2)^2 + (Y1-Y2)^2);
% Average distance, L_avg [m]
L_avg = L/2;


% Flexible Nets

% Constants
% Diameter of twine, d [m]
d = 0.003;
% Elastic module of twine, E [Pa]
E = 350*10^6;
% Density of twine [kg/m^3]
p = 1710;
% Solidity, Formula: Sn = ((2d)/Lambda)-(d/Lambda)^2
Sn = 0.15;

% Lambda [m], From formula for Sn
lambda = (2*d + sqrt((2*d)^2 - 4*Sn*(d^2)))/(2*Sn);

% Twine cross sectional area, A_twine [m^2]
A_twine = (pi/4)*(d)^2;

% Average number of vertical twines per meter, n_vert
n_vert = L_avg/lambda;

% Average number of twines per meter, n
n = (L_avg/d)*Sn;

% Axial Stiffnes, EA (from vertical twines) [N]
k = E*A_twine*n_vert;

% Net average external area, A_net [m^2]
A_net = A_twine * n;
% Unit mass, M (average number of twines) [kg/m]
M = A_net * p;


% Rigid Nets
% Calculation of drag coefficient
```

```
% Floater node 1 position, X1 = 69.411 (from above)
% Floater node 13 position, X13
X13 = 111.3;
% Diameter of net at floater, Dfloat [m]
D_float = X13 - X1;
% Depth of fish cage, h [m]
h = 44.0;

% Diameter of rigid element, Drigid [m]
D_rigid = 0.1;
% Angle of net, phi [rad]
theta = 90 - atand((D_float/2)/h);
% Twine drag coefficient from Solidity, Cd_twine [-]
Cd_twine = 0.04+(-0.04 + 0.33*Sn + 6.54*Sn^2 - 4.88*Sn^3)*cosd(theta);
% Twine lift coefficient from Solidity, Cl_twine [-]
Cl_twine = (-0.05*Sn + 2.3*Sn^2 - 1.76*Sn^3)*sind(2*theta);

% Quadratic drag coefficient per unit lenght in normal direction, Cd [-]
Cd_rigid = (Cd_twine*L_avg*cosd(theta)+Cl_twine*L_avg*sind(theta))/D_rigid

% Added mass, Ma [kg/m]
Ma = 1025*A_net


% Current Velocity Reduction factor

% reduction factor, r [-]
r1 = 1 - 0.46 * Cd_twine
r2 = r1 - 0.46 * Cd_twine;
r3 = r2 - 0.46 * Cd_twine
r4 = r3 - 0.46 * Cd_twine;
r5 = r4 - 0.46 * Cd_twine
r6 = r5 - 0.46 * Cd_twine;
r7 = r6 - 0.46 * Cd_twine
r8 = r7 - 0.46 * Cd_twine;
r9 = r8 - 0.46 * Cd_twine
```

```
Cd_rigid =    1.9462

Ma =    1.0079

r1 =    0.9539

r3 =    0.8616

r5 =    0.7694

r7 =    0.6772

r9 =    0.5849
```